Surface phonon polaritons in silicon carbide nanostructures revealed by near-field imaging and spectroscopy

Andrea Mancini

München 2023

Surface phonon polaritons in silicon carbide nanostructures revealed by near-field imaging and spectroscopy

Andrea Mancini

Dissertation
an der Faculty of Physics
der Ludwig–Maximilians–Universität
München

vorgelegt von
Andrea Mancini

München, den 9/1/2023

Contents

List of Figures

Zusammenfassung

Die Beugungsgrenze stellt eine untere Grenze für die Mindestgröße dar, auf die das Licht im freien Raum fokussiert werden kann. Um die Intensität der Licht-Materie-Wechselwirkung zu erhöhen, werden traditionell metallische Antennen eingesetzt, die sich durch eine signifikante Verstärkung und Beschränkung des Oberflächenfeldes auszeichnen. Diese Effekte sind eine Folge des Vorhandenseins freier Elektronen, die sich gegen das äußere elektromagnetische Antriebsfeld bewegen. Die höchste Feldeinschränkung für Edelmetallantennen wird im sichtbaren Bereich durch die Anregung von gemischten Photonen-Elektronen-Zuständen, den so genannten Oberflächenplasmonen-Polaritonen, erreicht. Die Leistung bei optischen Frequenzen wird jedoch durch hohe Verluste aufgrund des Eindringens des elektromagnetischen Feldes in das Material und der Verlustleistung durch Elektron-Elektronen-Streuung begrenzt.

Der Einschluss von Feldern im Subwellenlängenbereich kann auch in Materialien mit starken polaren Bindungen realisiert werden. In diesem Fall sind es nicht die freien Elektronen, die sich gegen das treibende Feld bewegen, sondern die Gitterschwingungen, die Phononen. Analog zu den Oberflächenplasmonen-Polaritonen gibt es in diesen Materialien auch Oberflächenphononen-Polaritonen. Diese Anregungen treten in einem engen Frequenzbereich auf, der zwischen einem transversalen und einem longitudinalen optischen Phonon liegt. Der Zerfallsmechanismus von Phonon-Polaritonen hängt mit der Phonon-Phonon-Streuung zusammen, die im Vergleich zur Elektron-Elektron-Streuung ein viel langsamerer Prozess ist, was die Lebensdauer dieser Zustände erhöht.

In dieser Arbeit untersuchen wir die lokalisierten und sich ausbreitenden Modi von Oberflächenphonon-Polaritonen in verschiedenen Siliziumcarbid-Nanostrukturen. Siliziumcarbid wurde als Material ausgewählt, da es geringe Verluste und einen breiten Frequenzbereich aufweist, in dem Oberflächenphonon-Polaritonen angeregt werden können. Besonderes Augenmerk wird auf die Untersuchung des Nahfeldverhaltens dieser verschiedenen Systeme gelegt, die mittels optischer Nahfeldmikroskopie mit Streuung untersucht wird. Im ersten Kapitel geben wir einen Überblick über die Gemeinsamkeiten und Unterschiede zwischen Oberflächenplasmonen und Oberflächenphononenpolaritonen. Anschließend werden einige theoretische Methoden beschrieben, die im weiteren Verlauf der Arbeit für die numerische Lösung der Maxwell-Gleichungen bei zwei- und dreidimensionalen Problemen verwendet werden. Im dritten Kapitel werden einschlägige experimentelle Methoden vorgestellt, wobei ein besonderes Augenmerk auf die Nahfeldmikroskopie und ihre allgemeinen Prinzipien gelegt wird.

In Kapitel 4 berichten wir über die Nahfeldmessungen an einer Siliziumkarbid-Metasurface. Wir zeigen auf, wie die Anwesenheit der AFM-Spitze, die für die Nahfeldmessungen verwendet wird, die Reaktion des Systems stört. In Kapitel 5 beschreiben wir hoch eingeschlossene Oberflächenphonon-Polaritonen, die in schwebenden Siliziumkarbid-Dünnschichten angeregt werden können. Die Dispersion dieser Oberflächenmoden wird durch Nahfeldspektroskopie ermittelt. Im letzten Kapitel zeigen wir, wie die in Kapitel 5 beschriebenen hoch eingeschlossenen Polaritonen zur Erzeugung von Phonon-Polariton-Wirbeln verwendet werden können, die durch Nahfeldspektroskopie sichtbar gemacht werden.

Summary

The diffraction limit poses a lower bound to the minimum size to which light can be squeezed by free-space focusing. To increase the intensity of light-matter interactions, metallic antennas featuring high surface field enhancement and confinement have been traditionally employed. These effects are a consequence of the presence of free-electrons that move against the external electromagnetic driving field. The highest field confinement for noble metal antennas is achieved in the visible thanks to the excitation of mixed photon-electron states named surface plasmon polaritons. However, performances at optical frequencies are limited by high losses due to penetration of the electromagnetic field inside the material and dissipation through electron-electron scattering.

Subwavelength field confinement can also be realized in materials with strong polar bonds. In this case, it is not the free-electrons moving against the driving field, but the lattice vibrations, or phonons. Analogous to surface plasmon polaritons, surface phonon polaritons exist in these materials. These excitations exist in a narrow frequency range bounded between a transverse and a longitudinal optical phonon. The decay mechanism of phonon polaritons is associated with phonon-phonon scattering which is a much slower process compared to electron-electron scattering, enhancing the lifetime of these states.

This work is focused on exploring surface phonon polariton modes in different silicon carbide nanostructures. Silicon carbide is the material of choice as it features low losses and a wide frequency region where surface phonon polaritons can be excited. Particular attention is given to the investigation of the near-field response of these different systems, which is probed through scattering-scanning near field optical microscopy. In the first chapter an overview of the similarities and differences between surface plasmon polaritons and surface phonon polaritons is given. In chapter 2, several theoretical methods used in the rest of the work for the numerical solution of Maxwell's equations in two and three-dimensional problems are presented. Relevant experimental methods are introduced in chapter 3, with an in-depth description of near-field microscopy and its general principles.

Chapter 4 reports on the near-field measurements of a silicon carbide metasurface. The perturbation introduced by the AFM tip used for the near-field measurements on the response of the system is analyzed. Chapter 5 describes highly confined surface phonon polaritons that can be excited in suspended silicon carbide thin-films. The dispersion of these surface modes is retrieved through near-field spectroscopy. The final chapter shows how the highly confined polaritons described in chapter 5 can be used to generate phonon-polariton vortex which are revealed though near-field imaging.

Chapter 1

Introduction

1.1 Confining light below the diffraction limit

Optical imaging and spectroscopy have been fundamental tools for the scientific progress in many research fields, including solid state physics, astronomy, chemistry and biology. Since the discovery of the wave nature of electromagnetic (em) radiation, physicists realized that diffraction posed a lower limit to the resolution of optical systems. In 1873 Ernst Abbe formulated the concept of *diffraction limit*, stating that the minimum distance d between two objects so that they can be resolved in a microscope depends on the wavelength of the employed em radiation [1]:

$$d = \frac{\lambda}{2n\sin\theta} \tag{1.1}$$

where λ/n is the wavelength of light in a material with refractive index n and θ the half-angle of the focusing cone. Due to diffraction, the image of a single point dipole source appears as an interference pattern referred to as *point spread function*, which depends on the numerical aperture (NA $= n\sin\theta$) of the focusing objective [1]. The point spread function for two different NA at $\lambda = 500\,\text{nm}$ and $n = 1$ is shown in Figure 1.1 a) (for details see Appendix A). Diffraction through the finite-sized circular aperture of a telescope analogously puts a lower limit to the angular resolution for astronomical observations. The wavelength of visible light is between $400\,\text{nm}$ and $700\,\text{nm}$, meaning that with a conventional microscope it is possible to resolve many biological entities, like cells and bacteria, whose size is on the order of microns. However, the resolution is not enough for smaller objects like viruses, proteins or single molecules. With the rise of nanotechnology, not only many natural phenomena are too small to be investigated with standard optical microscopes, but also artificial structures now require different imaging techniques. One straightforward way to increase the resolution is to reduce the employed wavelength as suggested by eq. 1.1. This recipe can be applied not only to em radiation, but also to massive particles thanks to the particle-wave duality of quantum mechanics. Following this principle, electron microscopes are routinely employed to achieve a resolution on the order of nanometers [2]. Since the De-Broglie wavelength is inversely proportional to the mass of the particle, even

higher resolutions can be achieved by using massive ions [3,4]. However, all these solutions pose a much greater technological challenge compared to conventional optical microscopes and often work only under specific conditions (i.e. vacuum, conductive materials, etc...). Moreover, one is often constrained to use light at specific wavelengths to probe particular excited states of a specimen. For example, vibrational modes of molecules and phonons in solids lye in the infrared (IR) range, while electronic transitions are typically found at visible and UV frequencies [5,6]. Therefore, overcoming the diffraction limit has been a central topic in optics, and fundamental steps in this direction have been made both through *far-field* [7] and *near-field* [8,9] techniques.
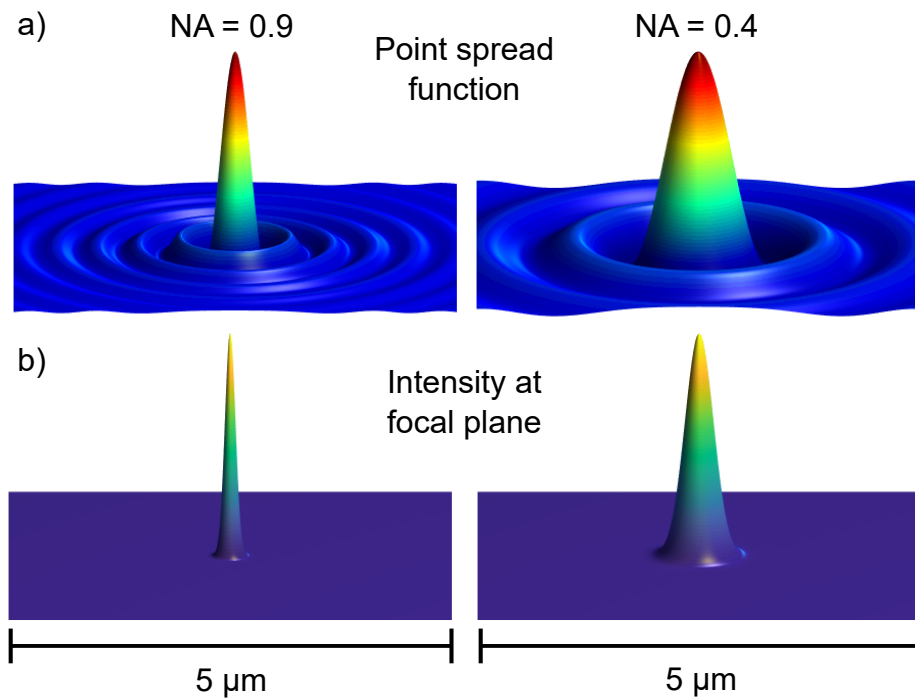
Figure 1.1: Calculated point spread function a) and field intensity at the focal plane b) for two different NAs at a wavelength of $\lambda = 500\,\text{nm}$. Details of the equations used for the plots can be found in Appendix A.

On top of limiting the spatial resolution achievable by microscopes and telescopes, diffraction also poses a lower limit on the volume in which light can be confined. When focusing light through an objective, the focal spot size is on the order of $(\lambda/n)^3$ [1]. In Figure 1.1 b) the field intensity $I = |E|^2$ (in the paraxial approximation [1], for details see Appendix A) in the focal plane is shown for two different objective NAs. The inability to shrink light below a certain size is detrimental, for example, for reducing the size of on-chip photonic integrated circuits [10,11] and to achieve strong light-matter interactions [12]. Another case of technological relevance is in mid-IR sensing, where the vibrational fingerprint allows the discrimination between different molecular species [13]. However, due to the dimensional mismatch between molecules and mid-IR wavelengths ($2.5\,\text{µm}$ to $10\,\text{µm}$), their

absorption cross-section is extremely small [12]. As a consequence, only relatively large amount of molecules can be probed by techniques relying on far-field focusing. The same argument applies to Raman spectroscopy, which is also a chemically selective technique associated with extremely small scattering cross sections [14]. Shrinking light to subwavelength volumes allows increased sensitivity of IR and Raman spectroscopies, which are both active research areas in the field of *nanophotonics*.

1.2 Optical response of metals and polar dielectrics

Since the advent of modern nanofabrication techniques, it has been clear that subwavelength em confinement could be achieved by borrowing the radiofrequency (RF) antenna concept and scale it down to the nanoscale. As RF antennas are made of metals, the natural choice in the development of optical nanoantennas has been to use the same class of materials, leading the development of the field of *Plasmonics* [15]. The term comes from the collective excitation of mixed light-electron surface states named *Surface Plasmon Polaritons* (SPPs). Since the early 2000s a large amount of effort has been dedicated to the development of different types of plasmonic antennas. However, the material choice has been quite limited, as the need for low optical losses and chemical stability restricted most research to the use of gold. Even neglecting its scarcity and high price which hamper possible large-scale commercial applications, the community realized that even in gold the fundamental material losses are too high for a number of applications initially envisioned [16, 17, 18, 19]. The need to find alternative viable materials has led to the investigation of graphene [20], doped semiconductors [21] and non-noble metal [19] as alternative plasmonic platforms. The em response of metals (and more generally of any plasmonic material) is characterized by the presence of electrons in the conduction band that can freely move and polarize in the opposite direction of the incoming field, resulting in a very low penetration of em radiation inside the material. This behavior manifests itself as a negative real part of the dielectric function $\mathrm{Re}(\varepsilon) < 0$, suggesting that alternative materials characterized by $\mathrm{Re}(\varepsilon) < 0$ can also be used for the fabrication of em antennas. This is the case for polar dielectrics (or ionic crystals), which feature a $\mathrm{Re}(\varepsilon) < 0$ region related to the strong absorption of an IR active transverse optical phonon [22]. We will review in more details is section 1.3 and 1.4 the reason why $\mathrm{Re}(\varepsilon) < 0$ is the key ingredient to obtain subwavelength em confinement.

In ionic crystals, the coulomb force between the oppositely charged ions holds the lattice together. Examples of polar dielectrics are silicon carbide (SiC), gallium phosphide (GaP) and indium arsenide (InAs). Contrary to metals, in polar dielectrics the microscopic charges polarizing against the incoming field are the polar bonds in the material. Here light strongly couples to lattice vibrations, resulting in the existence of collective excitations named *Surface Phonon Polaritons* (SPhPs), which share many features with SPPs. To understand the properties of SPhPs ans SPPs, in the following we briefly describe the optical response of metals and polar dielectrics.

The em response of a material is determined by the dielectric function, relating the field in the material $\mathbf{D}(\mathbf{r}, t)$ to the external one $\mathbf{E}(\mathbf{r}, t)$. In Fourier space [23]:
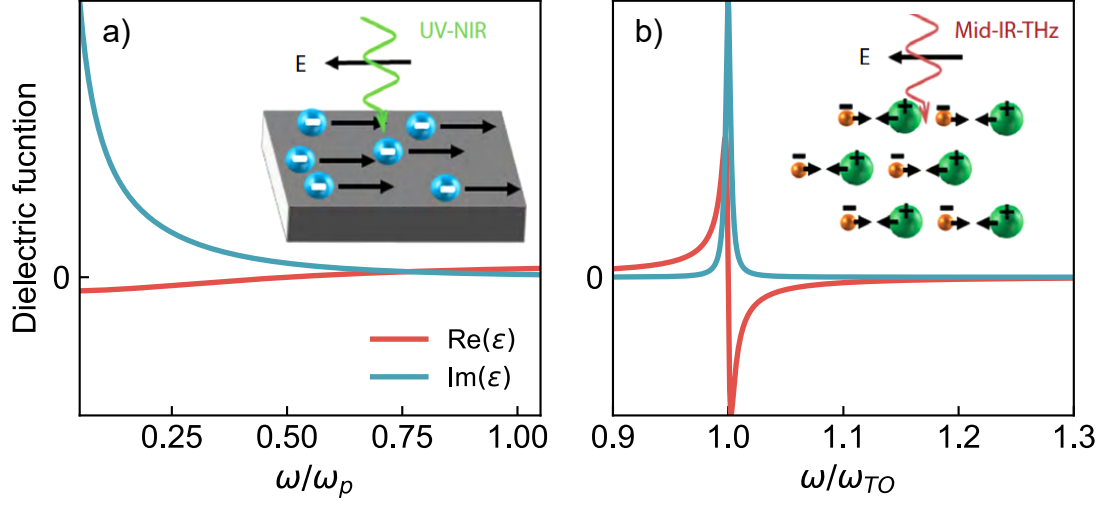
Figure 1.2: Dielectric function from the Drude model eq. 1.3 a) describing the em response of free-electrons ($\gamma = \omega_p/2$, $\varepsilon_\infty = \omega_p/5$) and b) from the Lorentz model eq. 1.5 describing the em response in the presence of a transverse optical phonon ($\omega_{LO} = 3\omega_{TO}/2$, $\gamma = \omega_{TO}/200$, $\varepsilon_\infty = \omega_{TO}/500$).

$$D_i(\mathbf{q}, \omega) = \varepsilon_{i,j} E_j(\mathbf{q}, \omega) \tag{1.2}$$

If the material is isotropic, the dielectric function is a scalar quantity, and if nonlocal effects are neglected only a function of frequency $\varepsilon(\omega)$. The em behaviour of an electron plasma can be described through the Drude model [6], while resonant processes, such as the excitation of electronic or vibrational states, are described with the Lorentz model. The dielectric functions associated with the Drude and Lorentz models are shown in 1.1 a) and b), respectively. The response of metals often deviates from a pure Drude response due to the presence of interband transitions at energies below the plasma frequency ω_p. The Drude model dielectric function is described by the following equation:

$$\varepsilon(\omega) = \varepsilon_\infty - \frac{\omega_p^2}{\omega^2 - i\gamma\omega} \tag{1.3}$$

where γ is the inverse of the mean time between electron collisions and determines losses in the material, while ε_∞ offsets the baseline level of ε to take into account for interband transitions at higher frequencies $\omega > \omega_p$. The plasma frequency depends on the electron density n and effective mass m^* as:

$$\omega_p = \sqrt{\frac{ne^2}{\varepsilon_0 m^*}} \tag{1.4}$$

where e is the electron charge and ε_0 the vacuum permittivity. The effective mass of an electron depends on the conduction band curvature of the material [6]. The plasma frequency represents the frequency below which electrons can follow the external driving field, while above it electrons "lag" behind the driving field. At $\omega > \omega_p$ the material does not behave anymore as a metal, optically speaking. On the other side for $\omega \to 0$, metals behave like perfect conductors, for which $\mathrm{Re}(\varepsilon(\omega))$ is formally infinitely negative. The electron density n in eq.1.4 is the main factor determining the plasma frequency of a material. Consequently, metals usually have ω_p in the visible or UV range ($n \sim 10^{22} - 10^{23}\,\mathrm{cm}^{-3}$), while doped semiconductors in the far to near infrared region depending on the doping level ($n \sim 10^{23} - 10^{29}\,\mathrm{cm}^{-3}$). An interesting case is the one of graphene, where the electron density can be tuned upon application of an external voltage bias [24].

The response of polar dielectrics close to an optical phonon can be described by a Lorentz-type function, which in this case takes the following form:

$$\varepsilon(\omega) = \varepsilon_\infty \left(1 + \frac{\omega_{LO}^2 - \omega_{TO}^2}{\omega_{TO}^2 - \omega^2 - i\gamma\omega} \right) \tag{1.5}$$

where ε_∞ and γ have the same meaning as in the Drude model, while ω_{TO} and ω_{LO} are the frequencies of a transverse (TO) and longitudinal (LO) optical phonons. The region with $\mathrm{Re}(\varepsilon) < 0$ is called the Reststrahlen (RS) band, which is bounded below by a TO phonon and above by a LO phonon. As the optical response of polar dielectrics depends on their phonon structure, we summarize here some features of lattice vibrations in crystals.

In any three dimensional crystal with p atoms in the primitive cell there are $3p$ phonon modes, out of which three are acoustic and $3(p-1)$ are optical. The acoustic phonon dispersion $\omega(k)$ is characterized by a linear dispersion close to the $k = 0$ point. As the photon momentum is small compared to the lattice momentum (approximately 4 orders of magnitude smaller considering a mid-IR wavelength of $10\,\mu\mathrm{m}$ and a lattice spacing of $10\,\mathrm{\AA}$), photo-excitation of a phonon can only happen at the $k = 0$ point, and hence acoustic phonons cannot directly interact with light. Conversely, optical phonons have non zero energy even at the $k = 0$ point. For each phononic branch, there is one longitudinal and two transverse modes, however many of these are often degenerate due to symmetries in the crystal structure. As light is a transverse wave, only TO phonons can directly absorb photons, which is why $\mathrm{Im}(\varepsilon)$ in Figure 1.2 b) is large close to the TO phonon but not to the LO phonon. However, not all TO phonons directly interact with light, as a change in dipole moment is needed for absorption of em waves. Therefore, TO phonons in non-polar lattices do not absorb IR light, as a displacement of the ions does not produce any change in the dipole moment. Neglecting losses, a general relation can be established between the frequency of LO and TO phonons at $k = 0$, the so called Lyddane-Sachs-Teller relationship [27]:

$$\frac{\omega_{LO}^2}{\omega_{TO}^2} = \frac{\varepsilon(\omega = 0)}{\varepsilon_\infty} \tag{1.6}$$

As a consequence, non-polar dielectric have degenerate LO and TO phonons, as the absence of IR absorption results in $\varepsilon(\omega = 0) = \varepsilon_\infty$, where ε_∞ is considered as the value
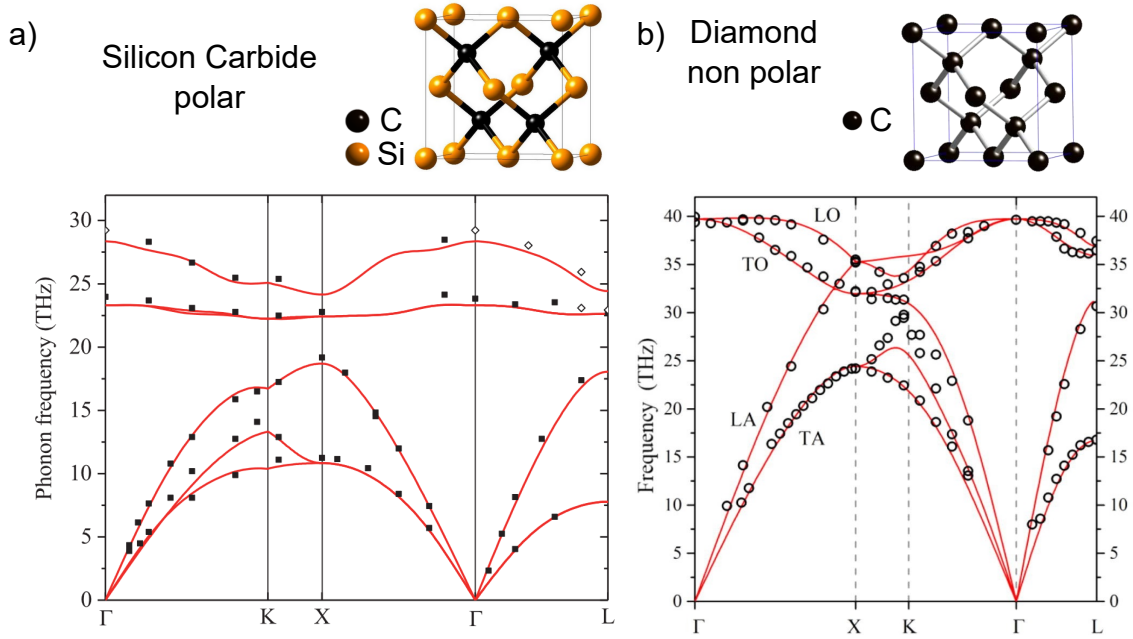
Figure 1.3: Unit cell and phonon band structure for SiC a) and diamond b). Red lines are calculated phonon dispersion while markers are experimental data. Adapted from [25] and [26].

of the dielectric function at high frequencies, but below the onset of interband transitions. An example of phonon band structures for a ionic crystal (silicon carbide, 3C polytype) and a non-polar dielectric (diamond), are shown in Figure 1.3 [25, 26]. As shown in the inset, both crystal structures are of the zincblende type, which is a face-centered-cubic lattice with two atoms in the basis. Consequently, we expect 3 acoustic phonon modes and 3 optical modes, 2 of which are TO and one LO. As predicted by the Lyddane-Sachs-Teller relationship, SiC features a splitting on the LO and TO energies at the Γ point, while the phonon branches in diamond are degenerate, as shown in Figure 1.3. Due to the high symmetry of the cubic lattice, the two TO phonon bands in SiC are degenerate along all the k-space directions.

In polar dielectrics featuring a RS band, the presence of a TO phonon does not result in an absorption peak in the IR spectrum. Since in the RS band $\mathrm{Re}(\varepsilon) < 0$, we expect a metallic-like behaviour, resulting in a high reflectivity region. This can be seen in Figure 1.4 for the case of SiC, which features a RS band in the $10\,\mu\mathrm{m}$ to $12.5\,\mu\mathrm{m}$ range. At the same time, both TO and LO phonons can be detected in Raman experiments, where only a change in polarizability is needed. In Figure 1.4 the Raman spectra of SiC is reported, showing two distinct peaks corresponding to the TO and LO phonons delimiting the RS band.

In this work we investigate the em response of different nanostructures supporting SPhPs in the mid-infrared. We choose silicon carbide (SiC) as the material platform
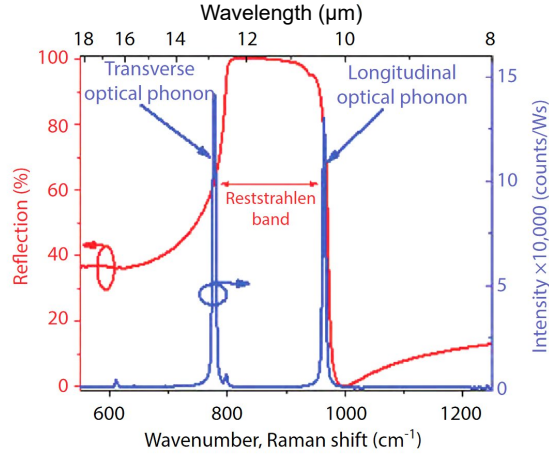
Figure 1.4: IR and Raman spectra of bulk SiC. Adapted from [22].

as it is one of the most common polar dielectrics with a wide RS band and low losses, and is already an established material in the field of power electronics [28] and quantum optics [29]. Particular attention is given to the study of *near-field* effects of SPhPs, which we investigate through the employment of scattering scanning optical microscopy (sSNOM).

1.3 Subwavelength field confinement: surface waves

In the previous section we discussed the optical response of metals and polar dielectrics, which are both characterized by having frequency regions where $\mathrm{Re}(\varepsilon) < 0$. Here we discuss how $\mathrm{Re}(\varepsilon) < 0$ is a necessary condition to achieve subdiffractional field confinement when exciting surface waves at the boundary of two semi-infinite slabs. We start by considering the fact that the diffraction limit can be understood as a manifestation of Heisenberg uncertainty principle [30]:

$$\Delta x \Delta p_x \geq \frac{\hbar}{2} \tag{1.7}$$

The momentum of a photon is $\Delta p_x = \Delta k_x \hbar / 2\pi$. We consider here for simplicity a 2-dimensional case where a beam propagating in vacuum in the y direction is focused in the x direction by an objective. The spread of momentum in the x direction is then related to the numerical aperture of the objective, since $k_x^{\min} = 0$ and $k_x^{\mathrm{MAX}} = k_0 \mathrm{NA}$. In the ideal case of an infinitely extended objective, $\mathrm{NA} = 1$. Then, $k_x^{\mathrm{MAX}} = k_0 = 2\pi/\lambda$. By substituting in eq. 1.7 we obtain:

$$\Delta x \geq \frac{\lambda}{2} \tag{1.8}$$

Which is the diffraction limit expressed in eq. 1.1. We see therefore that to overcome the diffraction limit we would need to have a larger spread in the photon momentum with
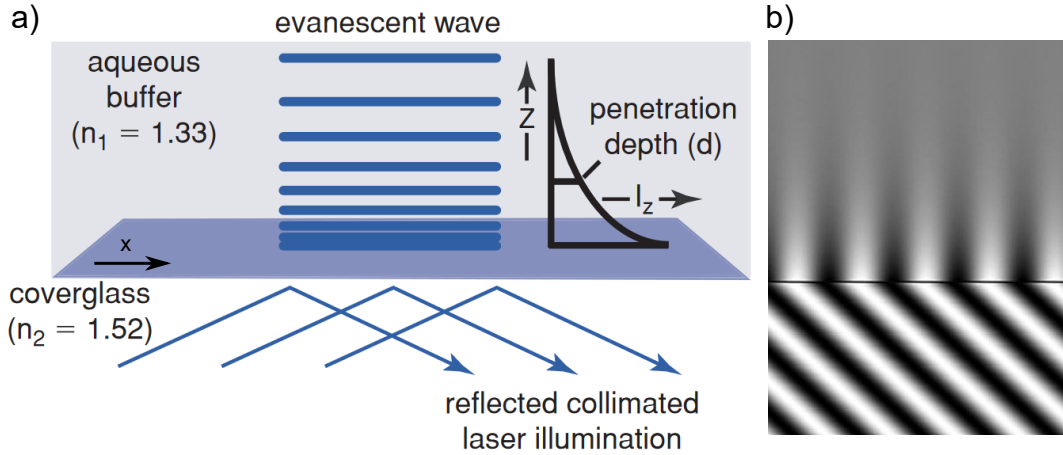
Figure 1.5: a) Sketch of the TIR phenomena associated with the creation of evanescent waves in the medium with lower refractive index. b) Electric field profile at the materials boundary at TIR condition, highlighting the same spatial variation on both sides of the interface. Adapted from [31].

$k_x^{MAX} > k_0$. However, $k_0^2 = k_x^2 + k_y^2$, and as long as k_x and k_x are real numbers, which is the case for free-space propagating light, the diffraction limit holds. Conversely, if k_y is imaginary, the spatial spread of the field in the x direction can be confined under the diffraction limit since $k_x > k_0$. An imaginary k-vector is associated with an exponentially damped field since $\mathbf{E} = \exp{(i\mathbf{k} \cdot \mathbf{r})}$. The existence of these so called *evanescent-waves* is connected in general to the presence of a material boundary. The region close to the surface where these exponentially decaying fields are present is called the *near-field*, as these fields components do not propagate and cannot be observed in the *far-field* far away from the interface.

We now consider the simplest case of material interface, where two semi-infinite slabs occupy the whole 2-dimensional space. The easiest way to produce an evanescent wave is to consider two dielectric medium exhibiting total internal reflection (TIR) when light comes from the medium with the higher refractive index $n_2 > n_1$ above the critical angle $\theta_c = \arcsin(n_1/n_2)$ as shown in Figure 1.5 a). For continuity reasons, the field in medium n_1 cannot be zero right after the interface, and as such one expects an evanescent wave to be present. For the same continuity argument, the field in medium 1 has the same spatial modulation of the one in medium 2, which is governed by the free-space wavelength and does not allow breaking of the diffraction limit in the x direction, as can be seen in Figure 1.5. At the same time, the evanescent field in the z direction is routinely used in TIR fluorescence microscopy, which allows reduction of background signal from fluorophores far away from the interface. However, no field enhancement is associated with the TIR phenomena, as the field intensity from the surface scales as $I(z) = I_0 \exp(-z/d)$ where d is a critical decay distance and I_0 is the intensity below the surface from the incoming free-space light in medium n_2 [31].

Evanescent waves at the material boundary shown if Figure 1.5 can also be achieved through the excitation of surface waves (SW). SW propagate along the interface and feature exponentially decaying fields in the perpendicular direction. The existence of surface states at the interface between two mediums can be derived analytically from Maxwell's equations applying continuity relations for the E and H field [15]. The SW condition is enforced by demanding the field components to be exponentially decaying in the direction z perpendicular to the material interface $E_{i,j}(z), H_{i,j}(z) \propto \exp(-k_i z)$, where the index j runs over the field components, and i over the two mediums 1 and 2. To have exponentially decaying fields the real part of the wavevectors has to be positive $\mathrm{Re}(k_i) > 0$. From this condition and the continuity of the fields one gets that no transverse electric (TE) SW can exist at the boundary. Only transverse magnetic (TM) SW can exist, given that the real part of the dielectric function of the two slabs have opposite signs [15]:

$$\frac{k_1}{k_2} = -\frac{\varepsilon_1}{\varepsilon_2} \tag{1.9}$$

Therefore, SW withing a single boundary can only occur between a dielectric with $\mathrm{Re}(\varepsilon) > 0$ and a material with $\mathrm{Re}(\varepsilon) < 0$. We consider from now the medium 1 to be the dielectric and medium 2 to be the one with $\mathrm{Re}(\varepsilon) < 0$. The two k-vectors in the z direction satisfy the following equations [15]:

$$k_i^2 = \beta^2 - k_0^2 \varepsilon_i \tag{1.10}$$

where β is the wavevector of the SW in the propagation direction and is given by

$$\beta = k_0 \sqrt{\frac{\varepsilon_1 \varepsilon_2}{\varepsilon_1 + \varepsilon_2}} \tag{1.11}$$

These relationship work for all materials with $\mathrm{Re}(\varepsilon) < 0$, regardless of their microscopic details. Indeed, SW described by eq. 1.10 can exist in metals for $\omega < \omega_p$, in which case they are named surface plasmon polaritons (SPP), and in polar dielectrics in the RS band, where they are named surface phonon polaritons (SPhP). In Figure 1.6 the dispersion for both SSP and SPhP calculated with the dielectric functions shown in Figure 1.2 are reported. For simplicity we excluded here the imaginary part of the dielectric function and we considered the dielectric slab to be vacuum. A sketch of the electric field at the material boundary is shown in the inset of Figure 1.6 a). The em field is exponentially decaying in the z direction in both materials, with a strong confinement in the "metallic" one, while propagating in the x direction at the material interface. The dispersion for SPP and SPhP is similar, a divergence of the wavevector is found at the condition $\mathrm{Re}(\varepsilon(\omega)) = -1$ (or in general at $\mathrm{Re}(\varepsilon(\omega)) = -\varepsilon_{env}$, where ε_{env} is the dielectric function of the dielectric slab). For $\mathrm{Re}(\varepsilon) \ll 0$ in both cases the dispersion approaches the light line $\omega = ck_0$, where the SW behaves similarly to a free-space photon with poor confinement in both the x and z directions. The main difference is that since the SW condition is valid only for frequencies where $\mathrm{Re}(\varepsilon) < 0$, there is no lower energy bound for the existence of SSP, while SPhPs only exist above the TO frequency. An important feature of both SPP and SPhP dispersion
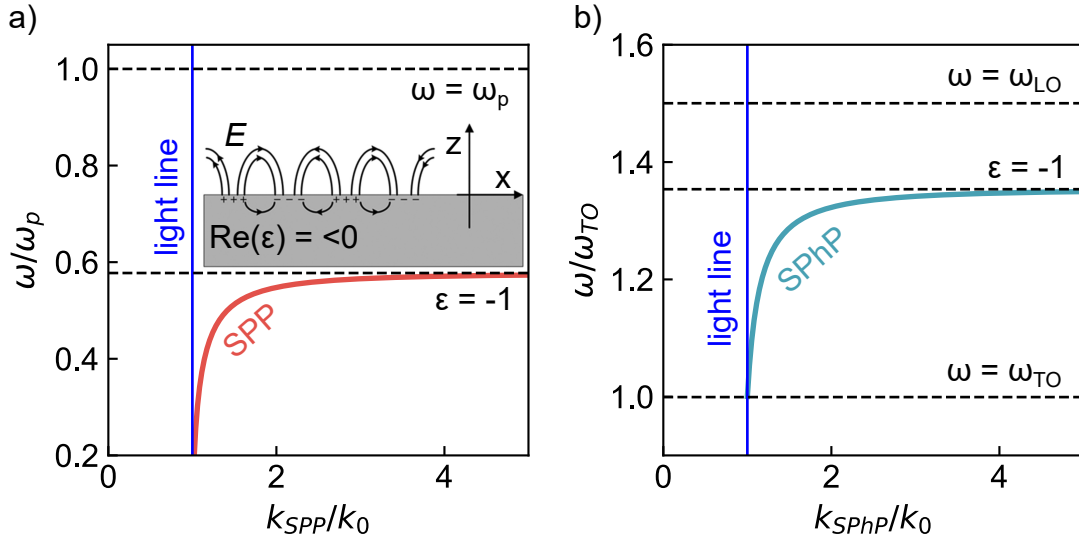
Figure 1.6: Dispersion for SPPs a) and SPhPs b) in vacuum. In the inset in a) a sketch of the field at the material boundary is shown. Adapted from [32].

curves is that they lie on the right of the light line. This means that conservation of energy and momentum cannot be fulfilled, and free-space photons cannot excite the SW. The additional momentum needed for excitation can be provided in a variety of ways, such as with gratings or by excitation with near-field sources [15].

The confinement of the SW can be evaluated in both the propagation and perpendicular directions by taking the inverse of the wavevector. In Figure 1.7 we plot the ratio between the SW wavelength and the free-space wavelength λ_0/λ_{SPhP} and the decay length of the field in the dielectric side $\delta = 2\pi/k_1$. At the same time, we plot the value of $\mathrm{Re}(\varepsilon)$. Subwavelength confinement is achieved in both cases for frequencies where the dielectric function is close to zero. A direct consequence of this is that for SPP and SPhPs the high confinement region is found in different wavelength ranges, being in the visible for SPPs in metals and in the mid to far infrared range for SPhPs. In this treatment we disregarded the imaginary part of the dielectric function. For real materials, the maximum in-plane k-vector is limited by the nonzero value of $\mathrm{Im}(\varepsilon)$ which consequently puts a lower limit on the achievable confinement. For non-negligible losses the k_{SW} dispersion shown in Figure 1.6 does not diverge at $\mathrm{Re}(\varepsilon) = -1$, but bends back towards the light line [15]. In general the k-vector is a complex quantity and a propagation length for the SW can be defined as $L = 1/2\mathrm{Im}(k_{SW})$. Higher confinement comes at the price of a lower propagation length due to higher field penetration in the material, associated with stronger losses.

From this discussion it is evident that from an electromagnetic point of view the behaviour of SPPs and SPhPs is very similar. However, as it will be described in following sections, there are fundamental quantitative and qualitative differences between these SW.

To reach the conclusion that a material with $\mathrm{Re}(\varepsilon) < 0$ is necessary to support SWs, we
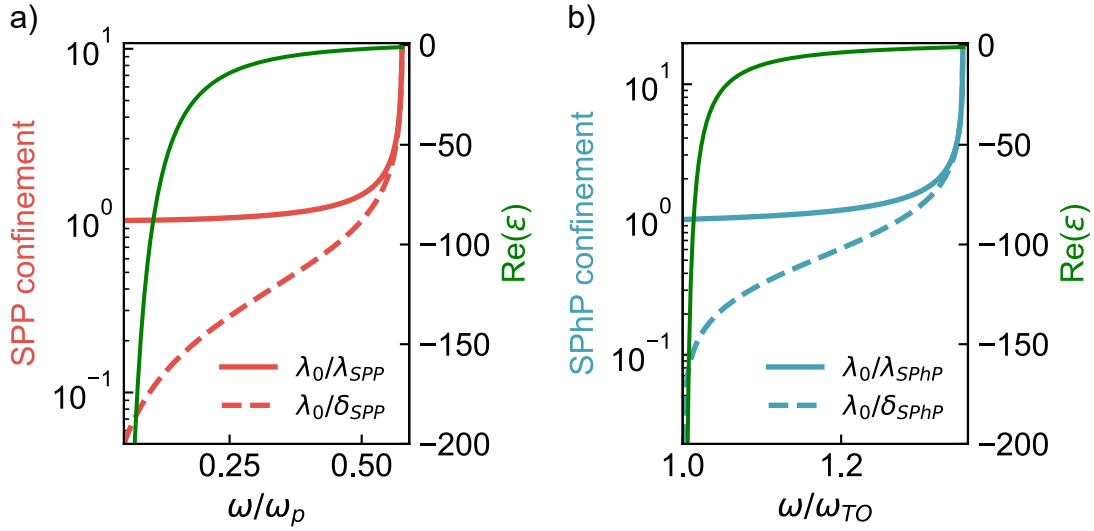
Figure 1.7: SW confinement for SPPs a) and SPhPs b) in both the direction of propagation λ_0/λ_{SW} and the direction perpendicular to the interface λ_0/δ_{SW}. Strong confinement is achieved where $\mathrm{Re}(\varepsilon)$ is close to zero.

considered in only the simple case of two-semi infinite slabs. It is worth mentioning that in more complex geometries SW can also be supported by purely dielectric architectures. This is for example the case for Bloch surface waves, where an heterostructure of alternating dielectric layers results in the existence of SW [33]. Even though SW can be excited in this configuration, the maximum wavevector of Bloch surface waves $\beta = 2\pi n_{SW}/\lambda_0$ is limited by the highest refractive index of the dielectric stack $1 < n_{SW} < n_{MAX}$ [33].

1.4 Subwavelength field confinement: resonators

In the previous section we highlighted how the presence of a $\mathrm{Re}(\varepsilon) < 0$ material is necessary to sustain SW at the boundary between two semi-infinite slabs, allowing for subdiffractional field confinement. The importance of negative permittivity can be also understood for resonators, independently of the detailed geometry of the system, from an energy conservation point of view [34]. We consider an optical cavity with a length that is a multiple of the wavelength, where standing waves can be formed. Both the electric field $\mathbf{E}$ and magnetic field $\mathbf{H}$ then have a spatial dependence in the confinement direction z of the form $\sin(2\pi z/\lambda)$. The system is sketched in Figure 1.8 a, b). The total em energy is periodically exchanged between the electric field energy $u_E \sim \varepsilon|\mathbf{E}|^2/2$ and the magnetic field energy $u_H \sim |\mathbf{H}|^2\mu/2$, where μ is the magnetic permeability of the material. We consider in the following the fields to have a harmonic time dependence. From Maxwell equations $\mathbf{E}$ and $\mathbf{H}$ are orthogonal. Then we get that the third Maxwell equation:
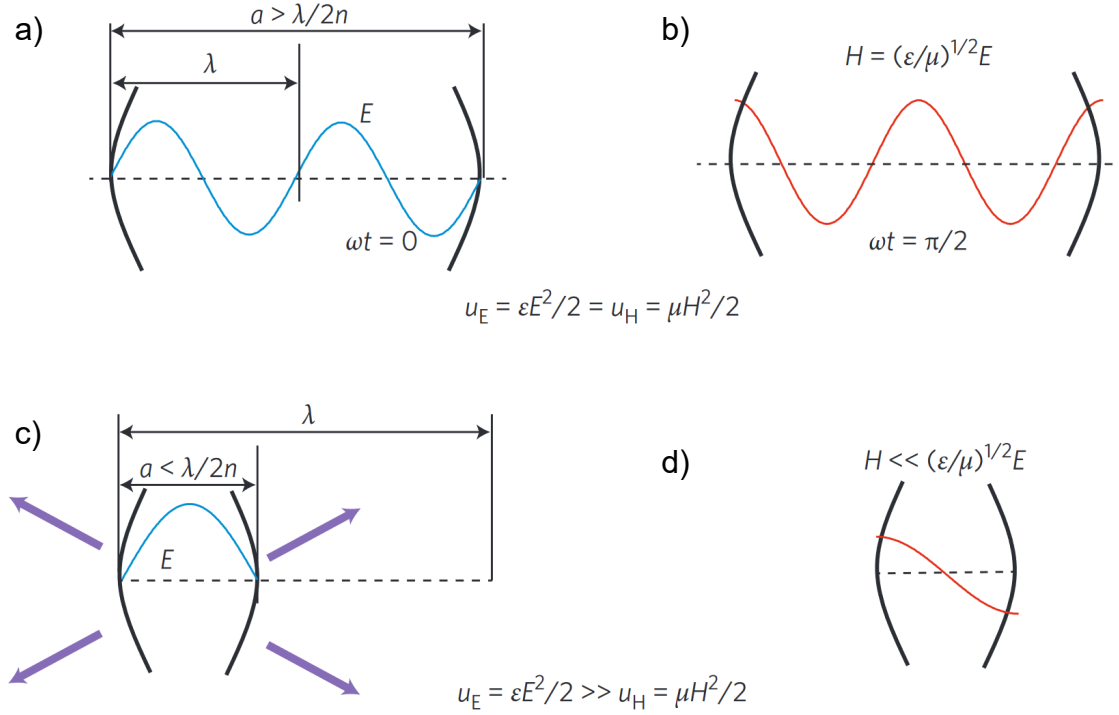
Figure 1.8: Self sustaining oscillations of the electric a) and magnetic b) fields in a resonator larger than the wavelength. For subwavelength structures the energy balance between electric c) an magnetic fields d) is not fulfilled anymore, leading to leakage radiation outside of the resonator. Adapted from [34].

$$\nabla \times \mathbf{E} = -\mu \frac{\partial \mathbf{H}}{\partial t} \tag{1.12}$$

is solved if $|\mathbf{H}| = \sqrt{\varepsilon/\mu}|\mathbf{E}|$. By substituting this relationship in the equations for the electric and magnetic energies, we see as expected that both have the same value $u_E = u_H$. This means that energy is periodically exchanged between the electric and magnetic fields without losses, and self-sustaining oscillations are possible [34]. Note that the same result can be obtained by repeating the same procedure with the 4th Maxwell equation:

$$\nabla \times \mathbf{H} = \varepsilon \frac{\partial \mathbf{E}}{\partial t} \tag{1.13}$$

Now if the resonator size a is smaller than the wavelength, the spatial dependence will be of the form $\sin(\pi z/a)$, as shown in Figure 1.8 c, d). Then from eq.1.13 we can write that the magnitude of the fields are related by:

$$|\mathbf{H}| = \frac{2a}{\lambda}\sqrt{\frac{\varepsilon}{\mu}}|\mathbf{E}| \tag{1.14}$$

The magnetic energy can then be expressed as a function of the electric energy as:

$$u_H = \left(\frac{2a}{\lambda}\right)^2 u_E \tag{1.15}$$

For a deeply subwavelength resonator we have $a \ll \lambda$ and therefore $u_H \ll u_E$. In this case we have an energy imbalance, meaning that self-sustaining oscillations are not possible. This statement is nothing else than another from of the diffraction limit, saying that squeezing the light in a resonator is possible only down to a dimension $a = \lambda/2$. Initial energy stored in the resonator will be lost due to leakage radiation to the environment, as shown in Figure 1.8 c) by the outgoing arrows. In materials with $\text{Re}(\varepsilon) < 0$, the energy balance can be restored by considering the kinetic energy u_k associated with the movement of free-charges $u_E = u_H + u_K$. These are electrons in metals and the ionic bonds in polar dielectrics. The kinetic term naturally adds in phase with the magnetic term, as currents are also out of phase with the electric field. From this argument, it follows that subwavelength resonators are inevitably lossy, as energy is stored almost half of the time as kinetic energy, which is lost at a rate commensurable with the scattering rate γ of the oscillating charges [34].

By applying the same reasoning used before for the subwavelength resonator, but using eq.1.12 instead of eq. 1.13, an apparent contradiction arises, as one gets $u_E \lll u_H$ in this case. This just means that the situation can also be treated from the opposite side, to restore energy balance one needs to have a source of additional potential energy oscillating in phase with **E**. However it is less straightforward how this can be done, other than just rising the value of u_E by increasing ε until the diffraction limit condition again applies [34].

1.5   Surface plasmon\phonon polaritons

In the previous sections we highlighted the need for materials with $\text{Re}(\varepsilon) < 0$ to achieve subwavelength confinement, and introduced SPP and SPhPs. While the dispersion curves for both types of SW are similar, many differences exist between the two, which we summarize in the following.

The first obvious difference is that, as can be seen from Figure 1.6, SSP exist at every wavelength below ω_p, while SPhP exist only in the Reststrahlen band. Moreover, if one is interested in deep subwavelength confinement, the wavelength of operation has to be close to $\text{Re}(\varepsilon) = 0$, as shown in Figure 1.7. This in not only true for surface modes, but also for localized resonances. For example, a simple rod antenna of length L has the lowest order resonance at $\lambda_{res} = L/2$ for $\text{Re}(\varepsilon) \ll 0$. Only when the permittivity approaches zero this simple relationship breaks down and subwavelength resonators become possible [35]. From the energy balance point of view, the $\text{Re}(\varepsilon) \ll 0$ condition corresponds to a low amount of energy stored as electron kinetic energy, only negligibly affecting the balance between electric and magnetic energy. The result is that the minimum size of a resonator is only slightly smaller than what determined by the diffraction limit. In turn, this means that losses are low at long wavelengths in metallic antennas, as only a small amount of energy is lost by electron collisions. While SPhPs naturally exist only in the mid-infrared
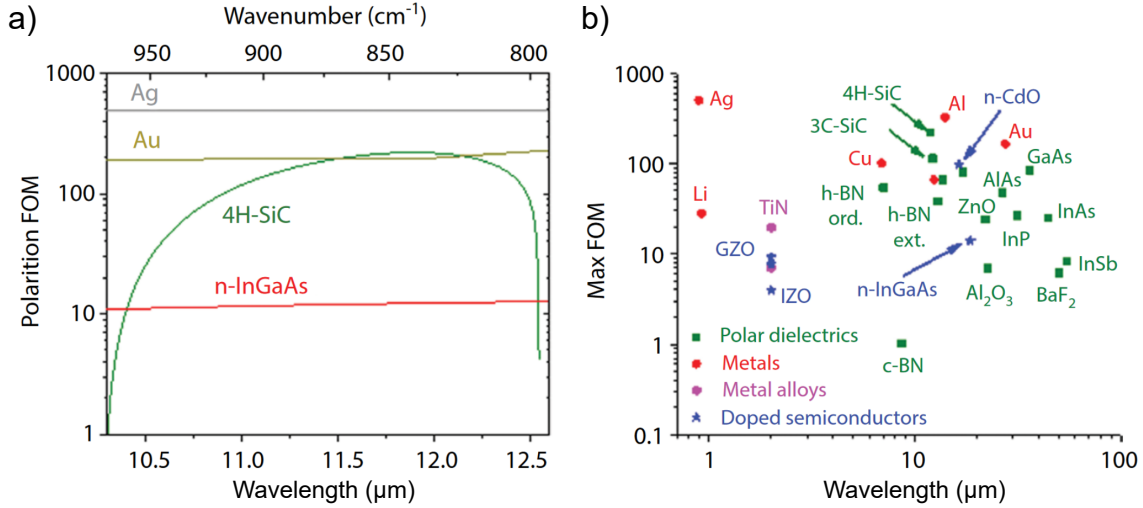
Figure 1.9: a) Figure of merit calculated from eq. 1.16 for two noble metals (Au, Ag), a doped semiconductor (n-InGaAs) and a polar dielectric (SiC). b) Maximum of the figure of merit for a selection of materials supporting both SPP and SPhP as a function of the frequency where the maximum is achieved. Adapted from [22]

(MIR) range, noble metal plasmonic structures produce the highest confinement at visible frequencies [36]. The different wavelength ranges can be bridged by doped semiconductors, which can have ω_p in the MIR [21], facilitating a direct comparison between SPP and SPhP.

The main property that has led to extensive study of SPhP is the lower losses in polar dielectrics. As we have seen from the energy balance approach in section 1.4, independently of the resonator shape the losses are determined by the scattering rate of the oscillating charges in the material. For noble metals, the intrinsic scattering rate is on the order of 10^{14} s^{-1}, while for doped semiconductors it can be an order of magnitude less due to the lower electron density [37]. However, the higher skin depth of doped semiconductors leads to comparable or even grater losses than in noble metals [37]. In this regard, SPhP offer great advantage since the loss mechanism is not related to electron-electron scattering but to phonon-phonon scattering, which is a much slower process. While SPP have lifetimes on the order of tens of femtoseconds, SPhP can reach three order of magnitude longer lifetimes of tens of picoseconds.

1.5.1 SPhP and SPP comparison

A number of figure of merits can be established to compare the properties of localized and surface resonances among different material platforms. We start here by considering surface waves, for which a common figure of merit (FOM) is the ratio between the propagation length L and the out-of plane confinement of the mode in the dielectric side δ. This figure of merit is chosen because the confinement for a certain material choice can be tuned arbitrarily by reducing the thickness of the dielectric layer in a metal-insulator-

metal (MIM) arrangement. By normalizing to the wavelength of operation, the FOM for SW can be expressed as [22]:

$$\text{FOM}_{SW} = \frac{L_p/\lambda}{2\delta/\lambda} \approx \frac{|\text{Re}(\varepsilon)|^{3/2}}{\text{Im}(\varepsilon)} \quad (1.16)$$

Eq. 1.16 is plotted in Figure 1.9 a) for the two most common noble metals (Ag and Au), a highly doped semiconductor (n-InGaAs) and a polar dielectric (SiC, polytype 4H) supporting SPhPs. The frequency range is the one of the RS band of SiC. It can be seen that SPhP in SiC do not outperform conventional noble metals, and only have the drawback of the limited frequency range. Even though the losses in SiC are much lower than for the plasmonic systems and the SPhP lifetime greatly increased, the FOM is low due to the low group velocity of SPhPs. The group velocity of a SW is calculated as $v_g = \partial\omega/\partial k$, and consequently v_g is small for SPhP due to their strong dispersion, balancing the increased lifetime. In Figure 1.9 b) the maximum of eq. 1.16 is reported for many materials supporting both SPPs and SPhPs. For each material the maximum of the FOM is reported together with the frequency value where such maximum is achieved. From this figure one can conclude that no particular advantage of SPhPs over SPP in metals or doped semiconductors can be clearly established.

On the other hand, the argument that the SW performance of a material can be estimated regardless of the confinement, misses the fact that the scaling of the k-vector for the MIM or IMI insulator-metal-insulator (IMI) geometries is not a linear function of the dielectric layer or metal film thickness. We consider here for example the IMI geometry for a SiC and a gold thin films in an homogeneous medium. For simplicity we analyze here only the lower energy mode arising in the MIM geometry due to hybridization of the top and bottom SW in a thin film [15]. As we are far away from interband transitions, for the dielectric function of gold we use a simple Drude model with $\omega_p = 70\,500\,\text{cm}^{-1}$ and $\gamma = 150\,\text{cm}^{-1}$ [38]. For the SiC dielectric function we use values taken from the literature [39]. In Figure 1.10 a) we show the calculated SPhP wavelength for a 200 nm SiC film suspended in vacuum. Such films can be experimentally realized and are even commercially available as millimeter-scale free-standing membranes [39]. To achieve a comparable level of confinement in the propagation direction with a gold film, its thickness has be of only 0.2 nm, as shown in Figure 1.10 a). This means that while theoretically the same confinement can be reached with a gold film, this is not actually feasible. Regardless of the difficulty of actually achieving such a small film thickness, at such sub-nanometer scales quantum effects start to play a role [40], invalidating this simple treatment based exclusively on Maxwell's equations. In Figure 1.10 b) we plot the ratio of the propagation length L to the SW wavelength λ_{SW} for the same films as in a). Even if the same confinement could be achieved, the losses for SPP are much higher, and the intensity decays a factor of e before completing even a single oscillation. In Figure 1.10 b) we calculate the FOM as defined in eq. 1.16 for the SiC and gold thin films. While the FOM in the bulk case slightly favours gold over SiC (see Figure 1.9 a), in the thin film case it is the opposite. This shows that the FOM used for a semi-infinite surface does not capture the correct behaviour for
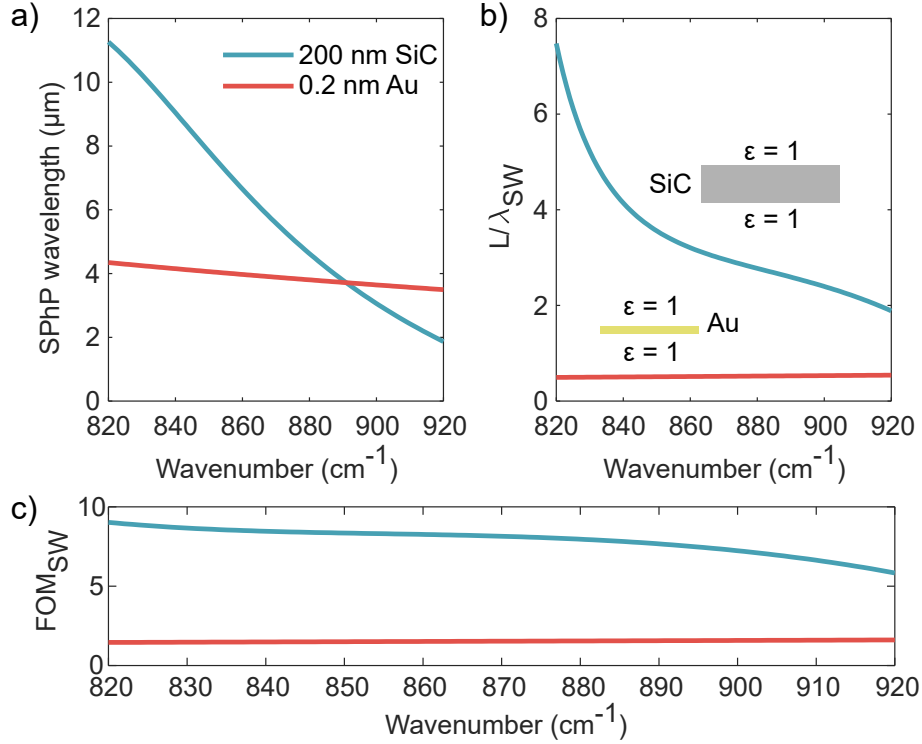
Figure 1.10: a) Calculated wavelength for SPhP in a 200 nm SiC film and SPP in a 0.2 nm Au film. In both cases the films are suspended in vacuum as shown in the inset in b). b) Calculated ratio between the propagation length L and SW wavelength λ_{SW} for the films in a). c) Calculated FOM from eq. 1.16 for the thin films.

the IMI geometry.

1.5.2   LSPhP and LSPP comparison

In the previous section we compared propagating modes in different materials with $\mathrm{Re}(\varepsilon) < 0$. We review here the properties of localized resonances in plasmonic (LSPP) and phononic (LSPhP) antennas. To evaluate the intrinsic material properties we consider a deeply sub-wavelength $a \ll \lambda$ spherical antenna of radius a. The polarizability of a sphere in vacuum in the quasi-electrostatic approximation (i.e. the driving field is considered constant over the whole particle) has a simple analytical expression [15]:

$$\alpha = 4\pi a^3 \frac{\varepsilon - 1}{\varepsilon + 2} \tag{1.17}$$

Eq. 1.17 has a maximum at $\mathrm{Re}(\varepsilon(\omega)) = -2$, the so-called Fröhlich condition. It can be shown that the quality factor (Q) of an electrostatic mode depends on the resonant wavelength, but is independent of the detailed geometry of the resonator [22]. The Q factor can then be expressed only in terms of the dielectric function of the material:
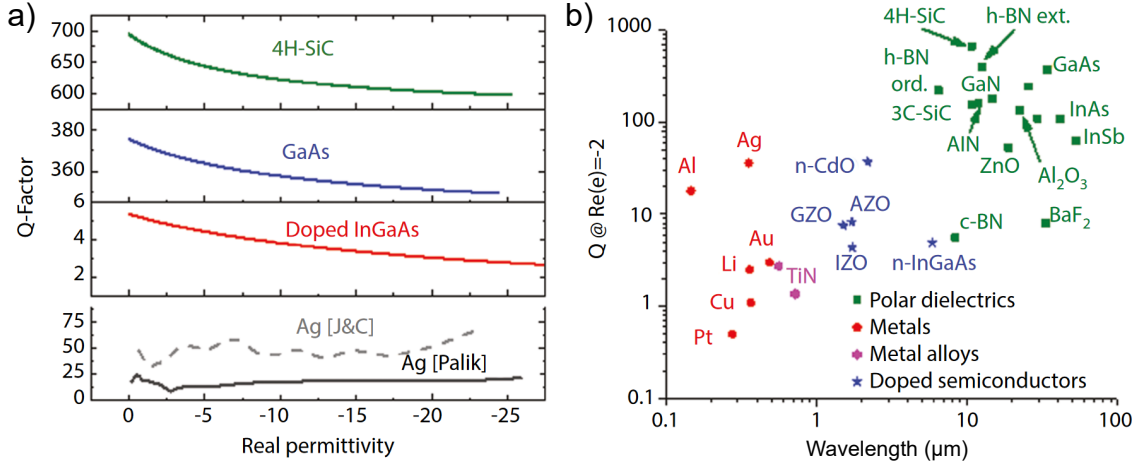
Figure 1.11: a) Calculated Q-factor in the electrostatic limit for LSPhP in polar dielectrics (SiC and GaAs) ans LSPP in a doped semiconductor (InGaAs) and a noble metal (Ag), as a function of $\mathrm{Re}(\varepsilon)$. b) Q-factor at the Fröhlich condition for materials supporting LSPP (metals, metal alloys and doped semiconductors) and LSPhP (polar dielectrics).

$$Q = \frac{\omega \mathrm{dRe}(\varepsilon)/\mathrm{d}\omega}{2\mathrm{Im}(\varepsilon)} \approx \frac{\omega}{\gamma} \tag{1.18}$$

where the approximation is valid for $\gamma \ll \omega_{LO} - \omega_{TO}$ for LSPhP and $\gamma \ll \omega_p$ for LSPP. The Q-factor in different material platforms can then be compared, as shown in Figure 1.11 a) as a function of the real part of the permittivity. The advantage of using materials supporting phonon polaritons is then clear in this case, as the Q-factor for LSPhP (4H-SiC and GaAs) is much higher than for LSPP in doped semiconductors (InGaAs) and noble metals (Ag). The Q-factor for a selection of materials is shown in 1.11 b) at the Fröhlich condition. Almost all polar-dielectrics outperform even the best plasmonic materials, while having resonance frequencies in the mid to far-IR region. Even though the Q-factor for LSPhP resonances is roughly one order of magnitude higher than for LSPP at similar frequencies, it has been shown that the increase in field enhancement and Purcell factor is not as high. This has been explained by considering that a large amount of energy in the SPhP antenna is stored as potential energy of the ions, which does not contribute to the enhancement of the external field and has no analogue in LSPP resonators [37].

1.5.3 Anisotropy

Until now we discussed the propagation of SW in isotropic systems, where the the dielectric tensor $\varepsilon_{i,j}$ is diagonal and all its terms are equal. However, there are materials in which the diagonal elements $\varepsilon_{i,i}$ can have different values. In dielectric materials, this is the origin of birefringence, which is the principle on which waveplates are built. The difference in the refractive index along different crystal directions introduces a phase delay between

orthogonal polarizations which depends on the relative angle between the crystal axis and the polarization direction. In materials supporting SPhPs and SPPs, if not all the terms are equal in magnitude, SW propagating in different directions will have different wavelengths. In momentum space, the wavevector surface is a sphere for isotropic materials, and an ellipsoid for anisotropic materials with all the diagonal elements $\varepsilon_{i,i} < 0$. More interestingly, it can also happen that for a certain frequency range some terms of the dielectric tensor are positive and some are negative, resulting in a k-vector surface which has the shape of an hyperboloid [42]. Hyperbolic response can arise from various combinations of Drude and Lorentz responses along different crystal directions, as shown in Figure 1.12 a) when considering only 2 independent components of the dielectric tensor. [42]. Howevever, for plasmonic materials such hyperbolic iso-momentum curves have been only recently observed in thin films of tungsten ditelluride (WTe2) in the mid-IR [43], but no direct imaging of hyperbolic SPPs has been carried so far. On the other hand exfoliated hBN, which is one of the most common materials for phonon polaritons, exhibits out-of plane hyperbolicity [44]. Since SPhP arise from the phonon structure of the lattice, anisotropic behaviour can be expected in a wide range of materials exhibiting highly anisotropic unit cells. 2D materials have attracted considerable attention in this context since they feature high anisotropy in the out-of plane direction, which allows exfoliation, and can also feature in-plane anisotropy. In-plane hyperbolic response has been recently discovered in different phononic materials, including α-MoO$_3$ [45, 46] and α-V$_2$O$_5$ [47], where anisotropic SPhP propagation was demonstrated through real-space near-field imaging. Recent experiments increased even more the possibility of engineering the phonon polariton response by twist-angle of stacked 2D materials [41] and by employing crystals with nonzero off-diagonal elements of the dielectric tensor [48, 49], which have, at the moment, no counter part in plasmonic systems. In Figure 1.12 b-d) the response of a heterostructure made by stacking two layers of α-MoO$_3$ with a certain twist angle between the layers is shown [41]. The in-plane dispersion has a topological transition from hyperbolic to elliptical as a function of twist angle. At a certain "magic angle" the SPhP are launched in a single direction, corresponding to the presence of "flat bands" in the in-plane dispersion, as shown in Figure 1.12 c, d). The topological transition is determined by the number of intersections between the in-plane dispersions of the individual layers, as shown by the dashed lines in Figure 1.12 d) and the value of N_{ACP}.

It is worth mentioning that, while anisotropy can be obtained in artificial metamaterials and metasurfaces, the maximum in-plane momentum of the SW is in this case limited by the size of the artificial unit cell [43].
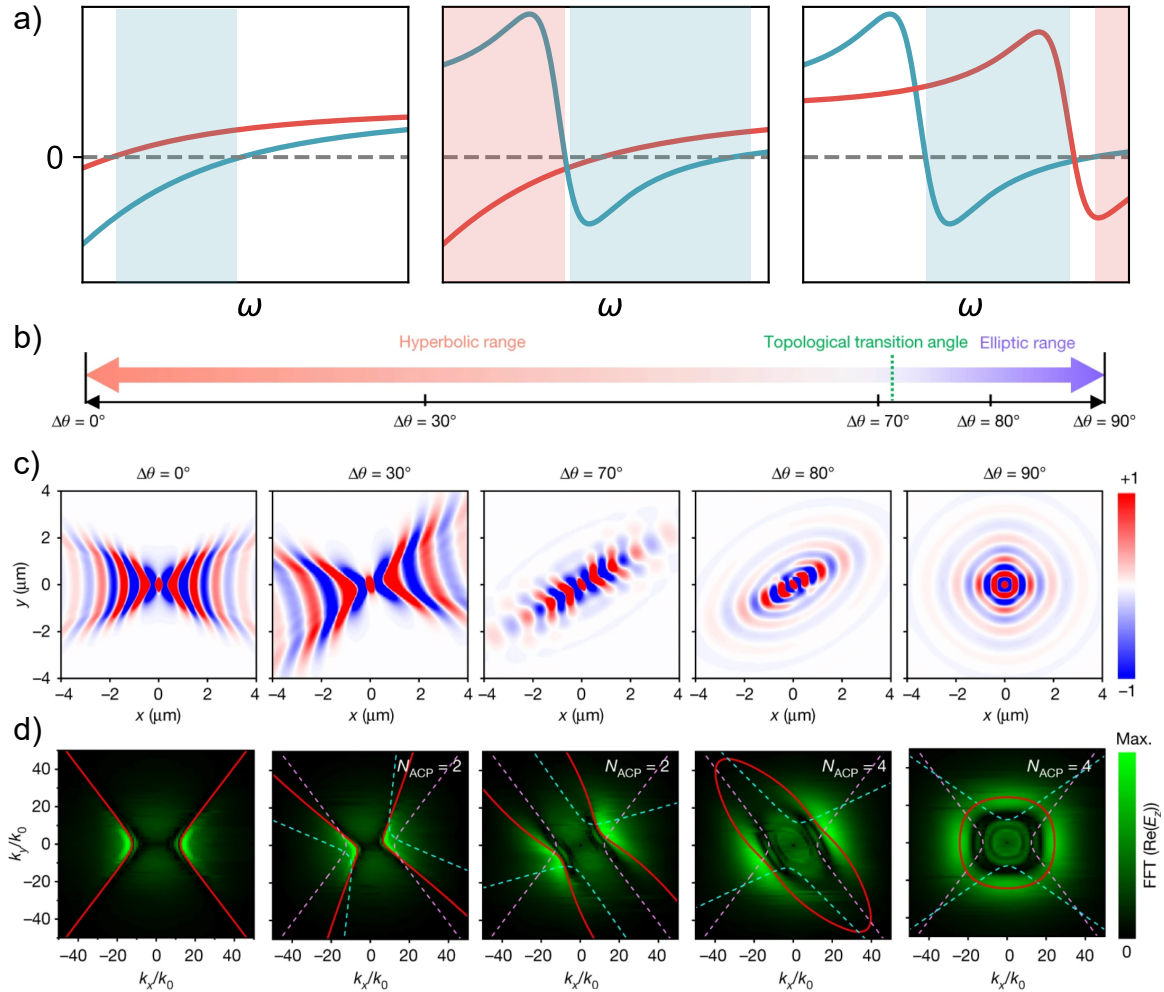
Figure 1.12: a) Different ways to obtain hyperbolic response in a natural material by a combination of Drude-Drude, Drude-Lorentz and Lorentz-Lorentz responses. The regions of hyperbolic response are highlighted in blue and red. b) Topological transition in the SPhP dispersion of two layers of α-MoO$_3$ as a function of the twist angle. c) Simulated out of plane electric field $\text{Re}(E_z)$ of a dipole emitting above the α-MoO$_3$ heterostructure as a function of twist angle and d) corresponding amplitude of the fourier transform. Dashed lines indicate the dispersion of the individual layers, while the red line is the heterostructure dispersion. Adapted from [41].

Chapter 2

Theory

Maxwell's equations describe electromagnetic fields, and all the phenomena investigated in this work can be described through their application with certain boundary conditions and material discontinuities. Analytical solutions of Maxwell's equations exist only for a very limited number of examples, and often numerical solutions are required. We review first the solution of Maxwell equations in layered stacks of uniform materials, which for example describe the behaviour of anti-reflection coatings based on thin-film interference. In the context of this work, layered geometries are of relevance to understand the properties of SPhP in complex heterostructures. We then move to arbitrary three dimensional geometries where numerical methods have to be used, and in particular we highlight the differences between finite difference time domain (FDTD) and finite element methods (FEM).

2.1 Maxwell equations in 2D layered geometries

2.1.1 Single interface

When light encounters a material boundary it gets reflected back into the initial medium and refracted inside the second one. The intensity of reflected and refracted lights depend on the refractive index of the materials and on the angle of incidence of light with respect to the normal direction of the surface. The refractive index $\hat{n} = n + ik$ serves the same purpose of the dielectric function ($\varepsilon = \varepsilon_1 + i\varepsilon_2$) to describe the em response of a material. These two quantities are related by:

$$\begin{aligned} \varepsilon_1 &= n^2 - k^2 \\ \varepsilon_2 &= 2nk \end{aligned} \tag{2.1}$$

The problem can be solved by considering a plane wave incident with an angle θ_i on the discontinuity and imposing various boundary conditions. The electric **E** and magnetic **H** fields for a plane wave can be written as:
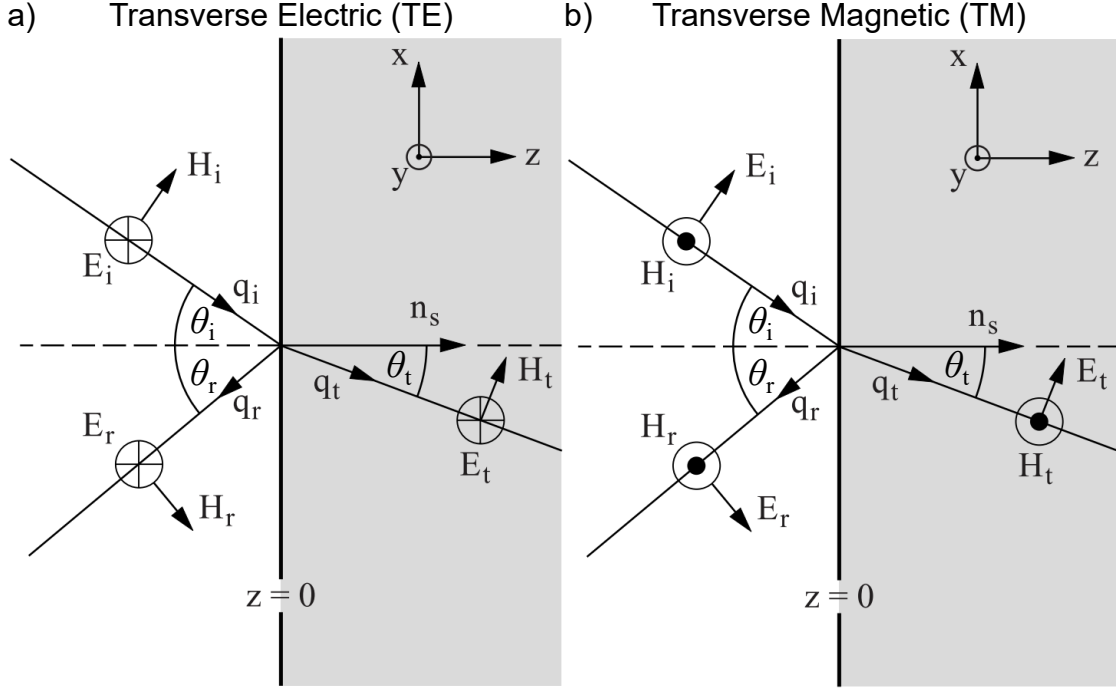
Figure 2.1: Scheme for the transmitted and reflected waves for TE a) and TM b) incidence at an interface between two materials with different refractive index. Adapted from [23].

$$\begin{aligned}
\mathbf{E}_i &= \mathbf{E}_{0i} e^{i(\mathbf{q}_i \cdot \mathbf{r} - \omega_i t)} \\
\mathbf{H}_i &= \mathbf{n}_{\mathbf{q}i} \times \mathbf{E}_i
\end{aligned} \tag{2.2}$$

where $\mathbf{n}_{\mathbf{q}i}$ is the unit vector in the direction of $\mathbf{q}_i$ and i is the material index. A series of boundary conditions can be enforced on the fields in eq. 2.2 to derive the Fresnel coefficients for the reflected and transmitted light. First of all the frequency of the wave is the same for all components ($\omega_i = \omega_t = \omega_r$), and the phase term at the interface must be the same ($\mathbf{q}_i \cdot \mathbf{r} = \mathbf{q}_r \cdot \mathbf{r} = \mathbf{q}_t \cdot \mathbf{r}$). The indexes i, r, t indicate the incident, reflected and transmitted parts. From these relations one can conclude that light is reflected at the same angle of incidence, and derive Snell's law for refraction of light:

$$\frac{\sin(\theta_i)}{\sin(\theta_t)} = \frac{\hat{n}_t}{\hat{n}_i} \tag{2.3}$$

Continuity at surface of the normal components of $\mathbf{D}$ and $\mathbf{B}$ and of the tangential components of $\mathbf{E}$ and $\mathbf{H}$ is used to derive Fresnel's equations [23]. The transmission and reflection coefficients are different for TM waves ($\mathbf{E}$ has a component perpendicular to the surface) and TE waves ($\mathbf{E}$ is parallel to the surface). The difference between TE and TM incidence is illustrated in Figure 2.1. The Fresnel coefficients read [23]:

$$r_{TE} = \frac{\hat{n}_1 \cos\theta_i - \hat{n}_2 \cos\theta_t}{\hat{n}_1 \cos\theta_i + \hat{n}_2 \cos\theta_t}$$

$$t_{TE} = \frac{2\hat{n}_1 \cos\theta_i}{\hat{n}_1 \cos\theta_i + \hat{n}_2 \cos\theta_t}$$

$$r_{TM} = \frac{\hat{n}_2 \cos\theta_i - \hat{n}_1 \cos\theta_t}{\hat{n}_2 \cos\theta_i + \hat{n}_1 \cos\theta_t}$$

$$t_{TM} = \frac{2\hat{n}_1 \cos\theta_i}{\hat{n}_2 \cos\theta_i + \hat{n}_1 \cos\theta_t}$$

(2.4)

Together with Snell law, eqs. 2.4 can be rewritten as only a function of the incidence angle θ_i. The Fresnel coefficients in 2.4 are complex quantities as they describe both the change in amplitude and phase of the electric field at the boundary. The well know phenomena of total internal internal reflection and polarized reflectivity at the Brewster angle are described by eq. 2.4.

The intensity of the reflected light can be calculated as the square of the corresponding Fresnel coefficient $R = |r|^2$, and the transmitted portion is obtained as $T = 1 - R - A$, where A represent absorption losses. In the special case of normal incidence there is no difference between TE and TM incidence. If one of the materials is vacuum as in most experiments, the reflectivity can be written as [23]:

$$R = \left|\frac{1-\hat{n}}{1+\hat{n}}\right|^2 = \frac{(1-n)^2 + k^2}{(1+n)^2 + k^2}$$

(2.5)

and the associated phase shift ϕ_r is

$$\tan\phi_r = \frac{-2k}{1 - n^2 - k^2}$$

(2.6)

2.1.2 Layered systems

The discussion carried in the previous section for the reflection and transmission at a single interface can be extended to multilayer systems. In the case of multiple interfaces, the incident light can interfere with the reflection from subsequent layers, resulting in thin-film interference effects. This is a particularly strong effect for multilayers of thickness larger than the wavelength but smaller than the skin depth, so that a considerable amount of light is reflected at each interface. The simplest version of a multilayer system is constituted by three different materials with two interfaces, with the material in the middle characterized by a thickness T. The problem can be solved for isotropic and homogeneous mediums by casting Maxwell equation in matrix form [50].

The derivation of the matrix formulation in quite lengthy, so we only briefly summarize it here. In the case of TE waves with incidence in the yz plane, where z is the direction of stratification, one has $E_z = E_y = 0$. A single second order differential equation can be
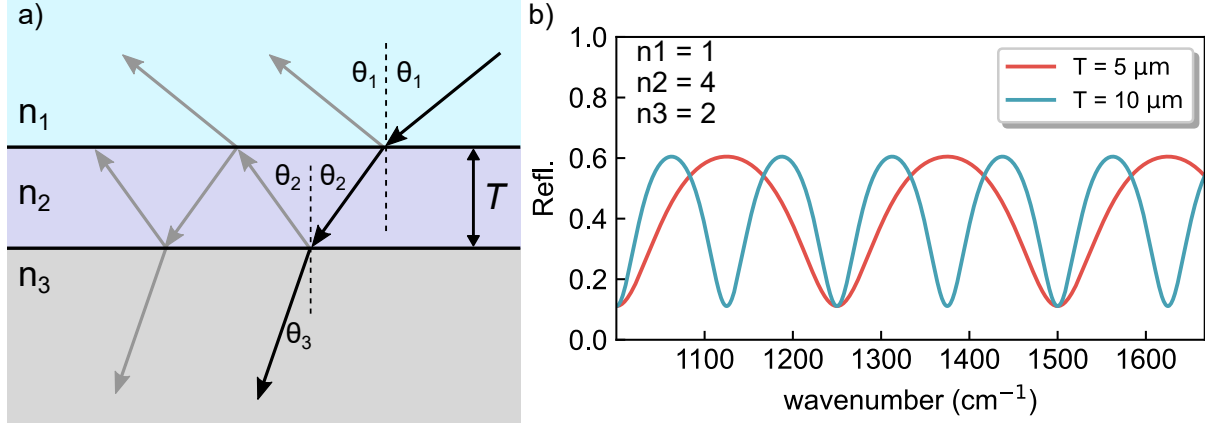
Figure 2.2: a) Scheme for a three layer system with $n_1 < n_3 < n_2$. Multiple reflections are shown as gray arrows. b) Reflectivity for a three layer system as calculated from eq. 2.17 for two different thicknesses of the middle layer for $\theta_1 = 0$.

written for E_x starting from Maxwell equations, which can be shown to have a solution of the form [50]:

$$\mathbf{E_x} = U(z)e^{i(k_0\alpha y - \omega t)} \tag{2.7}$$

where $U(z)$ is an unknown function of z and $\alpha = n\sin\theta$ where θ in the incidence angle. Analogously it can be shown that for the H field:

$$\mathbf{H_y} = V(z)e^{i(k_0\alpha y - \omega t)}$$
$$\mathbf{H_z} = W(z)e^{i(k_0\alpha y - \omega t)} \tag{2.8}$$

The problem is then reduced to finding the unknown functions $U(z)$, $V(z)$ and $W(z)$. The functions $U(z)$ and $W(z)$ are related by $\alpha U + \varepsilon W = 0$, so that the problem is reduced to the solution of two independent second order differential equations for $U(z)$ and $V(z)$. The value of the functions $U(z)$, $V(z)$ and their initial value $U(0)$, $V(0)$ are related by a 2×2, matrix which depends on the properties of the material [50]:

$$\mathbf{Q_0} = \mathbf{MQ} \tag{2.9}$$

where

$$\mathbf{Q_0} = \begin{bmatrix} U(0) \\ V(0) \end{bmatrix}, \qquad \mathbf{Q} = \begin{bmatrix} U(z) \\ V(z) \end{bmatrix} \tag{2.10}$$

The advantage of this formulation, which goes under the name of transfer-matrix method, is that the effect of multiple layers can be expressed as the product of the matrices characteristic of each layer. If we consider a series of N layers extending from $0 \le z \le z_1$, $z_1 \le z \le z_2$, $\cdots z_{N-1} \le z \le z_N$ one has:

$$\mathbf{Q}_0 = \mathbf{M}(z_N)\mathbf{Q}(z_N) \tag{2.11}$$

where $\mathbf{M}(z_N) = \mathbf{M}_1(z_1)\mathbf{M}_2(z_2 - z_1)\cdots\mathbf{M}_2(z_N - z_{n-1})$. It can be shown that for a single layer the characteristic matrix has the form [50]:

$$\mathbf{M}(z) = \begin{bmatrix} \cos(k_0 nz \cos(\theta)) & -\frac{i}{p}\sin(k_0 nz \cos(\theta)) \\ -ip\sin(k_0 nz \cos(\theta)) & \cos(k_0 nz \cos(\theta)) \end{bmatrix}, \tag{2.12}$$

where $p = \sqrt{\varepsilon}\cos(\theta)$. We consider for simplicity a non-magnetic medium with $\mu = 1$. According to eq. 2.7, the electric field depends only on the function U. Therefore for TE waves, $U_0 = A + R$ represents the sum of the reflected R and incident A amplitudes of the electric field, while $U(z) = T$ represents the transmitted part. Then by applying eq. 2.7:

$$\begin{bmatrix} U_0 \\ V_0 \end{bmatrix} = \begin{bmatrix} m_{11}U(z) + m_{12}V(z) \\ m_{21}U(z) + m_{22}V(z) \end{bmatrix} \tag{2.13}$$

where m_{ij} are the elements of the characteristic matrix. For continuity of the fields at the boundary one also has that the electric and magnetic fields are related by $\mathbf{H} = \sqrt{\varepsilon}\hat{k} \times \mathbf{E}$, where $\hat{k}$ is the unit vector in the propagation direction. Then one has for the field amplitudes $V(z) = p_t U(z) = p_t T$ and $V_0 = p_r(A - R)$, where the indexes r and t indicate the two mediums where light is reflected and transmitted. Therefore one can write:

$$\begin{aligned} A + R &= (m_{11} + p_t m_{12})T \\ p_r(A - R) &= (m_{21} + p_t m_{22})T \end{aligned} \tag{2.14}$$

From these the reflection and transmission coefficients can be retrieved as:

$$\begin{aligned} r &= \frac{R}{A} = \frac{(m_{11} + p_t m_{12})p_r - (m_{21} + p_t m_{22})}{(m_{11} + p_t m_{12})p_r + (m_{21} + p_t m_{22})} \\ t &= \frac{T}{A} = \frac{2p_r}{(m_{11} + p_t m_{12})p_r + (m_{21} + p_t m_{22})} \end{aligned} \tag{2.15}$$

In the case of $z = 0$ (i.e. a single interface), eq. 2.4 for TE waves is recovered, as the matrix elements are $m_{11} = m_{22} = 1$ and $m_{12} = m_{21} = 0$. The solution for TM waves is obtained by substitution of the p terms with $q = \sqrt{1/\varepsilon}\cos(\theta)$. For a three layer system (indicated with indexes $1, 2, 3$), where a film of thickness T is sandwiched between two layers as shown in Figure 2.2 a), the matrix elements according to eq. 2.11 are:

$$m_{11} = m_{22} = \cos\beta, \qquad m_{12} = -\frac{i}{p_2}\sin\beta, \qquad m_{21} = -ip_2\sin\beta \tag{2.16}$$

where $\beta = 2\pi n_2 T \cos(\theta_2)/\lambda_0$ and $p_j = n_j \cos(\theta_j)$. The angles of the transmitted wave in each medium are indicated as θ_j. By substituting the matrix elements in eq. 2.15 the

reflection and transmission coefficients can be expressed as a function of the single interface coefficients r_{12}, r_{23} and t_{12}, t_{23} as [50]:

$$r = \frac{r_{12} + r_{23}e^{2i\beta}}{1 + r_{12}r_{23}e^{2i\beta}}$$
$$t = \frac{t_{12} + t_{23}e^{i\beta}}{1 + r_{12}r_{23}e^{2i\beta}}$$

(2.17)

The reflectivity and transmissivity of the three layer system are then simply $R = |r|^2$ and $T = p_3|t|^2/p_1$. TM and TE coefficients are obtained by considering the appropriate single interface TE and TM coefficients r, t in eqs. 2.17.

An interesting phenomena related to multilayer films is the thin film interference effect. As can be understood from simply applying Snell law to the multilayer shown in Figure 2.2 a), due to different optical paths of the reflected rays in the upper medium, either constructive or destructive interference can be achieved. Neglecting phase retardation due reflection and transmission at the interfaces, constructive interference is achieved whenever $m\lambda = 2n_2T\cos(\theta_2)$. If plotted against the inverse of the wavelength, the periodicity of the fringes in a spectrum is given by:

$$\Delta = \frac{1}{2n_2T\cos(\theta_2)}$$

(2.18)

If the refractive index of the materials in the stack is known, from the periodicity of the fringes the film thickness can be inferred. An example of the effect of thin-film interference on the spectrum of a three-layer system is shown in Figure 2.2 b) for two different film thicknesses.

2.1.3 Extension to anisotropic materials

The transfer-matrix formalism summarized in the previous section can be used to compute the reflectivity and transmissivity of an arbitrary number of layers. However it cannot treat anisotropic materials, which are often interesting in the study of phonon polartions [44,45]. A formalism that can treat at the same time isotropic and anisotropic layers (with diagonal dielectric tensors) has been recently developed [51]. The method has been conceived to simulate experiments employing the Otto geometry, where light is coupled into a high index-prism in total internal reflection. The prism is brought close to the interface under study, so that the sample is excited by the exponential tail of the TIR in the prism, allowing the investigation of high in-plane momenta surface waves. This method can be used to predict SWs dispersions in complex stacks of layered anisotropic materials.

The main difference from the previous treatment is that the dielectric constant relating the field inside the material to the total field is not a scalar constant but a diagonal matrix. Therefore the effect of a layer cannot be described anymore by a 2×2 matrix, but a 4×4 matrix has to be considered. The incident field is assumed to lie in the $x - z$

plane and the wavevector in each layer i can be written as $\mathbf{k_i} = \omega/c(\sqrt{\varepsilon_{inc}}\sin(\theta), 0, q_i)$, where ε_{inc} is the isotropic dielectric function of the incident medium and θ is the angle of incidence. Then, Maxwell's equations considering harmonic time dependencies and neglecting nonlinear effects can be written as [51]:

$$\mathbf{R}\begin{bmatrix}E_x \\ E_y \\ E_z \\ H_x \\ H_y \\ H_z\end{bmatrix} = -i\omega\begin{bmatrix}D_x \\ D_y \\ D_z \\ B_x \\ B_y \\ B_z\end{bmatrix} \tag{2.19}$$

where $\mathbf{R}$ is a 6×6 matrix representing the spatial derivatives in Maxwell's equations, while temporal derivatives have been already computed, giving the $-i\omega$ term. It can be shown that the normal components E_z and H_z can be solved in terms of the other four field components, and Maxwell's equations can be rewritten as:

$$\frac{\partial}{\partial z}\begin{bmatrix}E_x \\ H_y \\ E_y \\ -H_x\end{bmatrix} = i\frac{\omega}{c}\mathbf{\Delta}\begin{bmatrix}E_x \\ H_y \\ E_y \\ -H_x\end{bmatrix} \tag{2.20}$$

where $\mathbf{\Delta}$ is a 4×4 matrix which is related in a non-straightforward way to the material parameters of the layer [51]. For each layer i, the 4 eigenvalues of $\mathbf{\Delta}(i)$ are the z-components of the wavevector q_{ij}. One can rewrite the previous equation as:

$$q_{ij}\Delta(i) = \Psi_{ij}\Delta(i) \tag{2.21}$$

where $\Psi = (E_x, H_y, E_y, -H_x)$. Here $j = 1, 2, 3, 4$ represents the different values of the wavevector due to different polarizations and propagation directions. The sign of q_{ij} distinguishes transmitted and reflected components. From the eigenvalues q_{ij} an appropriate 4×4 matrix $\mathbf{A}$ can be defined so that the in-plane fields of a layer can be related to the fields at the previous layer [51]:

$$\mathbf{A}_{i-1}\mathbf{E}_{i-1} = \mathbf{A}_i\mathbf{E}_i \tag{2.22}$$

where $\mathbf{E} = (E_{tr}^p, E_{tr}^s, E_{rfl}^p, E_{rfl}^s)$ so that the fields are distinguished by their polarization (p, s equivalent to TM and TE) and if they are reflected or transmitted. The full transfer matrix can then be expressed as:

$$\mathbf{\Gamma}_N = \mathbf{A}_0^{-1}\mathbf{T}_{tot}\mathbf{A}_{N+1} \tag{2.23}$$

where

$$\mathbf{T}_{tot} = \prod_{i=1}^{N}\mathbf{T}_i = \prod_{i=1}^{N}\mathbf{A}_i\mathbf{P}_i\mathbf{A}_i^{-1} \tag{2.24}$$
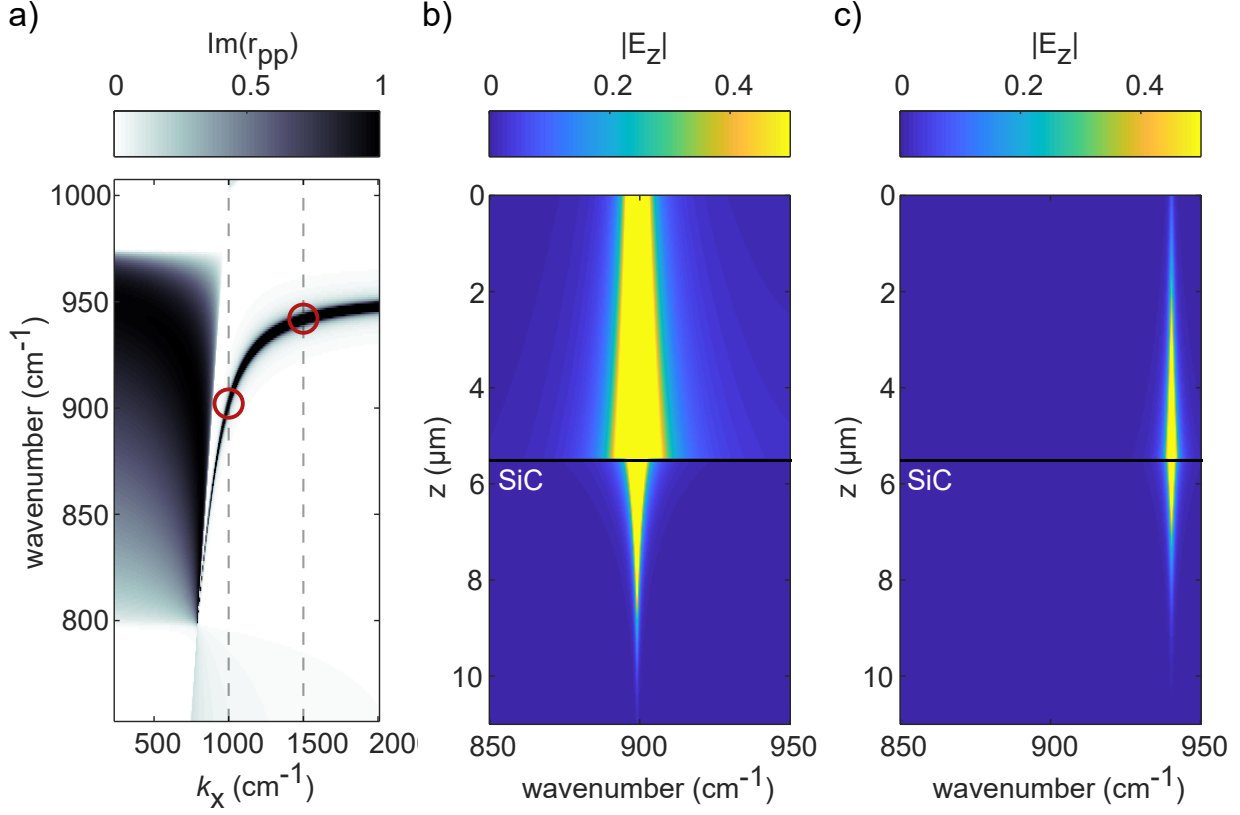
Figure 2.3: a) Dispersion of the SPhP on a semi-infinite SiC surface in vacuum calculated through the transfer-matrix method. $\mathrm{Im}(r_{pp})$ is shown in the colorbar. Vertical dashed lines indicate the in-plane momentum used for the calculations in b) and c), while red circles indicate the frequency of the SPhP at the corresponding momentum. Calculated absolute value of the out-of plane component of the field $|E_z|$ for in plane-momentum $k_x = 1000\,\mathrm{cm}^{-1}$ b) and $k_x = 1500\,\mathrm{cm}^{-1}$ c).

and $\mathbf{P}_i$ is the 4×4 propagation matrix of layer i where the diagonal matrix elements are given by $p_{ij} = \exp(-i\omega q_{ij} d_i / c)$, while the rest of the elements are 0. The in-plane electric fields at each interface can be calculated through eq. 2.22, and the fields at the top and bottom of the stacks are related by:

$$\mathbf{E}_0^- = \mathbf{\Gamma}_N \mathbf{E}_{N+1}^+ \tag{2.25}$$

where the $+$ and $-$ indicate the field at the upper or lower side of each interface. From the transfer matrix $\mathbf{\Gamma}_N$ the reflection and transmission coefficients can be calculated [51]. Each coefficient describes the reflected and transmitted for a determined input polarization and output polarization. The reflection coefficients are overall four: $r_{ss}, r_{sp}, r_{pp}, r_{ps}$ and the reflectivity is calculated as usual as the square modulus of the coefficients $R_{kl} = |r_{kl}|^2$. Similarly, one also has four transmission coefficients $t_{ss}, t_{sp}, t_{pp}, t_{ps}$. Since no reflected fields are present at the bottom of the stack, $\mathbf{E}_{N+1}^+$ can be written as:

$$\mathbf{E}_{N+1}^{+} = \begin{bmatrix} t_{pp} + t_{sp} \\ t_{ss} + t_{ps} \\ 0 \\ 0 \end{bmatrix} \tag{2.26}$$

The fields at each point z of layer i can then be calculated by applying the propagation matrix $P_i(z)$ to the fields at the interface:

$$\mathbf{E}_i(z) = \mathbf{P}_i(z)\mathbf{E}_i^{-} \tag{2.27}$$
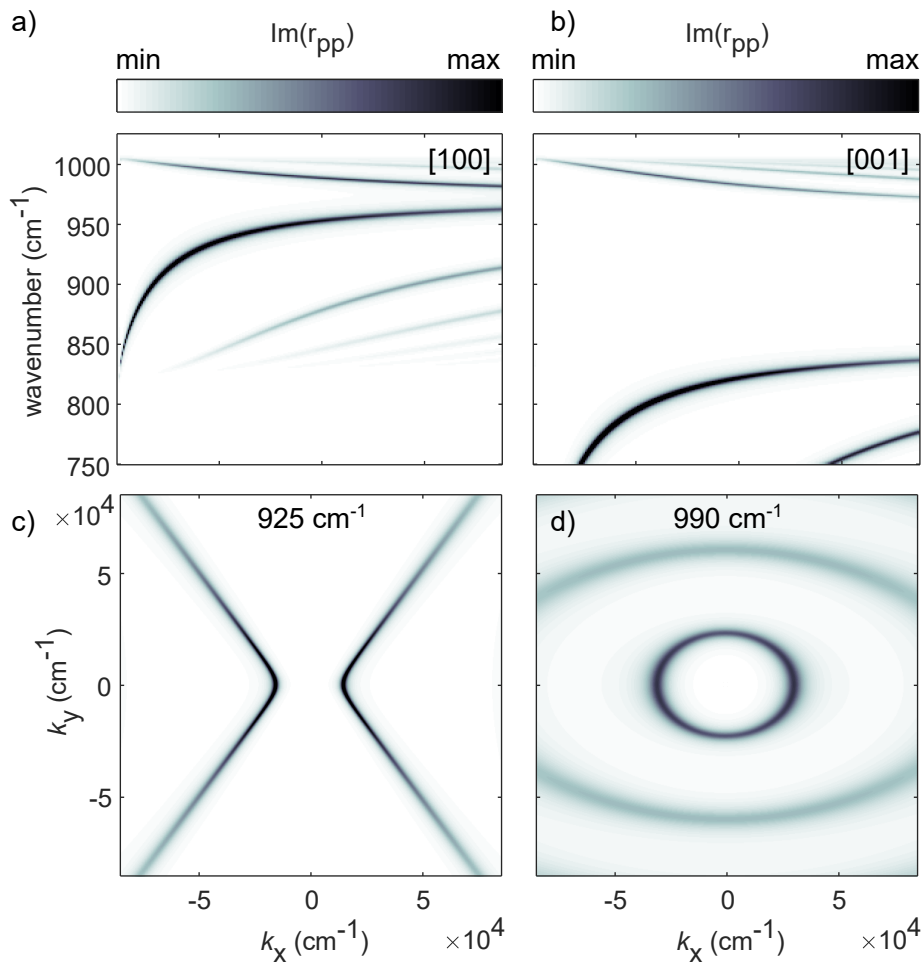
Figure 2.4: Transfer-matrix calculated dispersion along the [100] a) and [001] b) crystal direction for a $100\,\text{nm}$ thick α-MoO$_3$ film in vacuum. In-plane dispersion of the same film for $\omega = 925\,\text{cm}^{-1}$ c) and $\omega = 990\,\text{cm}^{-1}$.

This formalism can be therefore used to investigate the properties of unpatterned layered systems supporting surface wave excitations. An example of the results that can be obtained from the transfer-matrix approach are shown in Figure 2.3 for a semi-infinite SiC

surface. The dispersion of the SPhP is investigated by sweeping the in-plane wavevector at the top layer. The imaginary part of r_{pp} is the quantity of interest, as SPhP require TM polarization for their excitation and it has been shown to reproduce well the dispersion of SPhPs. On the right of the light line the dispersion of the single SPhP interface can be identified by following the maxima of $\text{Im}(r_{pp})$. In Figure 2.3 b), c) we also plot the absolute value of the out-of plane field component E_z for two different in-plane momentum ($k_x = 1000\,\text{cm}^{-1}$ in b) and $k_x = 1500\,\text{cm}^{-1}$ in c) as a function of wavelength and z co-ordinates. It can be seen that the wavenumber of the maximum field follows the dispersion reported in Figure 2.3 a), as highlighted from the red circles.
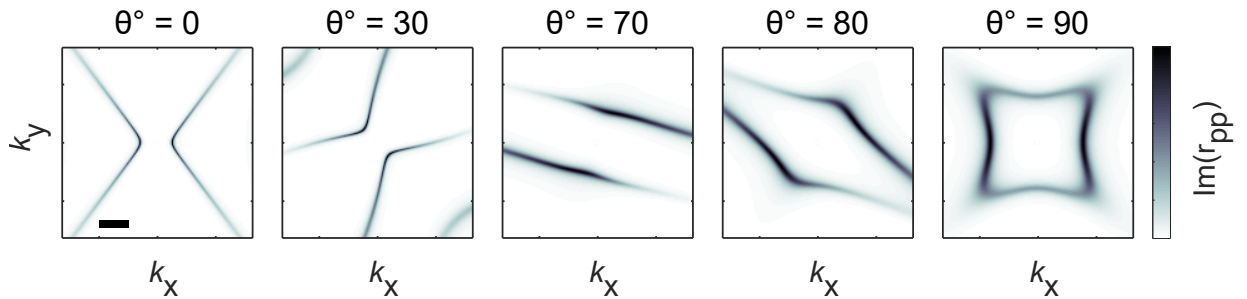
Figure 2.5: Transfer-matrix calculated in-plane dispersion at $925\,\text{cm}^{-1}$ for two stacked $150\,\text{nm}$ thick α-MoO$_3$ films. The in-plane dispersion is shown for various twist angles θ. Scale bar is $10\ k_x/k_0$.

The example of a single SiC surface is not particularly interesting, as analytical solutions exist for this simple geometry. The advantage of the transfer-matrix method is that more complicated geometries can be investigated. For example, for α-MoO$_3$ the dispersion for SPhPs has an analytical expression only in the high-momentum limit due to the additional difficulty of non-isotropic permittivity [52]. The dispersion along both crystalline orientations for α-MoO$_3$ can be easily computed with the matrix-transfer method as shown in Figure 2.4 a,b) for the [100] and [001] crystal directions [46]. The dispersion is for a $100\,\text{nm}$ thick film with vacuum on both sides. The dielectric function of α-MoO$_3$ is modeled with three different Lorentz oscillators along the x, y, z directions with values taken from Ref. [53]. The in-plane part of the dielectric function can be expressed as a function of the rotation angle θ as $\varepsilon_\perp = \varepsilon_x \cos^2\theta + \varepsilon_y \sin^2\theta$ [54]. Then, the momentum angular distribution can be calculated by sweeping the total in-plane momentum and rotation angle at a single frequency. The resulting $\text{Im}(r_{pp}(k_\perp, \theta))$ can be plotted against k_x, k_y as shown in Figure 2.4 c,d) for $925\,\text{cm}^{-1}$ and $980\,\text{cm}^{-1}$. In this way the transition from hyperbolic to elliptical SPhPs due to relative change of sign of the in-plane components of the dielectric tensor at different wavelengths can be clearly visualized. With the transfer-matrix method is also possible to calculate the response of twisted layers of α-MoO$_3$. In Figure 2.5 the in-plane response of a twisted α-MoO$_3$ bilayer in vacuum is shown at $925\,\text{cm}^{-1}$ for various twist angles. Each layer is $150\,\text{nm}$ thick and θ represents the twist angle, analogously to what shown in Figure 1.12. The transition from hyperbolic to canalized SPhPs can be visualized in Figure 2.5, confirming that the transfer-matrix method can accurately reproduce the

SPhP behaviour in complex anisotropic stacks.

2.2 Maxwell equations in arbitrary 3D geometries

In the previous section we have seen how the transfer-matrix method is a powerful tool to investigate surface waves in highly complex stack of layered materials. However, to solve Maxwell's equations in arbitrary three-dimensional geometries fully numerical models have to be employed. Two of the most common methods are finite difference time domain (FDTD) and finite element methods (FEM). In both cases the three dimensional space is discretized by subdivision in finite units of space, the so called mesh of the simulation. Maxwell's equations are solved in each unit of space and the continuity of the fields is ensured at the boundaries of the single cells. FDTD and FEM models differ in the type of algorithms employed to solve Maxwell's equations, with consequences on the type of mesh that can be used to discretize the space. In the following we briefly introduce both methods and summarize the differences between them.

2.2.1 Finite difference time domain method

The working principle the FDTD method to solve Maxwell's equations can be illustrated for simplicity in a one dimensional problem [55]. We consider as an example a lossless transmission line characterized by an inductance L and a conductance C per unit length. The current $I(x,t)$ and voltage $V(x,t)$ across the transmission line is expressed by a system of first order differential equations:

$$\frac{\partial I(x,t)}{\partial x} = -C\frac{\partial V(x,t)}{\partial t}$$
$$\frac{\partial V(x,t)}{\partial x} = -L\frac{\partial I(x,t)}{\partial t} \tag{2.28}$$

By combining the two equations, the voltage can be described by a second order differential equation that has the form of the wave equation [55]:

$$\frac{\partial^2 V(x,t)}{\partial x^2} = LC\frac{\partial^2 V(x,t)}{\partial t^2} \tag{2.29}$$

While eq. 2.29 has analytical solutions in the form of backward and forward traveling waves, we are here interested in finding an approximate numerical solution $f(x,t)$. The first-order space and time derivatives of the function $f(x,t)$ can be approximated via the "finite-difference" method. The Taylor expansion of f at points $x \pm \Delta x/2$ reads:

$$f\left(x \pm \frac{\Delta x}{2}\right) = f(x) \pm \frac{\partial f(x)}{\partial x}\frac{\Delta x}{2} + \frac{\partial^2 f(x)}{\partial x^2}\left(\frac{\Delta x}{2}\right)^2\frac{1}{2!} \pm \frac{\partial^3 f(x)}{\partial x^3}\left(\frac{\Delta x}{2}\right)^3\frac{1}{3!} + \cdots \tag{2.30}$$

By subtracting the expressions for $x + \Delta x/2$ and $x - \Delta x/2$ and normalizing by the small increment Δx one gets:

$$\frac{f\left(x + \Delta x/2\right) - f\left(x - \Delta x/2\right)}{\Delta x} = \frac{\partial f(x)}{\partial x} + \Delta x^2 \frac{\partial^3 f(x)}{\partial x^3}\frac{1}{24}\cdots \tag{2.31}$$

By rearranging the terms, the first order derivative of f can then be written as:

$$\frac{\partial f(x)}{\partial x} \approx \frac{f\left(x + \Delta x/2\right) - f\left(x - \Delta x/2\right)}{\Delta x} + O\left(\Delta x^2\right) \tag{2.32}$$

Which is known as the *central difference* approximation of the first-order derivative. The approximation is said to be second order accurate since the error decays as Δx^2. From eq. 2.31 it can be seen that the amplitude of the error is proportional to $\partial^3 f(x)/\partial x^3$, meaning that quickly varying solutions for which the derivative is large need small values of Δx to produce reliable solutions. In the context of em problems the rate of space-variation of the solutions depends on the wavelength of the problem, meaning that $\Delta x \ll \lambda$ is required. To have second order accuracy it is important that f in eq. 2.31 is evaluated symmetrically around x, so that the even partial derivatives disappear in eq. 2.32.

The central difference approximation can be applied to the derivatives in eq. 2.28, obtaining two equations that are second order accurate in (x, t):

$$\begin{aligned}\frac{I(x + \Delta x/2, t) - I(x - \Delta x/2, t)}{\Delta x} &= -C\frac{V(x, t + \Delta t/2) - V(x, t - \Delta t/2)}{\Delta t}\\\frac{V(x + \Delta x/2, t) - V(x - \Delta x/2, t)}{\Delta x} &= -L\frac{I(x, t + \Delta t/2) - I(x, t - \Delta t/2)}{\Delta t}\end{aligned} \tag{2.33}$$

These equations can be discretized by considering V and I at discrete (x, t) with uniformly spaced intervals $(\Delta x, \Delta t)$. However, to have that eq. 2.33 are consistent, V and I cannot be evaluated in the same point in time and space. This can be solved by separating them in both time and space by $\Delta x/2$ and $\Delta t/2$ with the following staggered time and space-sampling:

$$\begin{aligned}V_i^{n+\frac{1}{2}} &= V\left(i\Delta x, \left(n + \frac{1}{2}\right)\Delta t\right)\\I_{n+\frac{1}{2}}^i &= I\left(\left(i + \frac{1}{2}\right)\Delta x, n\Delta t\right)\end{aligned} \tag{2.34}$$

where i and n are integer numbers. Applying this discrete sampling to eq. 2.28 and considering that the initial values of $V_i^{n-1/2}$ and $I_{i+1/2}^n$ are known at time n for all i, recursive expressions can be written as:

$$\begin{aligned}V_i^{n+\frac{1}{2}} &= V_i^{n-\frac{1}{2}} - \frac{\Delta t}{C\Delta x}\left(I_{i+\frac{1}{2}}^n - I_{i-\frac{1}{2}}^n\right)\\I_{i+\frac{1}{2}}^{n+1} &= I_{i+\frac{1}{2}}^n - \frac{\Delta t}{L\Delta x}\left(V_{i+1}^{n+\frac{1}{2}} - V_i^{n+\frac{1}{2}}\right)\end{aligned} \tag{2.35}$$

This scheme represents and explicit differential operator as V, I can be calculated from their values at the previous time interval and only involve local spatial samples. The solution can be constructed starting from the known initial values $V_i^{n-1/2}$ and $I_{i+1/2}^n$, from which $V_i^{n+\frac{1}{2}}$ can be calculated for all i. After the voltage is updated at time $n + 1/2$, the current can be calculated at time $n + 1$ for all i, and so on in what is referred to as a *leap-frog* strategy.

The recursive recipe outlined in eq. 2.35 is not always stable for any arbitrary choice of the intervals $\Delta x, \Delta t$. For stability in this context it is meant that the energy in the system remains bounded when the energy input into the system is finite [55]. For the one dimensional transmission line it can be shown that the recursive solution for I, V is stable given that $c\Delta t \leq \Delta x$, where c is the propagation speed in the line. This means that the time step must small enough so that the space covered by the waver in the time Δt is smaller than the space interval Δx.
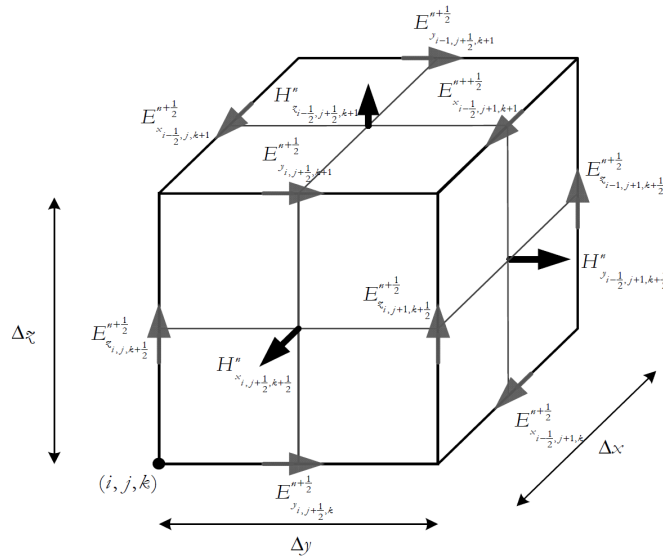
Figure 2.6: Illustration of the electric and magnetic fields in a Yee cell for the implementation of the FDTD method. Adapted from [55].

The application of the central difference approximation to the full three dimensional solution of Maxwell equation was first proposed by Yee in 1966 [55]. The same approach used for the one dimensional transmission line is used in this case: the space is divided in a uniform rectangular grid where each point can be described as $(i\Delta x, j\Delta y, k\Delta z)$ and the time coordinate is uniformly discretized as $t = n\Delta t$ with i, j, k, n integers. Any function evaluated in this 4-dimensional grid can the be expressed as $f_{i,j,k}^n$ from the space-time integer indexes. In this uniform grid, the projections of the electric field on the grid edges are sampled in the edges middle, while the magnetic field is sampled in the middle of the faces, as shown in Figure 2.6. In this way, the fields E and H are staggered in space in the same way it was required for the implementation for the transmission line. The fields

can be determined by considering the third and fourth Maxwell equations, which together constitute six equations from which the six field components can be computed:

$$\frac{\partial \mathbf{B}}{\partial t} = -\nabla \times \mathbf{E} - \mathbf{M}$$
$$\frac{\partial \mathbf{D}}{\partial t} = \nabla \times \mathbf{H} - \mathbf{J} \tag{2.36}$$

The projections of eqs. 2.36 along the x axis are:

$$\mu \frac{\partial H_x}{\partial t} = \frac{\partial E_y}{\partial z} - \frac{\partial E_z}{\partial y} - M_x$$
$$\varepsilon \frac{\partial E_x}{\partial t} = \frac{\partial H_z}{\partial y} - \frac{\partial H_y}{\partial z} - J_x \tag{2.37}$$

and analogous equations can be written for the other axes. The central difference approximation can then be applied to evaluate the partial derivatives in eq. 2.37, assured that the E and H fields are also staggered in time. In the end six recursive equations can be written to fully solve Maxwell equations, where the electric field components are calculated at times $n + 1/2$, from which the magnetic field can be evaluated at time $n + 1$ [55]. Additionally, continuity of the fields has to be enforced at the boundaries of different materials to ensure that the obtained numerical solutions follow Maxwell's equations. Moreover, a criterion must be established to assign a value to ε and μ for faces and edges at the boundaries of different materials. A solution which can be proven to be stable, is to assign at each edge and face at the material boundary the average between the ε and μ of the fours faces or edges adjacent to it [55]. To correctly reproduce the response of objects whose geometry does not conform to a rectangular grid (like a sphere), conformal methods have been developed which give a better approximation compared to the staircase method (only a single material per cell) without the need for increased mesh resolution. The Yee algorithm can also be extended to include non-uniform Cartesian grids and to correctly compute the response of dispersive materials [55].

As for the one dimensional case, it can be shown that the Yee algorithm produces stable solutions given that [55]:

$$\Delta t < \frac{1}{c} \frac{1}{\sqrt{\frac{1}{\Delta x^2} + \frac{1}{\Delta y^2} + \frac{1}{\Delta z^2}}} \tag{2.38}$$

Another difficulty of FDTD simulations is the treatment of the boundaries of the simulation region. While periodic boundary conditions can be implemented in a straightforward way, absorbing boundary conditions so that no em waves are reflected require special treatment. Absorbing boundaries with minimal reflections are achieved with the use of the so called perfectly matched layer (PML) technique, which supports both isotropic and anisotropic materials [55]. PML boundaries are also suited to absorb both propagating components and evanescent parts of em fields.

2.2.2 Finite element method

The finite element method (FEM) is an approach to solve partial differential equations with defined boundary conditions. The FEM can be applied to many relevant problems in physics and engineering and has found applications in structural analysis, heat transfer, fluid flow, mass transport, and electromagnetism [56]. A general boundary-value problem can be defined by a differential equation in a domain Ω:

$$\mathcal{L}\phi = f \tag{2.39}$$

where $\mathcal{L}$ is a differential operator and f the excitation or forcing function. ϕ is the unknown function solving the differential equation with certain boundary conditions at the boundary Γ of the domain Ω. In the solution of three dimensional Maxwell equations the differential operator $\mathcal{L}$ takes the form of the coupled wave equations 2.36 for $\mathbf{E}$ and $\mathbf{H}$. Here the fields are assumed to have harmonic time dependence and the time derivatives are simply computed as $\partial E/\partial t = i\omega E$. The boundary problem outlined by eq. 2.39 can be solved in different ways, of which the more common ones are the Ritz and the Galerkin methods [56]. The Ritz method is based on the variational principle, and we do not discuss it further. In the following we outline the Galerkin method, belonging to the family of weighted residual methods. We consider an approximate solution $\tilde{\phi}$, from which a residual r can be defined as

$$r = \mathcal{L}\tilde{\phi} - f \neq 0 \tag{2.40}$$

The best approximation $\tilde{\phi}$ is the one that minimizes the residual r at all point on the domain Ω. this condition can be written as:

$$R_i = \int_\Omega \omega_i r \; d\Omega = 0 \tag{2.41}$$

where R_i is named the weighted residual integral i and ω_i are chosen weighting functions defined over the whole domain Ω. In Galerkin's method the weighting function ω_i are chosen to be the same as those used to construct the approximate solution:

$$\tilde{\phi} = \sum_{j=1}^{N} c_j \omega_j \tag{2.42}$$

where c_j are constant coefficients to be determined. Eq. 2.41 can be rewritten by using eq. 2.40 as:

$$R_i = \int_\Omega \left(\omega_i \mathcal{L}\{\omega\}^T \{c\} - \omega_i f \right) \; d\Omega = 0 \tag{2.43}$$

This can be rewritten as a matrix equation:

$$[S]\{c\} = \{b\} \tag{2.44}$$

where the matrix elements are

$$S_{ij} = \frac{1}{2} \int_{\Omega} \left(\omega_i \mathcal{L} \omega_j + \omega_j \mathcal{L} \omega_i \right) \, d\Omega \tag{2.45}$$

and

$$b_i = \frac{1}{2} \int_{\Omega} \omega_i f \, d\Omega \tag{2.46}$$

The application of Galerkin's method can be illustrated in a one-dimensional problem [56]. We consider two infinite parallel plates at $x = 0$ and $x = 1$ with potential $\phi = 0$ V and $\phi = 1$ V respectively. The space in between is filled by a medium with constant permittivity ε and a space-varying electric charge $\rho(x) = -(x+1)\varepsilon$ C/m^3. We look here for a solution in the interval $0 \leq x \leq 1$. The solution is found through Poisson equation:

$$\frac{d^2 \phi}{dx^2} = x + 1 \tag{2.47}$$

with the boundary conditions $\phi|_{x=0} = 0$ and $\phi|_{x=1} = 1$. Eq. 2.47 admits the analytical solution $\phi(x) = x^3/6 + x^2/2 + x/3$. Eq. 2.47 can be written in the form of the boundary problem 2.39 with $\mathcal{L} = d^2/dx^2$ and $f = x+1$. The weighted residual equation for Galerkin's method following eq. 2.40 is:

$$\int_0^1 \omega_i \left(\frac{d^2 \tilde{\phi}}{dx^2} - x - 1 \right) \, dx = 0 \tag{2.48}$$

The boundary problem has only two conditions at $x = 0$ and $x = 1$, therefore in 2.48 we have $i = 1, 2$. To proceed with the solution, the functions ω_i (which are also used to construct $\tilde{\phi}$) have to be chosen. A simple choice is to take a polynomial expansion for the approximate solution:

$$\tilde{\phi}(x) = c_1 + c_2 x + c_3 x^2 + c_4 x^3 \tag{2.49}$$

Applying the boundary conditions $\tilde{\phi}|_{x=0} = 0$ and $\tilde{\phi}|_{x=1} = 1$ to 2.49:

$$\tilde{\phi}(x) = x + c_3(x^2 - x) + c_4(x^3 - x) \tag{2.50}$$

Then we take the ω_i functions associated to the coefficients c_3 and c_4 to be determined:

$$\begin{aligned} \omega_1 &= x^2 - x \\ \omega_2 &= x^3 - x \end{aligned} \tag{2.51}$$

Now the approximate solution $\tilde{\phi}(x)$ and the two functions ω_1 and ω_2 can be substituted in 2.48. From the evaluation of the definite integral, two algebraic equations are obtained:

$$\frac{c_3}{3} + \frac{c_4}{2} - \frac{1}{4} = 0$$
$$\frac{c_3}{2} + \frac{4c_4}{5} - \frac{23}{60} = 0$$

(2.52)

from which the coefficients $c_3 = 1/2$ and $c_4 = 1/6$ can be determined. In this case the exact analytical solution is recovered. It can be shown that this happens as long as the trial functions constitute a complete basis for the problem [56].

The success of Galerkin's method to solve the boundary problem in 2.47 relies on finding an appropriate set of trial functions defined over the entire domain that can approximate the true solution. While in this one dimensional case the trial functions were simple polynomials, for three dimensional problems where the real solution can be a rapidly varying function, it is very difficult to find an appropriate set of trial functions. The aim of the FEM is to subdivide the whole domain in smaller subdomains where Galerkin's method can be applied. If the single domains are small enough, simple trial functions can be used for each subdomain. The solutions found in each subdomain are then interpolated with a choice of interpolation function, usually linear or a low order polynomial. The FEM with Galerkin's recipe can be summarized of being comprised by the following steps [56]:

1. The whole domain is divided in smaller subdomains.

2. An appropriate interpolation function is chosen to relate the solutions found in each subdomain.

3. A system of algebraic equations is found by applying Galerkin method.

4. A solution for the system of equations is found.

2.2.3   FDTD and FEM comparison

In the previous sections we introduced the fundamental elements of the FDTD and FEM numerical methods to solve Maxwell's equations in three dimensions. We briefly review here the differences between the two methods, their advantages and shortcoming depending the problem at hand.

A first difference is in the discretization of the three dimensional space. While the FDTD method only allows non-uniform orthogonal gridding, there is no inherent limitation for the way in which the domain is subdivided in FEM simulations. This means that curved structures are generally better meshed in FEM than in FDTD. In FEM, the subdomains usually are of triangular shape in two dimensions and are tetrahedrons in three dimensional problems, which are well-suited to approximate arbitrarily complex shapes. As a result, the number of mesh cells to simulate complex structures is usually lower for FEM than for FDTD, reducing the simulation time [57]. An example of the different meshing in FEM and FDTD simulations is shown for a three dimensional disk in Figure 2.7. The same volume
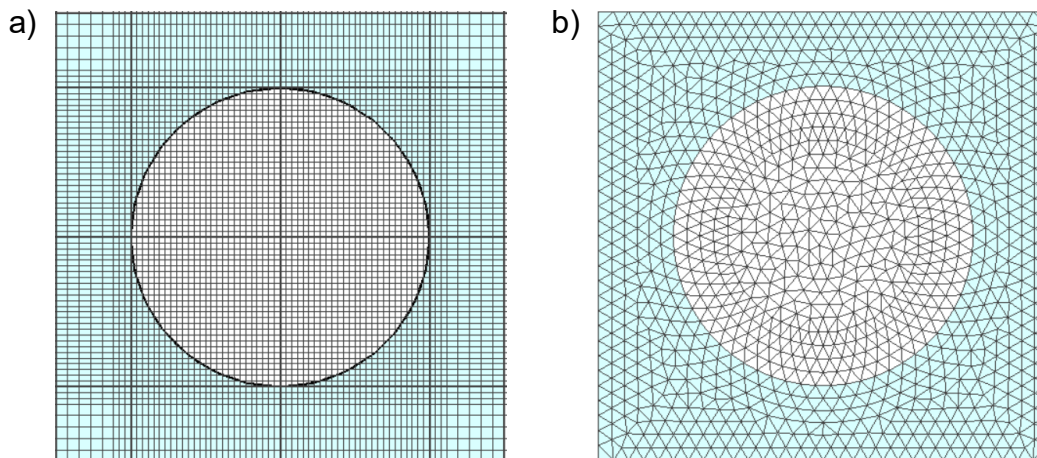
Figure 2.7: Example of meshing of a disk (top view) in a FDTD a) and a FEM b) simulation. The FDTD model requires more than 4 times more mesh cells.

is meshed with more than 4 times the cells in the FDTD ($\sim$ 115000 mesh cells) simulation compared to the FEM case ($\sim$ 25000 mesh cells), while the circular geometry is better represented in the FEM model thanks to the non Cartesian mesh. Another important difference between the two methods is that FDTD is a time-domain method, while the FEM is a frequency-domain method. In a FDTD simulation a defined source excites the system, and the time evolution is simulated step by step. This means that the transient response of a system can be investigated, and broadband simulations are naturally included in a single run. The frequency response in FDTD models is obtained by Fourier Transform of the time signal. Conversely in FEM methods the time dependence is assumed to be harmonic, so the transient response cannot be investigated. The simulations are inherently single-wavelength, and the broadband response is obtained by combining many different single-wavelength simulations. At the same time, FDTD struggles in simulating very high quality factor systems, as to obtain correct results one needs to extend the simulation in time until the fields are completely dissipated. To simulate dispersive materials in FDTD the material response has to be fitted with an analytical model, while this is not necessary in the FEM case [57]. In the rest of this work we use both FEM and FDTD simulations to investigate various nanophotonic structures. For FDTD simulations the software Lumerical is used, while for FEM simulations CST Studio is employed.

Chapter 3

Experimental Methods

In this chapter we introduce the main experimental techniques employed in this work. We outline the general principles underlying each method. We first introduce the most common technique used to investigate the optical response in the mid-infrared, fourier transform infrared (FTIR) spectroscopy. We then discuss scattering-scanning near field-microscopy (sSNOM), which is the main experimental technique employed in this thesis. sSNOM allows imaging and spectroscopy in the near-field, overcoming the diffraction limit and achieving deeply subwavelength resolution.

3.1   Fourier Transform Infrared Spectroscopy

In the visible range, spectra are usually acquired by using gratings. Broadband light incident on a dispersive grating is diffracted at different angles, and the signal is then collected on a camera. The position of the signal on the camera is then related to the wavelength of the incoming light. However, cameras work on limited spectral ranges, and are not routinely available in the mid-infrared. Instead, in FTIR spectroscopy an interferometer is used to collect interferograms, from which spectra are obtained through fourier transform (FT). An interferogram is obtained by varying the optical path difference between the two arms of a common-path interferometer. This is achieved in the most simple configuration employing a Michelson interferometer, where a light source is divided by a beam splitter in two orthogonal arms. One of the two arms consists of a movable mirror as shown in the sketch of Figure 3.1. By moving the mirror, a different optical path is acquired in the two arms, resulting in a variable interference at the beam splitter where the two beams are recombined. To obtain an interferogram one has to collect the interference generated by all the possible path length differences. The intensity $I(x)$ function of the path difference x, is recorded by a single pixel detector.

The relationship between a spectrum and its interferogram can be understood by considering the FT of a plane wave with harmonic time dependence [23]:

$$\mathbf{E}(\mathbf{r}, t) = \frac{1}{2\pi} \int_{-\infty}^{+\infty} B(\omega)^{\frac{1}{2}} e^{i(\omega t - \mathbf{q} \cdot \mathbf{r})} \, d\omega \tag{3.1}$$

$B(\omega)$ is the spectrum of the em field that we want to retrieve. The average intensity at the beam splitter after the two beams are reflected back from the mirrors is:

$$I(\mathbf{r}, \tau) = \frac{c}{8\pi T} \int_{-T/2}^{T/2} \left| \frac{\mathbf{E}(\mathbf{r}, t + \tau)}{2} + \frac{\mathbf{E}(\mathbf{r}, t)}{2} \right|^2 dt \tag{3.2}$$

where τ is the time delay accumulated due to the different path lengths and T is the period of the em field. Replacing eq. 3.1 into eq. 3.2 we get:

$$I(\tau) = \frac{I_0}{2} + \frac{c}{16\pi^2 T} \int_{-\infty}^{+\infty} B(\omega) \cos(\omega\tau) \, d\omega \tag{3.3}$$

where

$$I_0 = \frac{c}{8\pi T} \int_{-T/2}^{T/2} \mathbf{E}(\mathbf{r}, t) \cdot \mathbf{E}^*(\mathbf{r}, t) \, dt \tag{3.4}$$

From eq. 3.3 we can rearrange the terms to get:

$$\left(I(\tau) - \frac{I_0}{2} \right) \frac{16\pi^2 T}{c} = \int_{-\infty}^{+\infty} B(\omega) \cos(\omega\tau) \, d\omega = 2\pi \text{Re}(\tilde{B}(\omega)) \tag{3.5}$$

The right hand side can be regarded as the real part of the FT of the spectrum $\tilde{B}(\omega)$, as we are assuming $B(\omega)$ to be a real-valued function. The connection between the spectrum and the interferogram is then:

$$B(\omega) = \frac{32\pi T}{c} \int_{-\infty}^{+\infty} \left(I(\tau) - \frac{I_0}{2} \right) e^{-i\omega\tau} \, d\tau \tag{3.6}$$

which shows that the spectrum is proportional to the FFT of the interferogram after subtraction of the baseline value $I_0/2$ arising from incoherent sum of the two beams. In a symmetric interferometer the interferogram is an even function around the zero path difference point, so that the FT is a real-valued function. In a realistic implementation, the time delay between the beams cannot be extended to $\pm\infty$ since the displacement of the moving mirror is finite. As a consequence the integral in eq. 3.6 is cut-off at a certain value $\tau_0 = 2L/c$ representing the maximum time delay achievable with a mirror travelling a distance L:

$$B(\omega) = \frac{32\pi T}{c} \int_{-\tau_0}^{+\tau_0} \left(I(\tau) - \frac{I_0}{2} \right) e^{-i\omega\tau} \, d\tau \tag{3.7}$$

We can see how the truncation of the integral influences the measured spectrum shape. Defining

$$C(\tau) = \frac{32\pi T}{c} \left(I(\tau) - \frac{I_0}{2} \right) \tag{3.8}$$
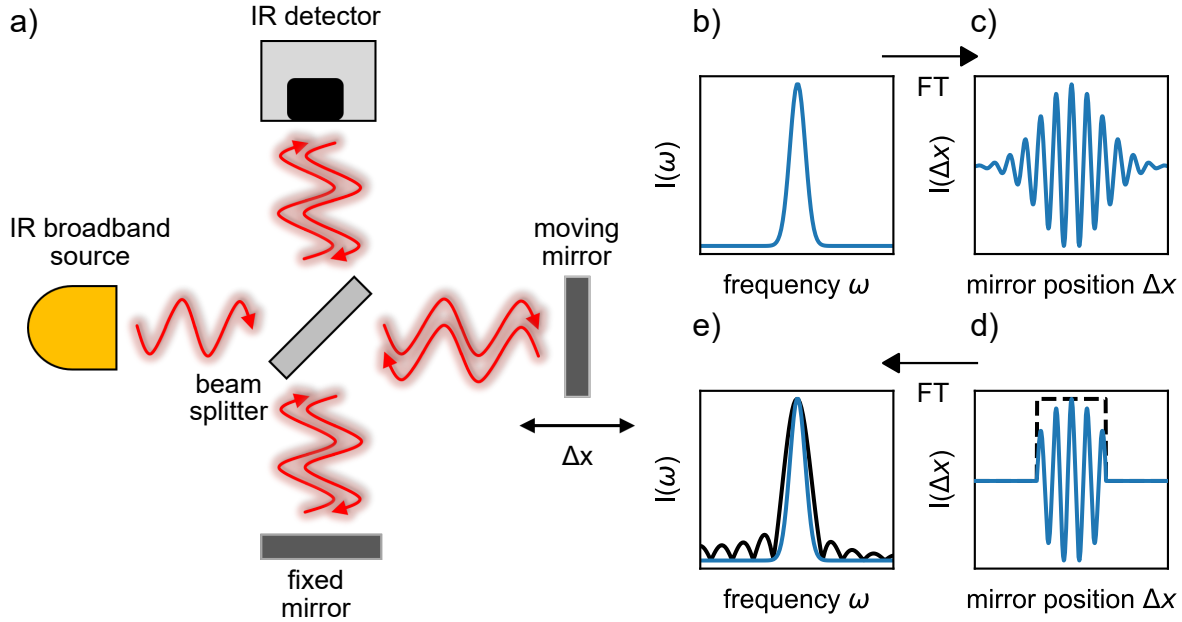
eq. 3.6 can be rewritten as

Figure 3.1: a) Sketch of a Michelson interferometer, used in FTIR spectroscopy to collect interferograms. Effect of the finite travelling distance Δx of the moving mirror on a trial gaussian spectrum b). The interferogram of b) obtained by FT is the shown in c). A finite Δx can be simulated by multiplying the interferogram by a box function, shown with a dashed black line in d). e) FT of the truncated interferogram broadens the retrieved spectrum (black line) and introduces ripples due to the FT spectrum of the box function. Side ripples can be eliminated through apodization with a function having a smooth FT spectrum.

$$B(\omega) = \int_{-\infty}^{+\infty} C(\tau)e^{-i\omega\tau} \, d\tau \tag{3.9}$$

Supposing the spectrum to be a delta function $B(\omega) = B_0\delta(\omega - \omega_0)$, we get from the integral in the above eq. 3.9 that $C(\tau) = C_0e^{i\omega_0\tau}$, where $C_0 = B_0/2\pi$. Computing the spectrum from the truncated integral in eq. 3.7 and using $C(\tau)$ found above, we get

$$B(\omega) = C_0 \int_{-\tau_0}^{+\tau_0} e^{-i(\omega-\omega_0)\tau} d\tau = 2C_0\frac{\sin\left[(\omega - \omega_0)\tau_0\right]}{(\omega - \omega_0)\tau_0} \tag{3.10}$$

The finite displacement of the mirror broadens the spectrum from an infinitely narrow peak to a broader one with width $\Delta\nu \approx 1/2L$, where ν is the frequency $\omega = 2\pi\nu = 2\pi c/\lambda$. The absolute resolution $\Delta\nu$ is often expressed in wavenumbers, given by $1/2L$ with L measured in cm. For example, a distance $L = 0.25$ cm corresponds to a spectral resolution of $2\,\text{cm}^{-1}$. This effect is illustrated in Figure 3.1 b-d), where a source with gaussian spectrum is considered as shown in b). Its FT is shown in c), representing the interferogram.

The effect of a limited Δx is simulated by multiplication with a box function (dashed black line) shown in c). Inverse FT of the truncated interferogram results in the black line in e), showing a wider peak compared with the initial spectrum shown for reference in blue. The ripples are due to the abrupt truncation of the interferogram, and come from the FT of the box function. The resulting spectrum is the convolution between the FT of the initial spectrum and the one of the box function. This effect can be minimized by multipication with a function slowly going to zero with a smoother FT spectrum, in what is called "apodization".
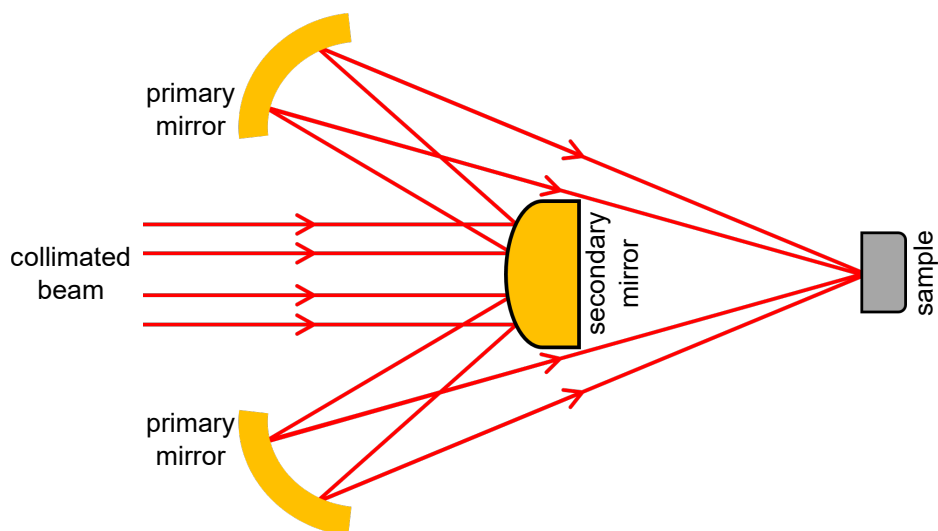
Figure 3.2: Two dimensional sketch of the cross section of a Cassegrain reflective objective often employed in FTIR microscopes.

In an actual FTIR experimental setup illumination is obtained using blackbody radiation, providing a broadband source where the peak wavelength can be tuned through the source temperature. The most common detectors employed in mid-IR spectroscopy are mercury cadmium telluride (MCT) detectors, which need to be cooled with liquid nitrogen down to $77\,\text{K}$ to suppress thermal noise. FTIR spectrometer can be coupled to a microscope to investigate small sample regions, as in the case of arrays of optical antennas resonating in the mid and near-IR. To achieve broadband operation, conventional refractive objectives are avoided due to chromatic aberrations related to refractive index dispersion. Moreover, almost all materials have absorption bands somewhere in the mid-IR. As a consequence Cassegrain reflective metallic objectives are usually employed. A drawbacks of Cassegrain objectives is that they produce an illumination of the sample that has an angular spread with a nonzero average, as shown in the sketch of Figure 3.2. This can be problematic in the measurement of samples with strong angular dispersion.

3.2   Scattering-scanning near-field optical microscopy

The FTIR technique presented in the previous section is a far-field technique, and as such is diffraction-limited. Mid-infrared spectroscopy is a powerful technique as each material has its own specific vibrational fingerprint. However the spatial resolution is rather poor, limited to several microns in size as $\lambda \approx 3 - 10 \mu m$. Higher resolution beyond the diffraction limit is then needed for investigation of highly inhomogeneous samples.

In section 1.3 of the introduction we have seen that the diffraction limit can be cast in the form of Heisenberg uncertainty principle, and that the resolution limit is a consequence of all the components of the wavevector k_i being real and smaller than k_0. Close to a material boundary, evanescent components of the em field with complex wavevectors exist in the so called *near-field* region. The electric field from the surface along the perpendicular direction z will have the form [1, 30]:

$$\mathbf{E}(k_z, k_y, z) = e^{ik_z z}\mathbf{E}(k_z, k_y, 0) \tag{3.11}$$

with $k_z = \sqrt{k^2 - k_x^2 - k_y^2}$. Then one can clearly distinguish components that will propagate through the far field from evanescent components depending on the value of the in-plane momentum $k_\parallel = k_x^2 + k_y^2$:

$$\begin{aligned} k^2 > k_\parallel^2 &\to k_z \text{ is real and these components propagate} \\ k^2 < k_\parallel^2 &\to k_z \text{ is imaginary and these components do not propagate} \end{aligned} \tag{3.12}$$

Free-space propagation of em waves acts as a low-pass filter for high in-plane wavevectors, corresponding to components with rapid spatial variations. To overcome the diffraction limit the high $k_\parallel$ need to be measured, which corresponds to measuring the near-field response of the system. With this formulation the connection between near-field optics and overcoming the diffraction limit is highlighted. The question is then how to collect the near-field response of a system.

At low frequencies where the wavelength has macroscopic dimensions on the order of millimeters the problem of measuring the near-field response is easily solved. For RF antennas it is actually more practical to measure the near-field response of an antenna and then infer the far-field radiation pattern with near to far-field transformations [58]. At RF frequencies the near-field can be directly measured through an electrical probe, which can be scanned in a surface around the antenna to reconstruct the near-field pattern. At optical frequencies the wavelength of em waves is at least two orders of magnitude smaller, meaning that an appropriate probe would have to be precisely positioned very close to the surface, which brings an additional technological challenge. More importantly, direct measurement of the time-varying electric field at optical frequencies is not feasible because electronic components stop working in the hundreds of GHz range. Therefore a near-field probe operating at optical frequencies has to work by somehow carrying the high $k_\parallel$ components to the far-field where it can be measured by a detector.

We can understand how a near-field probe allows propagation of high $k_\parallel$ components to the far-field in general terms [1]. We consider the near-field source to be positioned at coordinate $-z_0$, while the sample lies in the $z = 0$ plane. We assume the effect of the sample interaction to be represented by an operator acting only on the in-plane components $T(x, y)$. We consider a configuration where the signal from the source at $z = -z0$ is transmitted through the sample and propagates to the detector at $z = z_\infty$. Right after sample interaction the field is [1]:

$$\mathbf{E}_{sample}(x, y, z = 0) = T(x, y)\mathbf{E}_{source}(x, y, 0) = T(x, y)\mathbf{E}_{source}(x, y, -z_0)e^{ik_{z1}z0} \qquad (3.13)$$

where k_{z1} is the wavevector of the wave propagating from the source to the sample. The Fourier spectrum $\hat{\mathbf{E}}_{sample}$ of the field in eq. 3.13 can be written as:

$$\hat{\mathbf{E}}_{sample}(\boldsymbol{\kappa}_\parallel, 0) = \int_{-\infty}^{-\infty} \hat{T}(\boldsymbol{\kappa}_\parallel - \mathbf{k}_\parallel)\hat{\mathbf{E}}_{source}(\mathbf{k}_\parallel, -z_0)e^{ik_{z1}z0} \, dk_\parallel \qquad (3.14)$$

where $\mathbf{k}_\parallel = (k_x, k_y)$, $\hat{\mathbf{E}}_{source}$ is the fourier spectrum of the source field and $\hat{T}(\boldsymbol{\kappa}_\parallel - \mathbf{k}_\parallel)$ the fourier transform of $T(x, y)$. The field at the detector is the propagation of the field in 3.14 to z_∞:

$$\mathbf{E}_{detector}(x, y, z_\infty) = \int_{-\infty}^{-\infty} \hat{\mathbf{E}}_{sample}(\boldsymbol{\kappa}_\parallel, 0)e^{i(\kappa_x x + \kappa_y y)}e^{i\kappa_z z_\infty} \, d\boldsymbol{\kappa}_\parallel \qquad (3.15)$$

Only low-in plane wavevectors will be propagated to the detector as $\kappa_z = \sqrt{\kappa_0^2 - \boldsymbol{\kappa}_\parallel^2}$ and the same conditions formulated in 3.12 apply, meaning that we can probe only components for which $\boldsymbol{\kappa}_\parallel^2 \leq \kappa_0^2$. To understand how high-in plane components enter into the propagating spectrum of eq. 3.15 we can rewrite the fourier spectrum of the source as [1]:

$$\hat{\mathbf{E}}_{source}(\mathbf{k}_\parallel, 0) = \int_{-\infty}^{-\infty} \hat{\mathbf{E}}_{source}(\tilde{\mathbf{k}}_\parallel, 0)\delta(\tilde{\mathbf{k}}_\parallel - \mathbf{k}_\parallel)d\tilde{\mathbf{k}}_\parallel \qquad (3.16)$$

If the source field consists of a single spatial frequency $\hat{\mathbf{E}}_{source} \propto \delta(\mathbf{k}_\parallel - \tilde{\mathbf{k}}_\parallel)$, by substitution in eq. 3.14 and computing the integral with the delta function, one gets $\boldsymbol{\kappa}_\parallel - \mathbf{k}_\parallel = \tilde{\mathbf{k}}_\parallel$. Rearranging the previous equation:

$$\boldsymbol{\kappa}_\parallel = \mathbf{k}_\parallel + \tilde{\mathbf{k}}_\parallel \qquad (3.17)$$

This indicates that the effect of the in-plane wavevector of the source $\tilde{\mathbf{k}}_\parallel$ is to shift by the same amount the wavevector at the sample $\mathbf{k}_\parallel$. As the far-field low pass filter is applied on $\boldsymbol{\kappa}_\parallel$, depending on the magnitude of $\tilde{\mathbf{k}}_\parallel$ different components of the spectrum $\hat{T}$ will be carried to the far-field. Therefore, large spatial frequencies of the sample are combined with large spatial frequencies of the probe field, such that the difference wavevector corresponds to a propagating wave in the angular spectrum that travels towards the detector. The higher the k-vector from the source, the higher in-plane components will be

propagated in the far-field. If the source consists of focused free-space light, the maximum in-plane component is $\tilde{\mathbf{k}}_{\parallel,max} = 2\pi NA/\lambda$ where NA is the numerical aperture of the focusing objective and λ the operation frequency. To shift higher in-plane components into the far-field spectrum, a near-field source with evanescent components with high in-plane wavevector has to be used. The in-plane wavevector provided by a near-field source of dimension L can be estimated as:

$$\tilde{\mathbf{k}}_{\parallel,max} \approx \frac{\pi}{L} \tag{3.18}$$

In summary, to achieve imaging below the diffraction limit the source should be places in the near-field so that evanescent components of the field interact with the sample. Moreover, the smaller the near-field probe, the higher the in-plane components that will reach the detector, improving consequently the spatial resolution.

3.2.1 Measuring the near-field at optical frequencies

Two prominent ways to probe the near-field at optical frequencies have been developed in the last 20-30 years, both based on modifications of an atomic force microscope (AFM) [59]. One method is based on collection or emission of light through an optical fiber called aperture scanning near-field optical miscroscope (aSNOM), while the other is based on collecting the scattering from an AFM tip on which light is tightly focused, named scattering scanning near-field optical miscroscope (sSNOM). In both techniques the probe is brought in close proximity of the surface to be investigated so that it is located in the near-field region, typically with a distance smaller than a wavelength of the operating em radiation. Control of the tip-sample distance is achieved by employing feedback-based methods developed for AFM. A sketch of the two methods is shown in Figure 3.3. As both aSNOM and sSNOM are based on an AFM setup, topographical information is typically available during collection of the optical signal.

Both aSNOM and sSNOM are able to probe the near-field response of a sample, and each technique has its own strengths and weaknesses. We briefly compare both techniques in the following. In aSNOM many different configurations are possible, where the optical fiber can be used as the illumination source or for light collection. The optical fiber is tapered towards the aperture, and is usually coated with a metallic layer to reduce leakage radiation in the taper. As discussed in the previous section, the resolution that can be achieved depends on the size of the near-field source, which in this case is represented by the aperture size and should therefore be subwavelength. During the tapering, the size of the waveguide is continually decreasing, up to a point where the propagation constant of all the waveguide modes become imaginary. Moreover, light passing through a subwavelength hole of radius r in a perfectly conducting film goes down as $I \propto (r/\lambda)^4$ [60]. A more accurate prediction of the power going through a tapered waveguide is reported in ref. [1]. Only a tiny fraction of light passes through the aperture, limiting in practice the minimum aperture size and the spatial resolution that can be achieved in the visible to somewhere in between $50\,\text{nm}$ and $100\,\text{nm}$ [1]. The advantage of this arrangement is the absence of
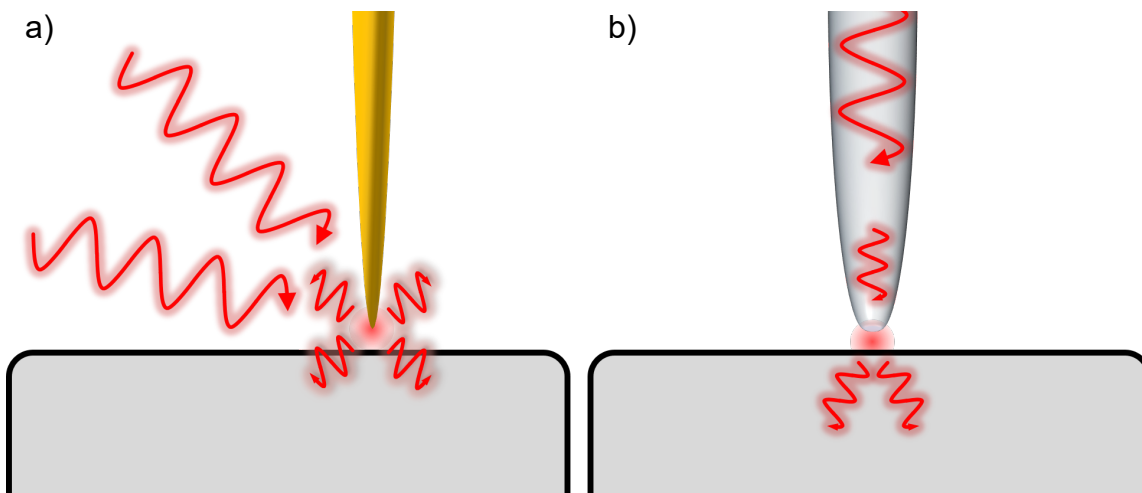
Figure 3.3: Sketch of a sSNOM a) and of an aSNOM setup b). In sSNOM light is focused at the end of an AFM tip, and the backscattered light is collected. In aSNOM light passes through a waveguide with a subwavelength aperture at the end, and transmitted light is collected by an objective below the sample.

far-field background, as the illumination only comes through the evanescent field of the subwavelength aperture.

On the other hand, sSNOM does not suffer from low signal intensity, as the near-field source is produced by direct coupling from focused free-space light. The resolution depends exclusively on the radius of curvature of the tip. This indicates that sSNOM has the possibility of outperforming aSNOM at longer wavelengths, since the bottleneck for aSNOM is the transmission through the tapered fiber, which is wavelength-independent. The main problem in sSNOM is distinguishing the tiny fraction of light that gets backscattered by the tip from light that goes back to the detector without having interacted with the near-field. To enhance the near-field signal metallic tips can be used, which can produce strong field enhancement at the tip apex when the polarization is along the tip shaft through the rod-lighting effect [30,61]. However, the field-enhancement is not enough alone to produce a sufficiently strong signal, as a diffraction-limited spot for $\lambda = 10\,\mu m$ is approximately 10^6 times larger than the near-field area below a tip with a curvature radius of $10\,nm$. We will discuss in more details how background-suppression is achieved in sSNOM, allowing mapping at a resolution higher than $\lambda/100$ at mid-infrared frequencies [1].

sSNOM is therefore generally preferred at mid and far infrared frequencies as it reaches much higher resolution compared to aSNOM. Moreover, fiber technology in the mid-IR is not as nearly as developed as in the visible range [62], making aSNOM impractical at these wavelengths. On the other side, at visible wavelengths the resolution achieved by sSNOM and aSNOM is similar, and aSNOM benefits from a simpler overall experimental arrangement.

3.2.2 Modeling of tip-sample interaction in sSNOM

To understand how suppression of far-field scattered light is achieved in sSNOM it is useful to start with a model for the tip-sample interaction. The first issue of modeling a sSNOM system is how to account for the presence of the tip without resorting to fully three dimensional em simulations. The point dipole model (PDM) is the simplest analytical approximations for the sample-tip interaction [63]. The sample is considered here to be a semi-infinite flat surface with dielectric function ε_s. The tip is treated as a spherical particle in the electrostatic approximation, where the polarizability has a simple analytical expression [63]:

$$\alpha = 4\pi a^3 \frac{\varepsilon_p - \varepsilon_m}{\varepsilon_p + 2\varepsilon_m} \tag{3.19}$$

where the sphere radius a is chosen to be the curvature radius of the tip. ε_p is the dielectric function of the probe and ε_m is the dielectric function of the embedding medium in which the tip is placed (in standard conditions $\varepsilon_m = 1$). A sketch of the PDM is shown in Figure 3.4 a). If the incident electric field E_{in} is polarized perpendicularly to the sample surface, it can be shown that the dipole induced in the sphere $p = \alpha E_i$ produces an image dipole in the sample $p' = p\beta$ [63], where:

$$\beta = \frac{\varepsilon_s - 1}{\varepsilon_s + 1} \tag{3.20}$$

The effective polarizability of the two near-field coupled dipoles in the electrostatic approximation is [64, 65]:

$$\alpha_{eff} = \frac{\alpha}{1 - \frac{\alpha\beta}{16\pi(a+z)^3}} \tag{3.21}$$

where z is the distance between the tip and the sample surface. The scattering intensity measured at the detector is proportional to the square of the effective polarizability $S \propto |\alpha_{eff}|^2$. A better description can be obtained by considering that the tip is not only illuminated by the directly incident light, but also by a component that is first reflected by the sample $E_{tip} = (1 + r)E_{in}$, where r is the appropriate Fresnel reflection coefficient. Moreover the scattered light also gets reflected by the substrate. Therefore the signal is proportional to $S \propto |(1 + r)^2\alpha_{eff}|^2$ [64]. The PDM model has been extended to take into account the elongated shape of the tip to provide better quantitative agreement with experimental data [64], and has been modified to additionally account for layered samples [65].

The scattered signal from the tip-sample interaction is only a small portion of the scattered light reaching the detector, due to the presence of far-field background. Since light intensity is measured at the detector, we can write:

$$I = |E_{nf} + E_{bg}|^2 = |E_{nf}|^2 + |E_{bg}|^2 + E_{nf}E_{bg}^* + E_{nf}^*E_{bg} \tag{3.22}$$
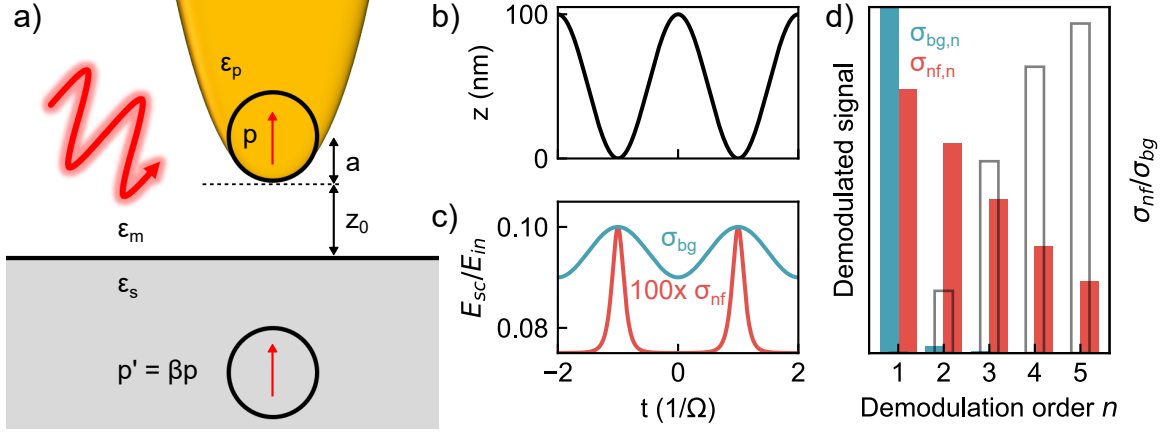
Figure 3.4: a) Sketch of the PDM, where the tip is modeled by a sphere of radius a at a distance z_0 above the sample surface. An image dipole p' is induced in the sample, which depends on the dielectric function ε_s of the sample through the parameter β. The tip oscillates above the sample following the trace in b). The PDM is used to calculate the scattered field from the tip (red curve) through eq. 3.21 and the $z(t)$ shown in b). The background field depends linearly on z, and the tip scattered far-field contribution is shown by the blue curve. d) Demodulation of the periodic signal at higher orders $n\Omega$ diminishes the far-field background (blue bars) much quicker than the near-field (red bars). The ratio between the near and far-field contributions increases with the demodulation order (gray bars).

where $E_{nf} = \alpha_{eff}E_{in}$ and $E_{bg} \gg E_{nf}$ is the far-field background. Scattering coefficients are usually defined as $E_{inc} = \sigma_{nf}E_{nf}$ and $E_{inc} = \sigma_{bg}E_{bg}$. To suppress far-field background in sSNOM, the AFM is operated in tapping mode at a frequency Ω on the order of hundreds of kHz. As the effective polarizability in eq. 3.21 depends on z, the scattered light will also be modulated at the same frequency. The height modulation of the tip is $z(t) = z_0 + A(1 + \cos(\Omega t))$, where A is the tapping amplitude and z_0 the minimum tip-sample distance as shown in Figure 3.4 b). Plugging $z(t)$ in eq. 3.21, $\alpha_{eff}(t)$ and the scattering coefficient σ_{nf} can be calculated. While α_{eff} depends in a nonlinear way on z, the far-field background radiation is approximately linearly decreasing $\sigma_{bg} = -z(t)/\lambda + 1$ when $z \ll \lambda$ [66]. In Figure 3.4 c) the scattering coefficients σ_{nf} and σ_{bg} are shown for a $a = 15\,\text{nm}$ gold tip on top of a gold surface $\varepsilon_s = \varepsilon_p = -5000 + i1000$ at $\lambda = 10\,\mu\text{m}$. The tapping amplitude (TA) is set at $A = 50\,\text{nm}$ and it assumed that the background field is $1/10$ of the incident field with the near-field signal being $1/100$ of the background signal. As a consequence of the nonlinearity of $\alpha_{eff}(z)$, $\sigma_{nf}(t)$ is anharmonic, while $\sigma_{bg}(t)$ has the same shape of $z(t)$. This difference allows the separation of the near-field signal from the background. The scattering coefficients can be expressed as a Fourier series:

$$\sigma = \sigma_{nf} + \sigma_{bg} = \sum_{n=-\infty}^{\infty} (\sigma_{nf,n} + \sigma_{bg,n})e^{in\Omega t} \tag{3.23}$$
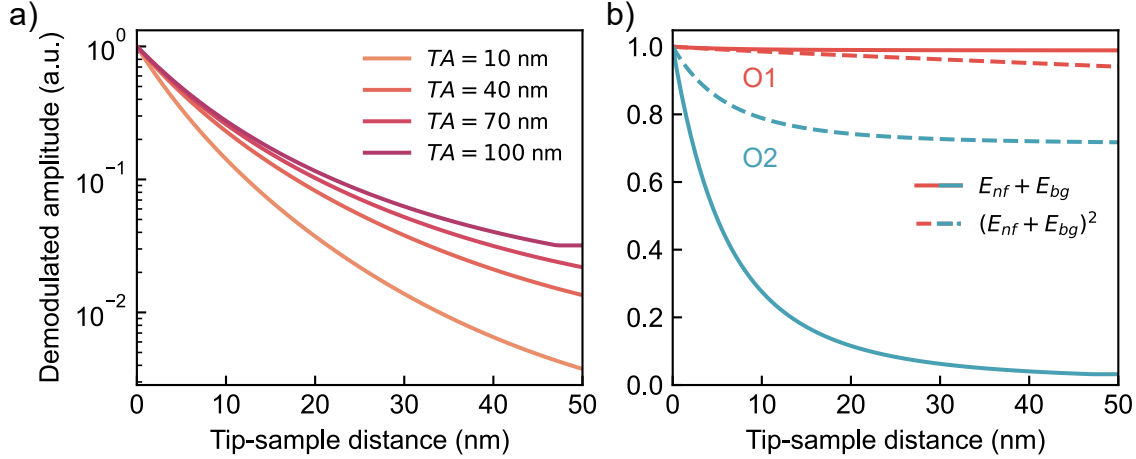
Figure 3.5: a) Approach curve for the signal demodulated at 2Ω for different values of the tapping amplitude. b) Demodulation at higher orders provides good background suppression when considering the sum of the near and far-field scattered fields (solid lines). However the intensity is measured at the detector, which introduces a multiplicative background that is not suppressed by the demodulation process (dashed curves). Approach curves are shown with demodulation Ω (red curves) and 2Ω (blue curves).

The terms σ_n correspond to demodulation of the signal at $n\Omega$. The Fourier coefficients σ_n are obtained by FT of the time-periodic signals and by selecting the value of the FT at the frequency $n\Omega$. The Fourier coefficients for the periodic signals shown in Figure 3.4 c) are reported in Figure 3.4 d). The contribution of the background quickly diminishes for $n > 1$, allowing the reconstruction of the near-field signal by choosing a demodulation order $n \geq 2$. The ratio between the near-field and the background signals is also shown in Figure 3.4 d). The higher the demodulation order n the less far-field background, at the price of overall signal and consequently lower signal to noise ratio (SNR) in a real experiment [67]. A similar argument can be made for the TA, with higher TA yielding better SNR and lower TA giving better suppression of far-field radiation. In Figure 3.5 a) the signal amplitude demodulated at 2Ω is shown as a function of the tip-sample distance z_0 (the so called approach curve) for different TA values. The curves in Figure 3.5 a) are normalized to highlight the faster decay of the signal for lower TA, indicating better far-field background suppression.

Demodulation to higher orders n is however not sufficient for complete far-field suppression since in the signal intensity the product between near-field and background terms appears as shown in eq. 3.22. If we consider the contribution from background scattering coefficients $\sigma_{bg,n}$ to be negligible for $n \geq 1$, the demodulated intensity I_n at order n:

$$I_n \propto |E_{nf,n}|^2 + E_{nf,n}E_{bg,0}^* + E_{nf,n}^*E_{bg,0} \tag{3.24}$$

which shows that demodulation at higher orders is not sufficient for complete far-field background suppression due to the multiplicative term $E_{bg,0}$. The effect of the multiplicat-

ive background is shown in Figure 3.5 b) by plotting the approach curves for $n = 1, 2$ when the total field is given by the sum of the near-field and background fields (solid lines) or by the square of the sum (dashed lines).When summing the fields the multiplicative background is not present, allowing background free-signal already for $n = 2$. When instead considering the intensity, at $n = 2$ considerable background is present. We will see in the next sections how $E_{bg,0}$ can be removed by performing interferometric measurements.

3.2.3   Pseudo-Heterodyne detection for narrowband near-field imaging
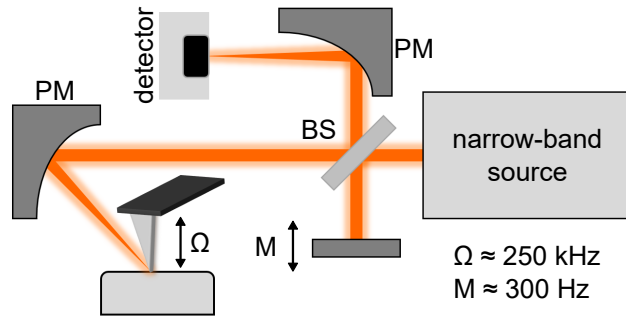

Figure 3.6: a) Sketch of the PsHet setup, a narrow-band source is coupled into an asymmetric Michelson interferometer. A beam splitter (BS) sends half the light to a parabolic mirror (PM) which focuses the beam on the tip oscillating at frequency Ω. The other half of the beam is sent to the reference arm where a mirror vibrates at frequency $M \ll \Omega$. Light is then focused on a detector by a PM.

As we have seen in the previous section, even by applying high-order demodulation of the signal a multiplicative background is still present in the sSNOM signal. For a single-wavelength source the multiplicative background contribution can be eliminated by applying the so called pseudo-heterodyne (PsHet) interferometric technique [66]. On top of removing the multiplicative background, implementation of the PsHet method allows the reconstruction of the amplitude and phase of the signal. The PsHet method consists in adding a Michelson interferometers to the sSNOM setup as sketched in Figure 3.6. The light source is split by a beam splitter, half of the signal is focused on the tip by a parabolic mirror and half is sent to a reference arm. As discussed for FTIR, in sSNOM light is focused through metallic parabolic mirrors to allow operation over a wide range of frequencies. The backscattered light from the tip recombines with the reference signal and is sent to the detector. The light intensity reaching the detector is:

$$I \propto |E_{nf} + E_{bg} + E_{ref}|^2 = (E_{nf} + E_{bg} + E_{ref})(E_{nf} + E_{bg} + E_{ref})^* \qquad (3.25)$$

The reference arm position is modulated periodically at a frequency $M \ll \Omega$. We can understand how this eliminates the multiplicative background by writing $E_0 = E_{nf} + E_{bg}$
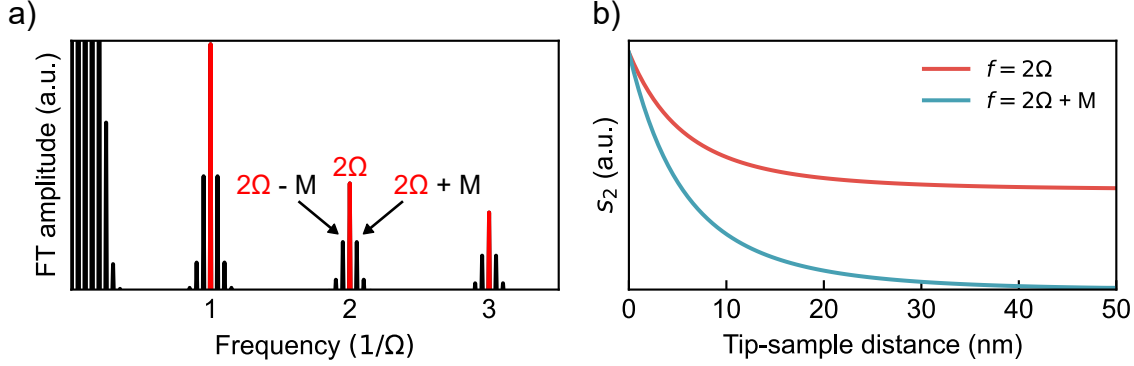
Figure 3.7: a) The FT spectrum at the detector acquires side-peaks at $n\Omega + mM$ (here $\Omega = 20M$) due to presence of the modulated reference beam at $f = M$. b) Demodulation at the side peaks $n\Omega + mM$ (blue curve) eliminates the multiplicative background in the scattered intensity calculated from the PDM. The approach curve of the signal demodulated at $n\Omega$ including the multiplicative background is shown in red.

and rewriting eq. 3.25:

$$I \propto |E_0|^2 + |E_{ref}|^2 + E_0 E_{ref}^* + E_0^* E_{ref} \tag{3.26}$$

For a single demodulation order n sufficiently high so that only the multiplicative background $\sigma_{bg,0}$ is relevant while $\sigma_{bg,n} \approx 0$ we can look at the frequency of the single terms in eq. 3.26. The first term is the one we had in the absence of the reference beam considered in eq. 3.23, appearing at $n\Omega$ and containing the multiplicative background. The time-modulated reference term can be written in phasor form as:

$$E_{ref} = \rho e^{i(\gamma \sin(mM)t + \Phi_R)} \tag{3.27}$$

where γ represents the amplitude of the mirror modulation and Φ_R is the average optical path difference between the signal and reference beam. The reference field can be expressed as its fourier series:

$$E_{ref} = \sum_{m=-\infty}^{\infty} \rho_m e^{imMt} \tag{3.28}$$

The frequency dependence of the second term $|E_{ref}|^2$ is therefore $mM \ll \Omega$. The third and fourth terms containing the product $E_0 E_{ref}$ have the same frequency. The fourth term when demodulating the signal at order n can be written as:

$$E_{0,n}^* E_{ref,n} = \sum_{m=-\infty}^{\infty} (\sigma_{nf,n} e^{-in\Omega t} + \sigma_{bg,0}) \rho_m e^{imMt} = \sum_{m=-\infty}^{\infty} \rho_m \sigma_{bg,0} e^{imMt} + \sum_{m=-\infty}^{\infty} \rho_m \sigma_{nf,n} e^{i(mM-n\Omega)t}$$
$$\tag{3.29}$$

The reference wave with modulation $f = M$ introduces side peaks at $n\Omega \pm mM$ as shown in Figure 3.7 a). The sidebands at $n > 0$ do not contain the multiplicative background, as shown in the second term of eq 3.29. Therefore demodulation at the side band frequencies of a sufficiently high n allows near-field measurements free of far-field background [66]. The suppression of the multiplicative background can be seen in Figure 3.7 b), where the PDM is used to calculate the near-field scattered signal, which is summed with the background (as in Figure 3.5) and the reference signal, and the intensity is computed. The red curve shows the approach curve for demodulation at 2Ω, where the multiplicative background is still present. The blue curve is obtained from demodulating the signal at $2\Omega + M$, which removes all the background contributions. The near-field signal is also enhanced by interference with the reference signal as can be seen from eq. 3.26. Moreover, it has been shown that by using adjacent sidebands $I_{n,m}$ the amplitude and phase of the signal of the complex scattered signal $s_{nf,n}e^{i\varphi_{nf,n}}$ can recovered from [66]:

$$
\begin{aligned}
s_{nf,n} &= 2.16k\sqrt{I_{n,1}^2 + I_{n,2}^2} \\
\varphi_{nf,n} &= \arctan\left(2.16k\frac{I_{n,2}}{I_{n,1}}\right)
\end{aligned}
\tag{3.30}
$$

where k is a proportionality constant. These relationship allow the retrieval of the complex-valued scattering assuming that the modulation depth of the reference mirror is equal to 0.21λ [66], where λ is the wavelength of operation. As a consequence, efficient extraction of amplitude and phase requires the use of a narrowband source. sSNOM coupled with the PsHet technique achieves deeply subwavelength near-field imaging by scanning the sample below the tip. Spectroscopic information can be acquired by changing the input frequency from a tunable source such as a QCL laser [63]. However, this requires acquisition of many images and can be time consuming. We will see in the next section that spectroscopic characterization can be achieved by coupling an FTIR setup to the sSNOM.

3.2.4   Nano-FTIR for broadband near-field spectroscopy

We have seen in the previous section how the coupling of a Michelson interferometer with the sSNOM allows suppression of far-field background and acquisition of both the amplitude and phase response of a sample. The same setup sketched in Figure 3.6 can be used to acquire interferograms and obtain spectroscopic informations through the FTIR technique introduced in section 3.1. While in the PsHet method the interferometer reference arm is modulated at high frequency, in the so-called nano-FTIR technique [68,69] the mirror is moved in discrete steps to record an interferogram from which the spectroscopic response can be retrieved by FT.

One important difference from the standard FTIR technique is that the interferometer used in nano-FTIR is asymmetric since one of the two arms of the setup is comprised by the sSNOM tip. As a consequence while the interferograms obtained in FTIR are always

symmetric around the zero-path difference point, this is not the case for nano-FTIR. The impact this has on the obtained spectrum is clear when writing the FT operation as:

$$\tilde{I} \propto \int_{-\infty}^{\infty} I(x) \underbrace{\cos(kx)}_{\text{even}} dx + i \int_{-\infty}^{\infty} I(x) \underbrace{\sin(kx)}_{\text{odd}} dx \tag{3.31}$$

Therefore if $I(x)$ is an even function the imaginary part of the FT is zero, and a real spectrum is recovered from the FT operation as customary in FTIR spectroscopy. In an asymmetric configuration the obtained spectrum is instead complex valued. It has been shown that the imaginary part of nano-FTIR spectra closely matches the absorption of the sample, while the real part follows the reflectivity [70]. These simple relations are valid for samples for which the parameter $\beta = (\varepsilon_s - 1)/(\varepsilon_s + 1)$ is not much larger than 1, which includes weak molecular oscillators (polymers, biological matter). Under these conditions, coupling with an analytical model for the tip-sample interaction the local dielectric function can be recovered from nano-FTIR spectra [70].

The multiplicative background is automatically eliminated while recording the interferogram in nano-FTIR. The intensity at the detector is described by eq. 3.25, which can be written as:

$$I \propto |E_{nf}|^2 + |E_{bg}|^2 + |E_{ref}|^2 + (E_{nf}E_{bg}^* + E_{nf}E_{ref}^* + E_{bg}E_{ref}^*) + c.c. \tag{3.32}$$

where $c.c$ indicates the complex conjugate of the three terms is parenthesis. If we consider the signal demodulated at order n:

$$I_n \propto |E_{nf,n}|^2 + (E_{nf,n}E_0^* + E_{nf,n}E_{ref}^*) + c.c. \tag{3.33}$$

To obtain the spectrum the FT integral with respect to the mirror position has to be computed. The dependence on the mirror position x appears only in the phase of the reference arm:

$$S_n \propto \int_{-d_0}^{d_0} dx e^{i\omega x} \left[|E_{nf,n}|^2 + (E_{nf,n}E_0^* + E_{nf,n}E_{ref}(x)^*) + c.c. \right] \tag{3.34}$$

Where $\pm d_0$ is the limit position of the reference mirror. The terms $|E_{nf,n}|^2$ and $E_{nf,n}E_0$ do not depend on x, and therefore do not contribute to the computed spectrum. The only relevant term for the nano-FTIR spectrum is then $E_{nf,n}E_{ref}(x)$, which does not contain any background contribution.

While it has been shown that nano-FTIR spectra can be acquired with a thermal source [71], in practice coherent broadband lasers with much higher brilliance are routinely employed to enhance the SNR and reduce the measurement time [68].
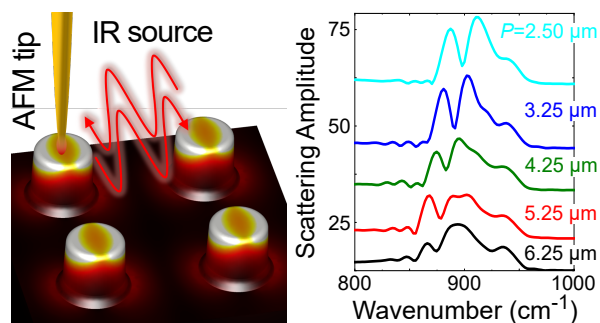
Chapter 4

Far and near-field spectroscopy of a SiC metasurface

In the introduction we discussed how LSPhP easily outperform plasmonic antennas due to the slower phonon-phonon scattering mechanism. In this chapter we investigate a SiC metasurface made out of cylindrical pillars supporting high Q-factor LSPhP.

Arrays of SiC pillars [73, 74, 75] have attracted considerable attention thanks to their ease of fabrication and rich em response, with broadly tunable modes [76], strong interaction between propagative and localized resonances [77, 78], and nonlinear response [79, 80, 81]. 3C is the SiC polytype of choice due to its simple isotropic permittivity and absence of additional folded optical phonons falling inside the RS band [82], which have been shown to perturb the LSPhP of the pillars in the 6H polytype [73]. Additionally, the low optical losses of SiC make it one of the best materials for fabricating antennas supporting LSPhPs [22].

As reported in more detail previously [76, 77], SiC pillar structures are fabricated by dry etching of a 3C-SiC layer through a hard mask fabricated by standard e-beam lithography, so that the pillars are supported by a SiC substrate. The resulting pillar height and diameter are both around 1 μm, while the interpillar spacing P, defined as the distance between adjacent pillar centers, is varied from 2.5 μm to 6.25 μm. In Figure 4.1 a) a SEM

image of a portion of one of the arrays ($P = 4.25\,\mu m$) is shown.

4.1   Far-field response of the SiC metasurface

The far-field optical response of the system is well understood [74] by considering the LSPhPs resonances of a single pillar coupled to the SPhPs of the bare SiC surface. The resonances of a single pillar in vacuum are composed of transverse modes, where the field oscillates along the pillar width, and longitudinal modes, where the field oscillates along the pillar height. The coupling can be described by the hybridization model, analogously to what happens for the resonance of plasmonic particles close to a metallic surface [83]. The array periodicity also folds the dispersion of the bare SiC SPhPs at $k_\parallel = 2\pi/P$, which can lead to hybridization of LSPhPs and SPhPs modes [77]. Of particular interest is the monopolar mode, arising from the coupling of the longitudinal dipole mode of the pillar with the bare SiC substrate. A monopolar mode in an isolated pillar in vacuum is forbidden by charge neutrality, which is provided in the coupled structure by the SiC substrate with negative ε_1. The charge of the monopolar mode spreads around the pillar base, generating coupling between adjacent pillars even at $\approx 3\,\mu m$ distance [76]. The modes resulting from coupling of the transverse resonances of a pillar to the SiC surface have been named transverse dipole (TD) modes [73,76]. While the coupling range between individual pillars is increased by the presence of the SiC substrate, near-field interaction can also occur between pillars in a dielectric environment. Coupling between single units of an array can also be mediated by far-field diffractive effects named Lattice Surface Resonances (LSRs) [84]. In previous experiments on SiC pillar arrays [73,76], two dips in reflectivity spectra have been associated with TD modes, which have been named transverse dipole 1 (TD1) and transverse dipole 2 (TD2). Polarization dependent measurements have been reported [85], showing that for *s-polarized* light the monopolar mode cannot be excited, as it requires an electric field component normal to the substrate, along the pillars height. The TD modes are instead relatively insensitive to light polarization, as there is always an electric field component parallel to the substrate surface along the pillars width.

We investigate the far-field optical response of the arrays with FTIR spectroscopy using a Bruker Hyperion microscope in reflection mode with a 15-magnification Cassegrain objective, which illuminates the sample with a weighted average incident angle of 25°. All spectra are normalized with a reference spectrum obtained on a clean gold surface. In Figures 4.1 b), c) experimental and simulated far-field spectra of arrays with different P are reported. Simulated spectra were obtained with a commercial solver (Lumerical) in time-domain and result from averaging s and *p-polarized* simluations, as in experiments the light source is unpolarized. In order to keep the incidence angle fixed at 25° (to match the experimental conditions) at all wavelengths we use the Broadband Fixed Angle Source Technique (BFAST) available in Lumerical. This is necessary as some modes of the metasurface shift with respect to the angle of incidence. The SiC dielectric function used in the simulations follows eq. 1.5 with $\varepsilon_\infty = 6.6$, $\omega_{TO} = 797\,cm^{-1}$, $\omega_{LO} = 973\,cm^{-1}$ and $\gamma = 1.4\,cm^{-1}$. While the superposition principle holds only for the fields and not for the
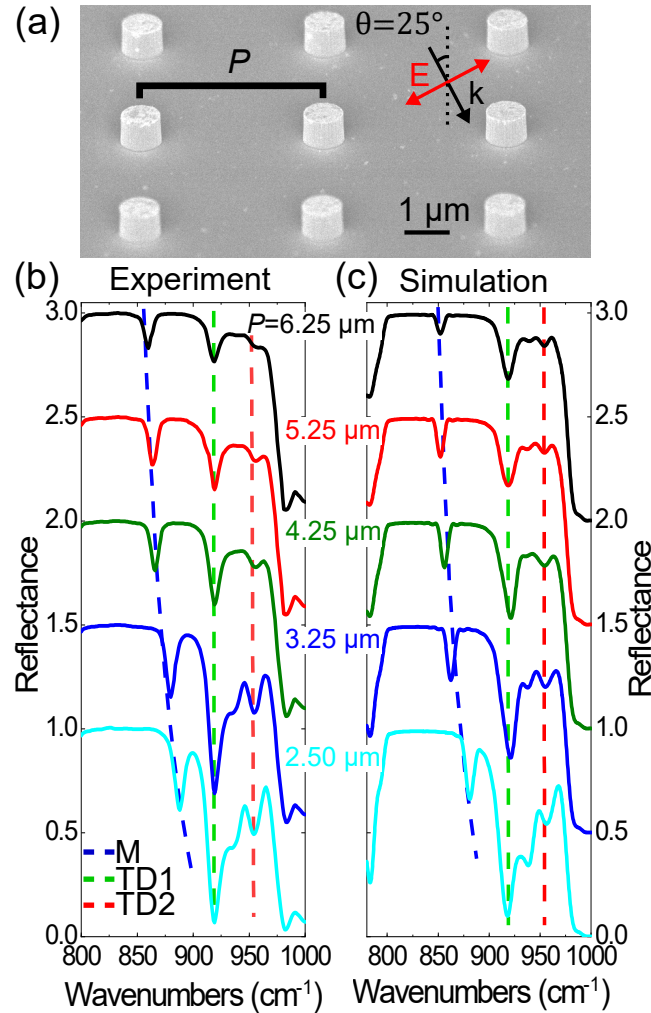
Figure 4.1: a) SEM image of a portion of the SiC pillar ($h \approx d \approx 1\,\mu m$) metasurface with spacing $P = 4.25\,\mu m$. b) Experimental FTIR and c) simulated spectra of the investigated arrays with different P. On the lower energy side, marked by a blue dashed line, the monopolar mode (M) redshifts as P increases due to reduced interpillar mode repulsion. At approximately $\omega_{TD1} = 920\,cm^{-1}$ and $\omega_{TD2} = 955\,cm^{-1}$ the first (TD1) and second (TD2) transverse dipolar modes are marked by green and red dashed lines, respectively. Subsequent spectra in b) and c) are vertically shifted by 0.5 for clarity.

Figure 4.2: a) Simulated reflectance spectra for the array with $P = 2.5\,\mu\text{m}$ calculated by averaging the reflectance spectra from *p-polarization* and *s-polarization* (red curve). Comparison with the spectra calculated by first averaging the fields from the two simulations which are then used to calculate the corresponding Poynting and reflec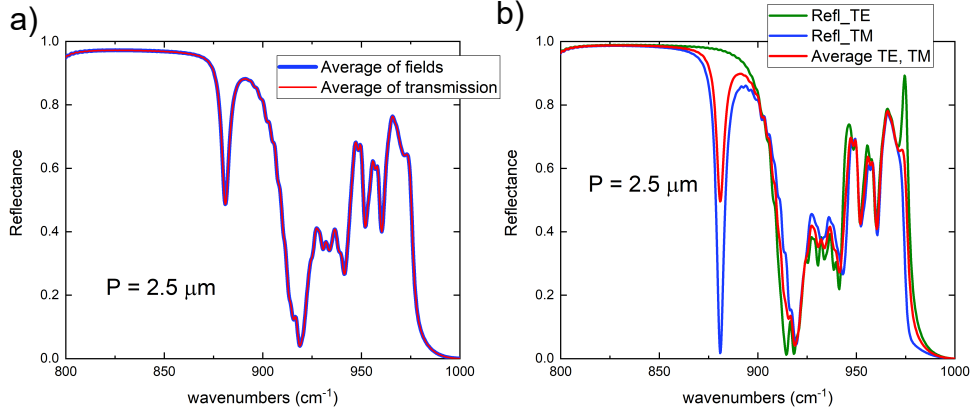tance spectra (blue curve). b) Simulated reflectance spectra for the array with $P = 2.5\,\mu\text{m}$ for *p-polarization* (TM, blue curve), *s-polarization* (TE, green curve) and their average value (red curve).

reflection spectra, we verified that for the present structure there is no difference between averaging the spectra and constructing the spectrum by first averaging the fields and then computing the reflected power. The reason why averaging the fields and then calculating the corresponding spectra, or averaging the spectra directly gives the same results can be understood as following. The reflection of the periodic structure is calculated from the fields recorded on a monitor placed above the source plane as:

$$R(\omega) = \frac{1}{2} \frac{\iint \text{Re}(\mathbf{P}(\omega)) \cdot \mathbf{dS}}{\text{sourcepower}(\omega)} \tag{4.1}$$

where $\mathbf{P} = \mathbf{E} \times \mathbf{H}$ is the Poynting vector and the integral is evaluated on the surface $\mathbf{S}$ of the monitor recording the fields. The cross product leads to the calculation of the energy flow in the direction perpendicular to the monitor surface. In the denominator sourcepower(ω) normalizes the result for the injected power. We then evaluate the Poynting vector calculated by averaging the fields from two simulations, one with *p-polarization* and one with *s-polarization*, and we use this to calculate the reflection spectra. In the Figure 4.2 a) we compare the result obtained in this way with the one obtained by directly averaging the reflection spectra from s and *p-polarized* simulations. In Figure 4.2 a) the two spectra cannot be distinguished, justifying the averaging of the reflection spectra for the present structure. The equivalence between the two procedures can be understood by looking at eq. 4.1. If we name the fields for the *p-polarized* simulation as $\mathbf{E_1}, \mathbf{H_1}$ and the ones for the *s-polarized* simulation as $\mathbf{E_2}, \mathbf{H_2}$, the question of whether averaging the reflection spectra is a legitimate procedure is equivalent to checking the following equation:
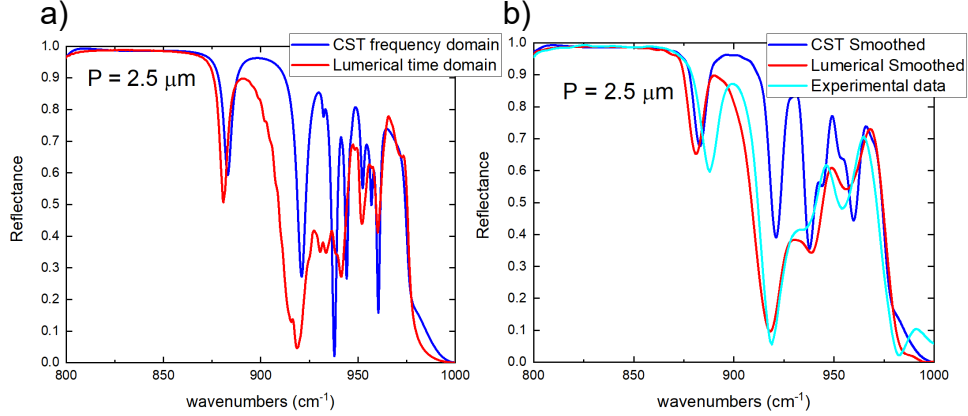
Figure 4.3: a) Comparison between the reflectance spectra for the $P = 2.5\,\mu m$ array obtained through frequency domain (blue lines) and time domain (red lines) simulations. In b) the same data are shown after Fourier smoothing with $n = 15$ together with the corresponding experimental data (light blue curve).

$$\mathbf{P}(\mathbf{E_1}, \mathbf{H_1}) + \mathbf{P}(\mathbf{E_2}, \mathbf{H_2}) = (\mathbf{E_1} \times \mathbf{H_1}) + (\mathbf{E_2} \times \mathbf{H_2}) \overset{?}{=}$$

$$\overset{?}{=} (\mathbf{E_1} + \mathbf{E_2}) \times (\mathbf{H_1} + \mathbf{H_2}) = \mathbf{P}(\mathbf{E_1} + \mathbf{E_2}, \mathbf{H_1} + \mathbf{H_2}) \quad (4.2)$$

Where the left hand side represents the averaging of the reflection from the s and p-*polarized* simulations, while the right hand side represents the averaging of the fields and the subsequent calculation of the transmission. The equation is satisfied if:

$$\mathbf{E_1} \times \mathbf{H_2} + \mathbf{E_2} \times \mathbf{H_1} = 0 \quad (4.3)$$

This is indeed true for the input fields due to the 90 degrees in-plane rotation between the two polarizations. If the interaction with the sample does not rotate in a different way the field components between the s and p-*polarization*, $\mathbf{E_1}, \mathbf{H_2}$ and $\mathbf{E_2}, \mathbf{H_1}$ are parallel and their cross product is null. We show in Figure 4.2 b) the reflectance spectra obtained from *s-polarized* and *p-polarized* plane wave simulations, together with their average. The main difference between the two polarizations is that with an *s-polarized* plane wave the monopolar mode cannot be excited as it requires a component of the field parallel to the pillar height.

Properly accounting for inhomogeneous broadening due to fabrication differences between single structures is not a trivial process [86], as all the relevant geometrical parameters should be randomly varied. For simplicity here we qualitatively account for inhomogeneous broadening by apply a smoothing procedure based on Fourier filtering with window $n = 15$, which dampens the sharper features in the simulated spectra. All spectra feature an increase in reflectivity corresponding to the SiC Reststrahlen band, while the resonances of the system appear as dips in this high-reflectivity wavelength range. The lower energy

resonance, marked by a blue dashed line in Figure 4.1 b) and c), can be identified as the monopolar mode, which redshifts with increasing P due to reduced pillar repulsion [76]. By green and red dashed lines at $\omega_{TD1} = 920\,\mathrm{cm}^{-1}$ and $\omega_{TD2} = 955\,\mathrm{cm}^{-1}$ the first (TD1) and second (TD2) transverse dipole modes are marked respectively.
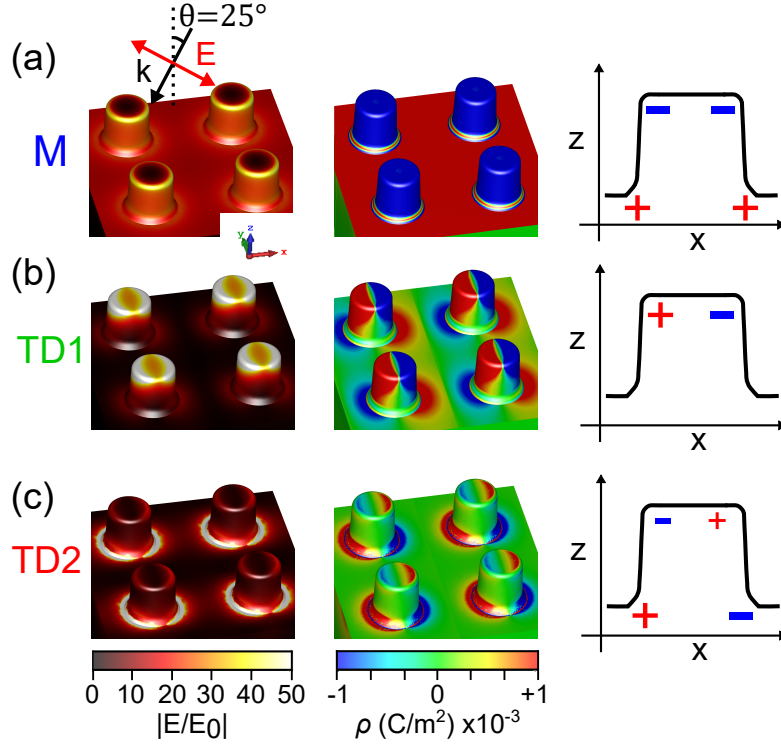

Figure 4.4: Simulated near-field maps for the monopolar mode M a), the first transverse mode TD1 b) and the second transverse dipole mode TD2 c). For each mode the field enhancement at the surface (left), surface charge density distribution (middle) and sketch of the charge distribution in the $x - z$ plane (right) are shown.

To verify the assignment of the modes in Figure 4.1 b), c) we simulate the field-distribution at the corresponding frequencies. Time-domain simulations are slow for the investigated structure due to the high quality factor of the resonances and, except for Figure 4.1 c), we simulate the system in frequency-domain (with either CST Studio or COMSOL). We check that both simulation methods give similar results, but we use the time-domain results for the far-field spectra in Figure 4.1 as we get better agreement with the experimental data. A comparison between the spectra obtained in frequency-domain and time-domain for $P = 2.5\,\mu\mathrm{m}$ are shown in Figure 4.3 a). The peaks in the frequency-domain simulation (blue curve) are excessively sharp compared to the experimental data, possibly due to a combination of inhomogeneous broadening due to fabrication imperfections and underestimation of the SiC losses determined by the parameter γ in eq. 1.5. The peaks are broader in the time-domain simulation (blue curve), which might be due to the fields not being zero at the end of the simulation. The same simulations are shown together

with the experimental data (light blue curve) after smoothing with Fourier smoothing with window $n = 15$. Both simulations capture the main dips appearing in the experimental data, with a better agreement obtain from the time-domain data.

In Figures 4.4 a)-c) simulated field enhancements at the surface for the three main resonances are reported in the left column for the array with $P = 2.5\,\mu$m. The simulated surface charge density distribution (middle column) are reported together with sketches of the charge distributions in the $x - z$ plane (right column). The field distribution for the transverse dipole modes is much more confined at the pillar edges than for the monopolar mode. For this reason we do not see any significant shift for TD1 and TD2 with varying P. The transverse dipole modes can also shift due to interpillar coupling [76], but only for values of P much smaller then the one analyzed in this study. From the charge distribution it can be seen that while for the monopolar mode an increase in P induces a redshift, for the TD1 and TD2 modes it produces a blueshift, as the interpillar interaction is attractive. The small shoulder around $\omega = 935\,\text{cm}^{-1}$ can be attributed to a higher order transverse resonance, almost spectrally overlapped with the TD1 resonance.

4.2 Near-field response of the SiC metasurface

In the previous section we described the far-field response of the SiC metasurface. At the same time, many applications of this system might require coupling with other objects through near-field interaction, as in the case of enhance surface spectroscopies [87]. We have seen that in the presence of surface waves the near-field behaviour of the system can be very different from its far-field response. For example, the thermal emission form a SiC semi-infinite surface in the near-field is quasi-monochromatic due to the presence of evanescent SPhPs [88]. Therefore it is necessary to directly investigate the near-field response of the SiC metasurface to be able to exploit all its possible functionalities. To do this we employ the nano-FTIR technique introduced in section 3.2.4 to extract near-field spectra of the SiC metasurface. The measurements are carried in a commercial setup (neaspec).

In the following all sSNOM measurements are demodulated at the fourth harmonic 4Ω of the tip oscillation frequency and normalized to a reference spectrum obtained on a flat silicon surface $|E_{\text{s4,Si}}|$. We will indicate the normalized amplitude of the near-field measurements as $|E_{\text{s4}}/E_{\text{s4,Si}}|$. Since it is well known that the presence of the AFM tip can perturb the optical response of strongly resonating antennas [89,90,91], we do not use standard nano-FTIR tips ($r \approx 40\,\text{nm}$), instead choosing more conventional metal-coated AFM tips with smaller radius of curvature (Arrow-NCPt, $r < 25\,\text{nm}$).

To understand the near-field response of the system we probed with the AFM tip positioned either on the center of one of the pillars (position A) or on the substrate between the pillars at approximately $800\,\text{nm}$ from the pillar center (position B), as illustrated in the sketch at the top of Figure 4.5. Results are reported in Figure 4.5 a) and b) for positions A and B, respectively. Spectra in Figure 4.5 a) show that the response on the pillars is independent of the array spacing, since we can identify two peaks, marked with green and
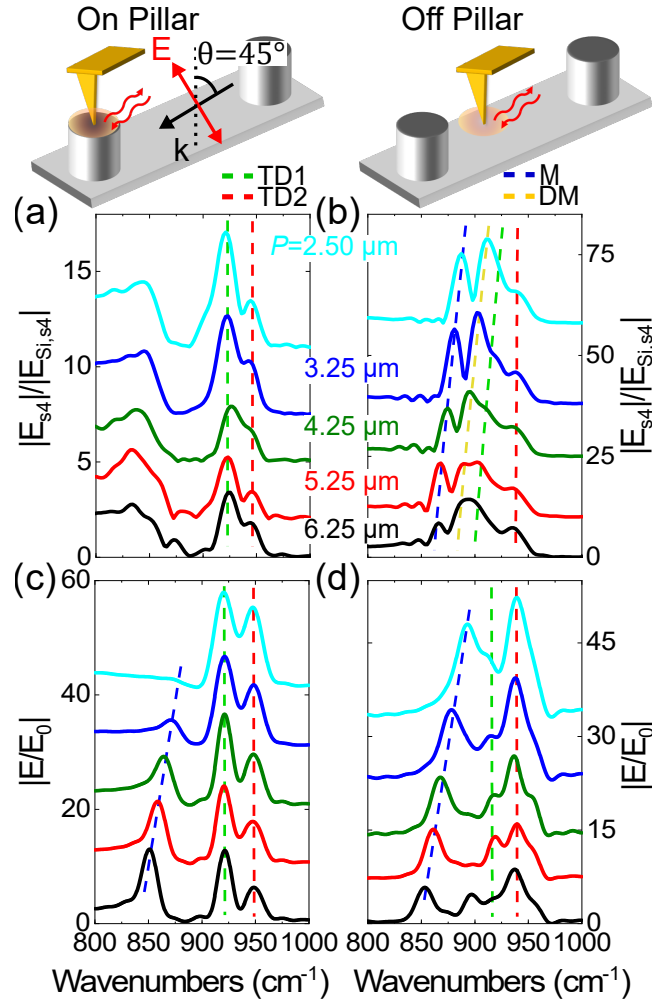
Figure 4.5: Near-field measurements of the spectral response for different array periodicity P. The spectra are collected either on a) the center of a pillar, or b) on the substrate inside the array at $\approx 800\,\mathrm{nm}$ from a pillar center. The different modes are indicated with dashed lines, using the same color code as in Figure 4.1: green for transverse dipole 1, red for transverse dipole 2, blue for the monopole and yellow for the dark mode. Simulated near-field enhancement spectra at $5\,\mathrm{nm}$ above the surface on top of a pillar c) and on the substrate between pillars d), matching the measurement geometry. Subsequent spectra in a)-d) are vertically shifted by $2.5; 15; 10$ and 7 respectively.

Figure 4.6: a) Near-field spectra measured on top of a pillar for different demodulation orders $n\Omega$ at TA = 60 nm. b) Same spectra as in a) shown for varying the tapping amplitude at 4Ω demodulation.

red dashed lines, at $920\,\mathrm{cm^{-1}}$ and $945\,\mathrm{cm^{-1}}$ for all the arrays. These match well with the frequenc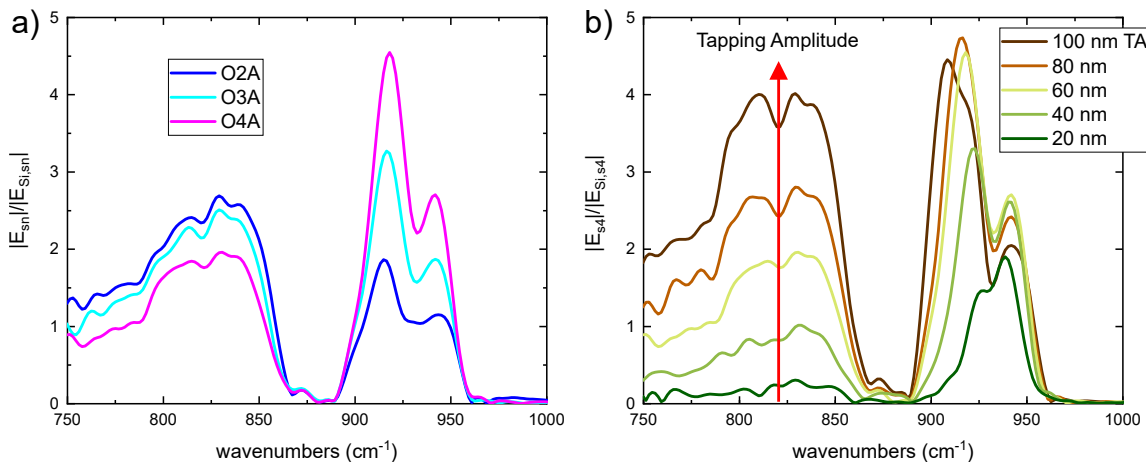ies of the first (red) and second (green) transverse dipole modes measured in the far-field at $\omega_{TD1} = 920\,\mathrm{cm^{-1}}$ and $\omega_{TD2} = 955\,\mathrm{cm^{-1}}$. The monopolar mode is absent when measuring at position A, while it is detected when measuring on the substrate and it appears as a lower energy peak which redshifts with increasing P, as shown in Figure 4.5 b). The frequency of the monopolar mode in the near-field is also found to closely match that reported in far-field measurements. Surprisingly at higher energies we see an additional mode, subject to similar redshifts, which cannot be associated with any far-field resonance. This is illustrated by a yellow dashed line in Figure 4.5 b). We associate this with a dark mode which, as it has no net dipole moment, can be excited only in the presence of the near-field illumination provided by the tip. The broad peak below $850\,\mathrm{cm^{-1}}$ in Figure 4.5 a) can be identified as a non-suppressed far-field contribution, as can be inferred from investigation of its amplitude as a function of increasing harmonic demodulation order $n\Omega$ and tapping amplitude as shown in Figure 4.6.

Interestingly, the signal from transverse dipoles is also detected when measuring on position B, as shown by the presence of peaks above the monopolar mode in Figure 4.5 b). Even though the frequency of the transverse modes is similar in Figure 4.5 a) and Figure 4.5 b), in the latter there is a small redshift with increasing P especially for TD1 (green line), indicating some weak interpillar coupling for the transverse modes when measured on the substrate. This feature is absent in the spectra collected at position A, indicating that this effect is mediated by the interaction with the tip.

In Figure 4.5 c), d) we report simulated spectra (CST, frequency domain) of the near-field amplitude at positions A and B, 5 nm above the pillar center and the SiC substrate respectively. In these simulations the incident angle of the light is set to 45° to better represent the experimental conditions, but no modeling of the AFM tip is attempted. In an FTIR type of experiment, the achievable spectral resolution is inversely proportional to the

distance over which the interferogram is recorded. Our sSNOM is equipped with a $800 \, \mu m$ long interferometer. We consider in the near-field simulations the finite spectral resolution affecting the experimental data by Fourier smoothing (same as used for the far-field spectra) the simulated spectra shown in Figures 4.5 c), d). The mode assignment in the simulated data is supported by checking the field distribution profile at the corresponding frequency. Simulated spectra only partially reproduce the measured data due to interaction between the AFM tip and the LSPhP antennas. Nevertheless, we can see that for both simulations on and off pillars in Figures 4.5 c) and d), the TD1 and TD2 transverse modes, marked by green and red dashed curves, lie close in frequency to the corresponding experimental data. Their relative amplitudes differ from the experimental values, and this could be attributed to the different illumination geometry and collection efficiencies, as the AFM tip predominantly backscatters the out-of-plane component of the field E_z. The small shoulder that can be see at $950 \, cm^{-1}$ in Figure 4.5 d) could be related to the excitation of SPhPs on the substrate at the frequency at which the SPhPs optical density of states is maximum [74].

Strikingly, simulations do not show at all the dark mode, marked with a yellow dashed line in Figure 4.5 b). This further suggests that this resonance is active only in the presence of the AFM tip, which acts as a near-field source, allowing the excitation of modes with no net dipole moment. In previous works on SiC pillars, the interaction between the monopolar mode and the SPhP originating from folding of the SPhP dispersion due to the array periodicity was considered [77]. We mainly do not see such an effect in this work since the parameter space we are exploring is almost outside the range where the two modes overlap. The only instance in which strong coupling between SPhPs and LSPhps could happen is in the largest measured array. Indeed in Figure 4.5 d) there is a new mode at $900 \, cm^{-1}$ seen for the largest pitch (black curve), which indicates a possible splitting of the modes as a result of strong coupling. However, such an effect is not clearly observed in the experimental data and is in general beyond the scope of this work, and it is not discussed in the following. We now investigate further the excitation of a dark mode by simulations in which we include the effect of the tip.

4.3 Influence of the AFM tip on the near-field response

Accurately simulating the experimental system is a complex task. Accounting at the same time for the local illumination from the tip and the periodic pillar array would come at high computational expense. The exact shape of the AFM tip is a relative unknown, affecting both excitation of pillar modes and how they radiate to the far-field detector. In order to qualitatively investigate the effect of the tip in inducing the dark mode observed in Figure 4.5 b) we model the tip as a gold sphere with radius $r = 30 \, nm$, placed $5 \, nm$ above a single isolated pillar. A more realistic modeling of the AFM tip should take into account its elongated shape. However, we expect to obtain similar qualitative results using a sphere
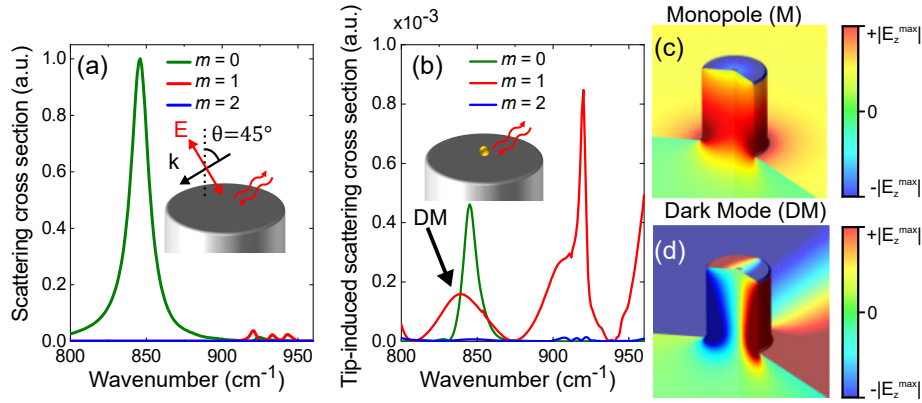
or a more elongated shape [72].

Figure 4.7: a) Simulated scattering cross section of a single isolated pillar on a SiC substrate. The different colors distinguish the scattering contribution from modes with different azimuthal symmetry m. b) Simulated tip-induced scattering cross section obtained by subtracting the far-field background. This procedure highlights the excitation of the dark mode (DM, indicated with a yellow line in Figure 4.5) activated by the introduction of the tip (modeled by a small metallic sphere). Map of the z component of the electric field at the frequency of the monopole c) and of the dark mode d).

To simulate the demodulation procedure at higher harmonics of the tapping frequency $n\Omega$ (which ensures that only light which has interacted at least once with the tip is recorded in the far-field), we first solve for the pillar in the absence of the sphere with plane wave excitation. We then we use this field as a background for the full simulation including the sphere. Doing this we isolate the tip-induced scattering from the far-field. These simulations are done in COMSOL and the background removal procedure is commonly referred as the "scattering problem" formulation. To reduce computational resources, the model is created in 2D-axisymmetric coordinates. Non-normal incidence at 45° for an axisymmetric model is achieved by expanding the plane wave as a sum of cylindrical waves [92]. In the scattering problem approach, there is a background field that is known and $E_{tot} = E_{bkgr} + E_{relative}$. The model is then solved for the $E_{relative}$ field, and the results are a good approximation of the perturbation induced by the scattering object (in our case, the gold sphere representing the metal tip). Both results from the background simulation and the scattering simulation are then available. The different contributions to the scattering cross section can be distinguished from their azimuthal angular dependence $e^{im\phi}$ of order m.

In Figure 4.7 a) the background far-field scattering cross section of a single pillar is shown, while in Figure 4.7 b) the tip-induced scattering cross section resulting from the background subtraction procedure is reported. Spectra in Figures 4.7 a), b) are normalized to the maximum of the isolated pillar scattering cross section. The scattering contributions are distinguished by their azimuthal symmetry order, so that it is easy to distinguish the monopolar mode with $m = 0$ symmetry from the transverse dipolar modes with $m = 1$

symmetry. The classification of the modes with their azimuthal number m is analogous to the classification of the hydrogen electronic wavefunctions with respect to the quantum number ℓ [74]. The spectra in Figure 4.7 b) show that on the red side of the monopolar mode, another peak with $m = 1$ symmetry appears, which is absent in far-field measurements. We associate this peak with the dark mode indicated by a yellow line in the experimental data of Figure 4.5 b). In Figures 4.7 c), d) the z component of the electric field in the presence of the metallic sphere is shown for the monopolar and dark modes, respectively. The dark mode is polarized out of plane like the monopolar mode, but switches polarization along the pillar axis, resulting in a zero net dipole moment and no coupling to the far-field. The polarization switch along the axis of the pillar means that the dark mode has an $m = 1$ character, similarly to the TD modes. Differently from other transverse modes, the dark mode has high field intensity in the interpillar region, which leads to a redshift similarly to what is experienced by the monopolar mode with increasing P. From Figure 4.7 b) it can be seen that another peak, slightly redshifted from the first transverse dipole, is also induced by the presence of the tip. This additional resonance arises from the coupling of the first transverse dipolar mode with the dipole induced by the tip, but it seems to have a lesser impact on the measured spectra, as no clear additional resonance close to the first transverse dipolar mode is seen experimentally in Figure 4.5 a) or 4.5 b).

Finally, to obtain the spatially resolved near-field distribution we perform a point by point measurement by collecting spectra while continuously scanning the tip, either on top of a pillar or off pillar. We report in Figure 4.8 colorplots of the measurements obtained in this way for the array with $P = 3.25\,\mu\text{m}$. In the inset (i), the scan direction, highlighted with a green dashed line, is plotted on top of a sketch of the corresponding portion of the sample. In (ii) we plot three spectra obtained at different positions, marked with three stars of different colors in both the sketches and colorplots. From Figure 4.8 a), we see that the TD2 mode (red dot) is efficiently excited only when the tip is in the middle of the pillar, while as we expect, the TD1 mode (green dot) shows higher intensity when measuring on the edges of the pillar and completely disappears close to the center, in the point marked by the red star. Referring to the simulated field enhancements of Figures 4.4 a-c), the monopole is expected to have high intensity only on the very edge of the pillar, which is hard to experimentally probe due to the high geometrical curvature of the region, leading to difficult sample-tip mechanical interaction. The TD2 resonance is not expected to have a maximum at the center of the structure (see Figure 4.4 c)) as experimentally reported, showing that the tip interaction heavily modifies the field distribution of this mode. The asymmetry of Figure 4.8 a) with respect to the pillar center can be attributed to the tilted illumination, which breaks the symmetry of the system. Interestingly, we detect the presence of an additional mode only when measuring close to the side of the pillar. By comparing its frequency with the off pillar measurements of Figure 4.5 b), we can identify this peak as the dark monopolar mode. This resonance is detected only on the side facing towards the illumination direction (from the right in the colorplots and in (i)). This asymmetry is consistent with previous studies of the perturbation introduced by the presence of an AFM tip on top of resonating antennas [89].

The colorplot in Figure 4.8 b) shows that the response of the substrate in between
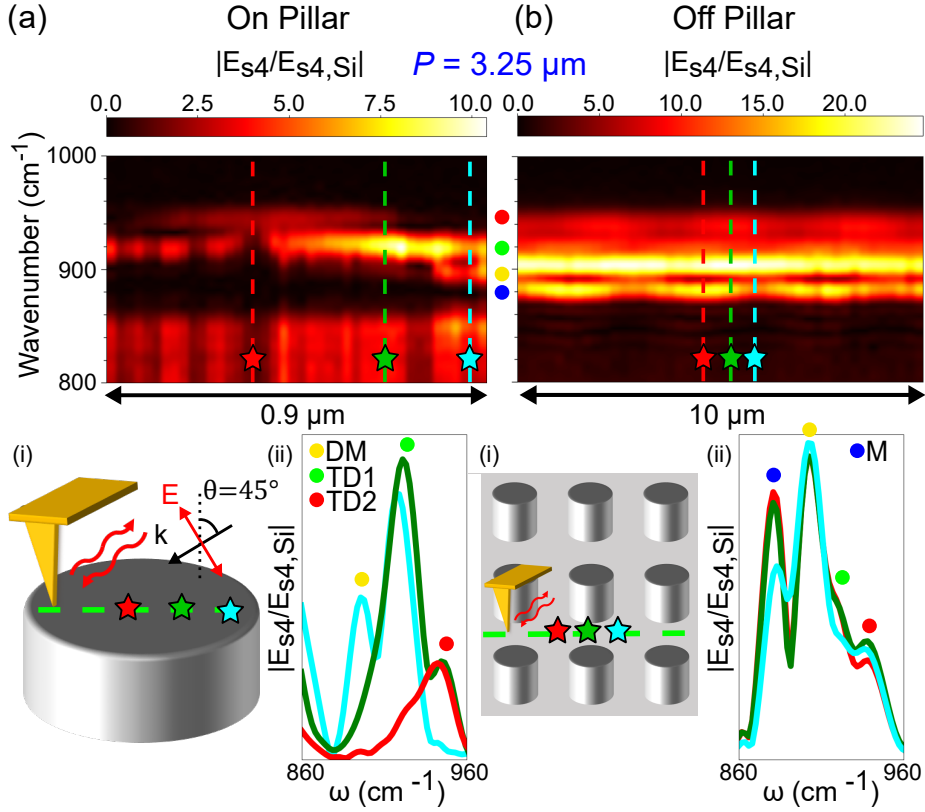
Figure 4.8: Color plots of the near-field spectra collected as a function of tip position when scanning on top of a pillar a), or on the substrate between pillars b). In (i) three selected spectra showing variations of spectral response in different positions are shown. In (ii) a sketch of the line along which the data where collected is reported. The stars represent the positions at which the spectra in (i) are taken.

pillars varies weakly with small intensity modulations. The response of the TD1 and TD2 modes is found to be stronger when scanning close to the base of a pillar, on the side facing towards the illumination source. The intensity of the monopolar mode follows instead an opposite trend, peaking for points equidistant from adjacent pillars. As expected from the simulated field distributions of 4.4 a-c), the response of the monopolar mode is stronger than that of the TD1 and TD2 modes when measuring off pillar. The weak frequency shifts seen at different positions in both Figures 4.8 a), b) can be at least partially attributed to coupling with the tip, as the use of conventional nano-FTIR tips with larger curvature radius increases these shifts as shown in Figure 4.9.

To further confirm the spatial pattern of the modes measured in Figure 4.8 a), we also perform hyperspectral imaging on top of one of the pillars as shown in Figure 4.10. To perform hyperspectral imaging one needs to record a large number of spectra to form a 2D map. This in principle would not be a problem in the absence of sample drift. We experimented that for measurements longer than $\approx$ 1 hour, sample drift becomes big enough to
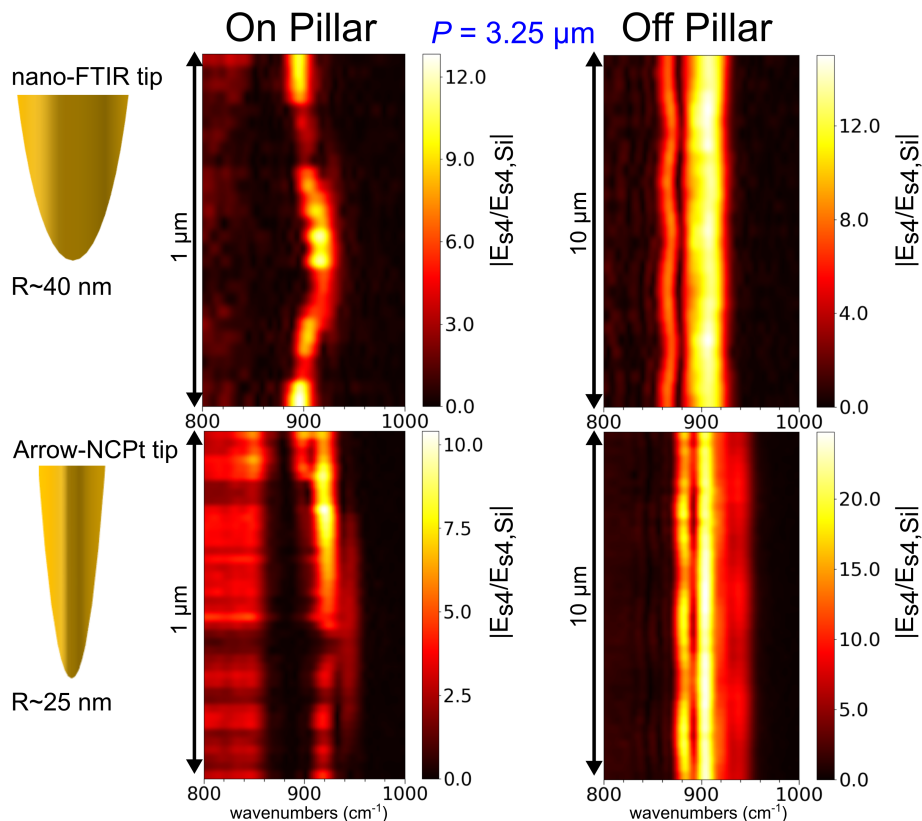
Figure 4.9: Comparison of linescans on pillar (left) and off pillar (right) with nano-FTIR tips (top row) and Arrow-NCPt tips (bottom row) for $P = 3.25\,\mu m$. The larger curvature radius of the nano-FTIR tips redshifts the peaks and causes larger spectral shifts when measuring at different positions on the sample

lead to unreliable mapping. In order to reduce the measurement time we use nano-FTIR tips, which produce larger signal but considerable redshifts, and we only map 1/4 of the disk. To obtain a full image we then assume circular symmetry, which is in principle not true due to the tilted illumination, but should provide a reasonable approximation. It has been shown that drift-free hyperspectral imaging can be performed by periodically acquiring AFM images after n spectral acquisition and use these for drift correction [93]. For simplicity, we preferred reducing the acquisition time of the hyperspectral imaging instead of implementing a drift correction procedure. The images reported in Figure 4.10 consist of 15×15 pixels and the acquisition time was $\approx$ 45 minutes. All the modes frequencies are redshifted in Figure 4.10 with respect to the ones reported previous figures due to the employment of nano-FTIR tips. The gray-shaded regions in Figures 4.10 c-f) represent the portions of the images obtained by leveraging the circular symmetry of the structure. We find that integrating the signal over two different frequency ranges confirms that the TD1 mode shows higher response on the edges, while TD2 is stronger in the center.
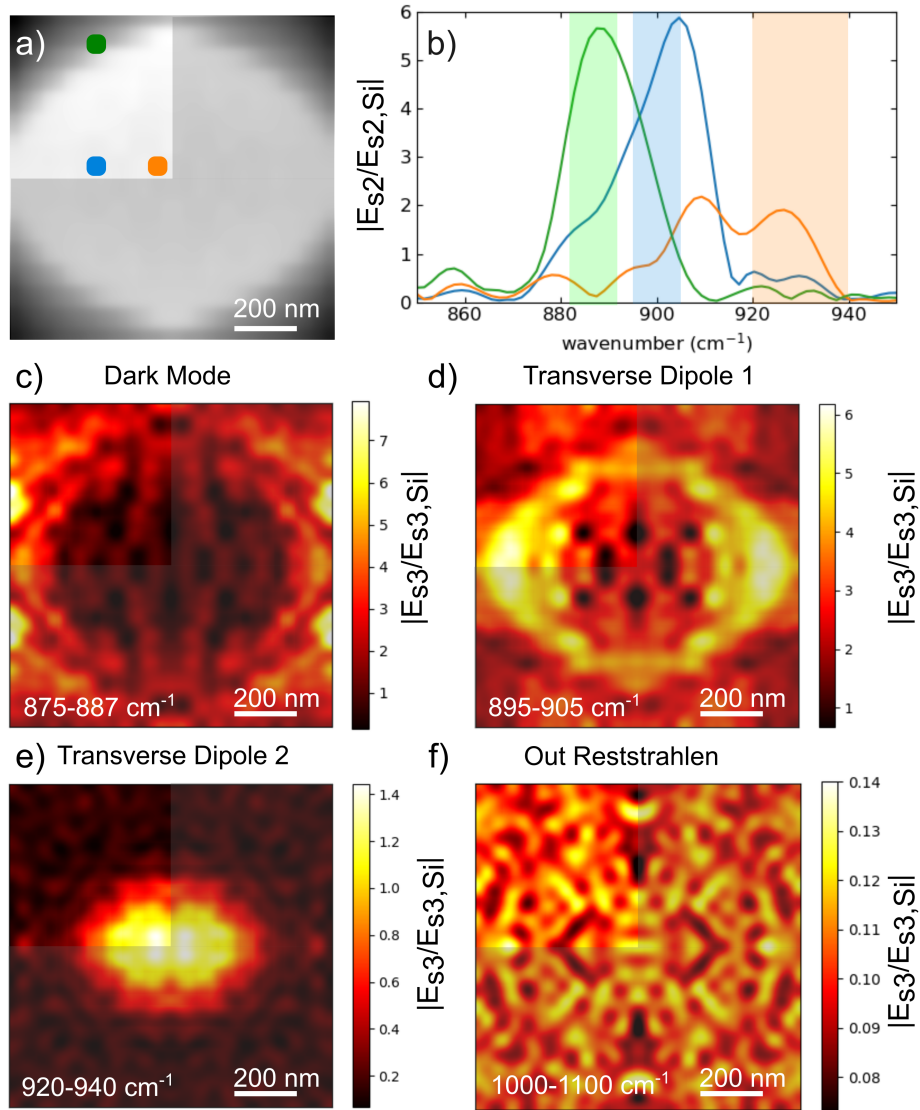
Figure 4.10: Hyperspectral imaging on top of a pillar for the array with $P = 2.5\,\mu\mathrm{m}$. To shorten the measurements time the spectra were recorded on 1/4 of the pillar and the full image reconstructed by circular symmetry. a) AFM of the investigated region, with colored dots representing the positions where the spectra of b) where collected. The colored areas represent the frequency regions used to produce images c-e). c-f) Images obtained by integrating the spectra over different frequency ranges, illustrating the localization of the different modes.

4.4   Conclusions

In conclusion, we reported in this chapter on the near-field study of the spectral response of a SiC pillar metasurface in the mid-IR by means of sSNOM. These results are of importance for enhancing the efficiency of mid-IR emitters or for manipulation of thermal emission at the nanoscale with phonon-polariton antennas. As the near-field spectral response of a system supporting surface wave excitation can be in general different from the response measured in the far-field, this study will help in the understanding of further experiments where SiC resonators are coupled to other systems through near-field interaction. We further employ electromagnetic simulations to understand the effect of the sSNOM tip in modifying the response of the metasurface. Even though such effects are not related purely to the near-field behavior of the antennas, similar perturbations can be expected to occur when coupling the LSPhPs resonators with other strong IR emitters or resonators.
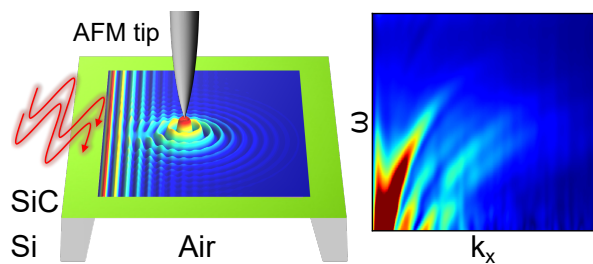
Chapter 5

SPhPs dispersion retrieval in large-area free-standing SiC thin films

In this chapter we discuss SPhPs in SiC thin films, and the retrieval of their dispersion through near-field measurements. As mentioned in the introduction, an intriguing feature of phonon polaritons is the possibility of anisotropic propagation due to the complex crystal structure of polar dielectrics, related to the simultaneous presence (i.e. at fixed frequency) of both positive and negative terms in the dielectric tensor [48, 94, 95, 96, 97, 98]. Thin films of layered van der Waals (vdW) materials have attracted considerable attention as they support highly anisotropic hyperbolic and elliptical phonon polaritons, combined with extreme subdiffractional confinement [45, 98, 99, 100, 101, 102, 103, 104]. Additionally, fabrication of twisted vdW bilayers has increased the dispersion engineering possibilities in these novel materials [105, 106, 107].

High quality crystalline vdW materials are currently obtained by exfoliation techniques, which are difficult to scale and result in flakes with limited sizes, hampering their implementation for practical applications. While first steps towards large-scale fabrication of

2D materials have been made via chemical-vapour-deposition and similar techniques, their seamingless implementation is still technologically challenging [108]. Thin films of conventional polar dielectrics can also produce deep subwavelength confinement of free-space light due to SPhPs hybridization, while allowing the use of more scalable fabrication processes. Strong confinement is achieved through the insulator-metal-insulator (IMI) configuration, which is well known for plasmonic films [109, 110, 111, 112]. Millimiter scale free-standing membranes of various polar dielectrics with tens of nanometer thicknesses are commercially available (see for example Norcada Inc. or Silson Ltd), but their application as a platform for SPhPs has yet to be explored. The presence of a solid substrate has been shown to be an additional source of polariton damping [113, 114, 115], highlighting the advantage of free-standing membranes. Silicon carbide (SiC) is an excellent material for SPhPs applications having a wide RS band and low losses [22, 116, 117]. Moreover, SiC is a widely used material in quantum optics [29, 118, 119] and power electronics [28], with well established fabrication procedures, facilitating its usage in a number of applications.
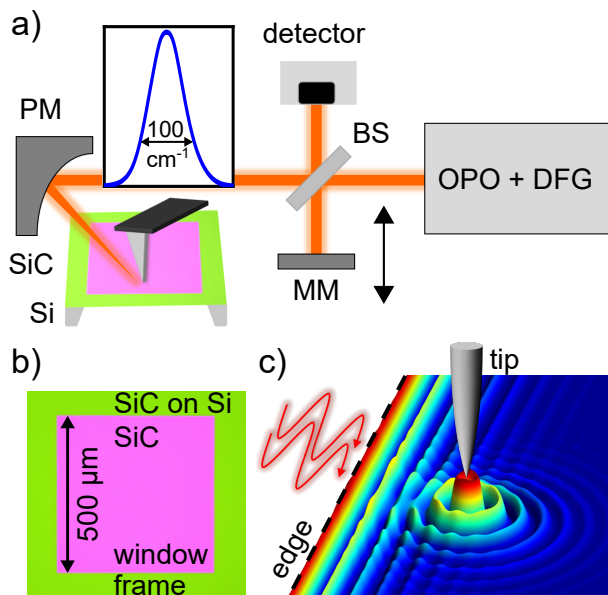
Figure 5.1: a) Sketch of the nano-FTIR setup used in the experiments (BS, beam splitter; MM, moving mirror; PM, parabolic mirror). The light source is an OPO laser with a DFG module, resulting in a MIR pulse with a bandwidth of $100 \, \text{cm}^{-1}$. Light is focused on the tip of an AFM by a parabolic mirror, and the back-scattered light is redirected towards a MCT detector by passing through a beam-splitter. b) Optical image of a SiC membrane window with a thickness of $200 \, \text{nm}$. c) Artistic representation of SPhPs launched by both the tip and the window edge.

Additionally, free-standing membranes of polar dielectrics have been shown to feature enhanced in-plane thermal conductivity associated with the presence of long-propagating SPhPs [120, 121, 122]. Surface pattering can be further leveraged to control the direction of SPhPs-induced heat flow at the nano and micro scales [123, 124]. Furthermore, the SiC RS

band matches the thermal emission wavelength of objects around room temperature and thin SiC films have been investigated in the context of enhanced near-field thermal energy transfer [111, 112, 125]. A number of experiments have confirmed this effect in nanometric gaps between polar dielectrics, where the thermal emission far exceeds the blackbody limit due to the contribution of evanescent SPhPs [126, 127, 128]. However, the optimization of all these applications requires fundamental knowledge of the SPhPs properties of polar thin films, while the experimental verification of the dispersion relation in such systems is still lacking.

We employ sSNOM to retrieve the SPhPs dispersion in SiC (polytype 3C) free-standing membranes (100 nm and 200 nm thick). sSNOM enables direct polariton measurements, as the presence of the tip provides the missing momentum for excitation in unpatterned samples, while offering subwavelength spatial resolution [99, 129]. We record position-dependent nano-FTIR spectra which allow the reconstruction of the dispersion relation at many frequencies in a single experimental run [129, 130]. A sketch of the experimental setup is shown in Figure 5.1a). The SiC membranes are supported by a silicon frame $\sim 400\,\mu m$ thick, with a $500\,\mu m \times 500\,\mu m$ square window in the center. An image of the top of a 200 nm membrane obtained with a 10X optical microscope is shown in Figure 5.1b). When scanning on the membrane, SPhPs are launched both from the tip and from the edge, as shown in Figure 5.1 c), producing complex interference patterns, of which we provide a detailed study in the next sections.

5.1 SPhPs hybridization in thin films

To confirm the optical properties of the SiC membranes we first investigate their far-field response by FTIR spectroscopy. In Figure 5.2 a) we show the analytically calculated normal-incidence reflectivity of free-standing SiC thin films of various thicknesses T in air, obtained from the Fresnel coefficients for a three-layer system according to eq. 2.17 where T is the SiC film thickness [23]. For decreasing T the reflectivity stays high around the TO phonon (at $797\,cm^{-1}$), while it substantially drops close to the LO phonon (at $973\,cm^{-1}$). The green line indicates the response of a semi-infinite SiC surface, showing high reflectivity in the whole RS band. Markers in Figure 5.2a) show the measured reflectivities for the 100 nm (light blue) and 200 nm (blue) membranes. We used for the calculations of the reflectivity the same SiC dielectric function employed in the previous chapter, which follows eq. 1.5 with $\varepsilon_\infty = 6.6$, $\omega_{TO} = 797\,cm^{-1}$, $\omega_{LO} = 973\,cm^{-1}$ and $\gamma = 1.4\,cm^{-1}$. The close match between the calculated and experimental reflectivity confirms that the optical properties of the SiC membranes can be modeled from literature values of the dielectric function.

In plasmonic thin films the surface plasmon polariton (SPP) dispersion splits into a lower and a higher energy mode [15], resulting from hybridization of the separate SPPs existing at the top and bottom interfaces. The splitting becomes appreciable when the film thickness T is reduced to values comparable to the material skin depth, on the order of few tens of nanometers in metals [109, 131]. In SPhPs thin films the skin depth is much
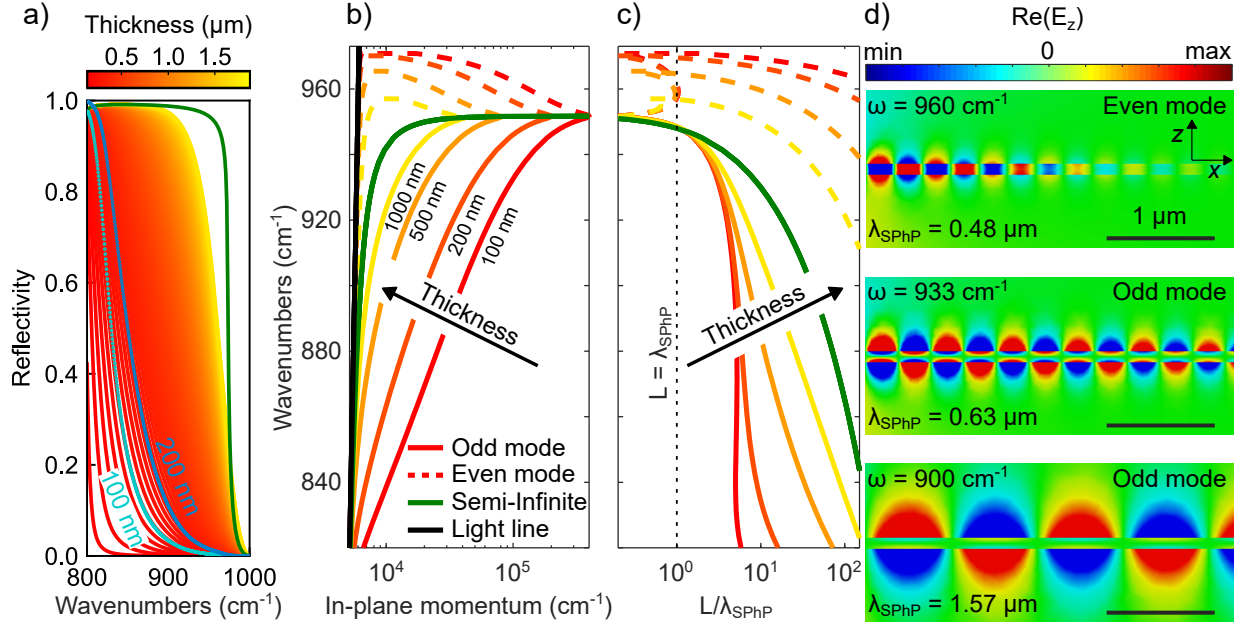
Figure 5.2: a) Calculated normal incidence reflectivity for a free-standing layer of SiC of variable thickness in air. Markers are experimentally measured quasi-normal incidence reflectivity spectra for 100 nm (light blue) and 200 nm (blue) SiC membranes. The green line is the reflectivity for a semi-infinite SiC surface. b) Theoretical SPhP dispersion in free-standing SiC films of various thicknesses. The single SPhP dispersion on a semi-infinite surface (green line) splits in films of finite thickness in a high energy mode (even mode) and a lower energy mode (odd mode). The splitting increases as the thickness decreases. For a range of frequencies above the green line asymptote, the even mode has two solutions. c) Calculated ratio between the propagation length and the SPhP wavelength for the same thicknesses in b). d) Simulated field profile at three different frequencies for a 100 nm membrane. The even and odd modes are named with respect to the symmetry of the electric field in the z direction normal to the SiC surface.

larger, with clear mode splitting visible already for $T = 1\,\mu\text{m}$ as shown in Figure 5.2 b). The dispersion of the two modes for a film of thickness T in a homogeneous medium with dielectric constant ε_2 are given by the following implicit relations [15, 109]:

$$
\varepsilon_1 k_2 + \varepsilon_2 k_1 \tanh\left(-i\frac{k_1 T}{2}\right) = 0
$$
$$
\varepsilon_1 k_2 + \varepsilon_2 k_1 \coth\left(-i\frac{k_1 T}{2}\right) = 0
$$

(5.1)

where $\varepsilon_1 = \varepsilon(\omega)$ is the dielectric function of the "metallic" layer and k_i are the wavevectors in the z direction (as the top and bottom materials are the same $k_2 = k_3$). In

our case $\varepsilon(\omega)$ is the SiC dielectric function. The in-plane SPhP wavevector β is related to the out of plane wavevectors k_i by:

$$k_i^2 = \beta^2 - k_0^2 \varepsilon_i \tag{5.2}$$

where where k_0 is the free-space wavevector. By substituting eq. 5.2 in eq. 5.1 two equation for the in-plane wavevectors $\beta = k_{ev}$ and $\beta = k_{odd}$ of the two modes can be written:

$$\sqrt{\frac{k_{ev}^2(\omega,T) - k_0^2 \varepsilon_2}{k_{ev}^2(\omega,T) - k_0^2 \varepsilon(\omega)}} = \frac{\varepsilon_2}{\varepsilon(\omega)} \times \tanh\left(\frac{T}{2}\sqrt{k_{ev}^2(\omega,T) - k_0^2 \varepsilon(\omega)}\right) \tag{5.3}$$

$$\sqrt{\frac{k_{od}^2(\omega,T) - k_0^2 \varepsilon_2}{k_{od}^2(\omega,T) - k_0^2 \varepsilon(\omega)}} = \frac{\varepsilon_2}{\varepsilon(\omega)} \times \coth\left(\frac{T}{2}\sqrt{k_{od}^2(\omega,T) - k_0^2 \varepsilon(\omega)}\right) \tag{5.4}$$

Equation 5.3 describes the dispersion of the higher energy even mode k_{ev}, for which the field component perpendicular to the film surface E_z is symmetric (even mode), while equation 5.4 describes the lower energy mode k_{od} for which E_z is antisymmetric (odd mode). In Figure 5.2 b) the numerical solutions of equations 5.3 and 5.4 for $\varepsilon_2 = 1$ are reported for selected values of T, along with the dispersion for a semi-infinite SiC slab in air (green line) and the vacuum light line $\omega = ck_0$ (black line). The energy splitting between the odd (solid lines) and even (dashed lines) modes increases as T is reduced, as shown in Figure 5.2 b). From Figure 5.2 b) one can see that for decreasing T the wavelength shrinking λ_0/λ_{SphP} for the odd mode is increased as the in-plane momentum increases at any given frequency. It should be noted that the even mode branch has two solutions above the frequency where $\varepsilon(\omega) = -1$ (corresponding to the asymptote of the semi-infinite slab dispersion), one close to the light line with practically no confinement, and another one at higher k. In Figure 5.2 c) we report the calculated ratio between the SPhP propagation length L and its wavelength λ_{SphP}. While not showing appreciable field confinement, the low-k even mode solution features very long propagation lengths, efficiently transporting thermal energy and enabling the enhanced in-plane thermal conductivity reported in thin films of polar dielectrics [120, 121, 122]. For a mode to be detectable in a polaritonic interferometry experiment, it has to travel at least one wavelength before decaying. As a consequence, the high-k vector even mode solution cannot be detected in our experiments as the ratio L/λ_{SphP} is below unity at all frequencies (see vertical dashed line in Figure 5.2 c)). In Figure 5.2 d) we show a snapshot of the simulated $\text{Re}(E_z)$ field profiles at three selected frequencies for a $T = 100\,\text{nm}$ membrane. In the top panel the high-k solution of the even mode (symmetric in E_z) can be identified due to the strong wavelength confinement and field symmetry. As it can be seen from Figure 5.2 b), this solution is characterized by negative group velocity ($d\omega/dk < 0$). This is a consequence of the field being concentrated in the "metallic" region where the Poynting vector parallel to the surface points in the negative direction (to the left in Figure 5.2 d)) [110]. The low propagation length of this mode is associated with increased losses in the SiC film due to the field being concentrated inside the material, which has been leveraged for enhanced

second harmonic generation [132]. This weakly propagating mode is usually named epsilon near zero (ENZ) mode [133] as for sufficiently small T the even mode dispersion is pushed towards the $\varepsilon(\omega) = 0$ line. In the two bottom panels of Figure 5.2 d) the odd mode solution (antisymmetric in E_z) is shown for two different frequencies. From Figures 5.2 b), c) and the simulated field profiles, one can see that there is a general trade-off between propagation length and wavelength shrinking for the SPhPs. The $\mathrm{Re}(E_z)$ symmetry determines the energy of the two modes: the charges at fixed x inside the SiC layer at the top/bottom interfaces have the same sign in the even mode, raising the energy due to repulsion, while they have opposite sign for the odd mode, lowering the energy due to attraction.

5.2 Polariton interferometry of the free-standing SiC films

To experimentally reconstruct the SPhP dispersion in the membranes, we use the nano-FTIR sSNOM technique in a commercial setup (neaspec), where a broadband source is coupled to an AFM in an asymmetric interferometer configuration (see sketch in Figure 5.1 a), allowing the measurements of near-field spectra with subwavelength spatial resolution [63, 129, 130]. We use illumination from an optical parametric oscillator (OPO) laser (Stuttgart Instruments), feeding a difference frequency generation (DFG) module, where the MIR output is realized by DFG between the signal and idler outputs (see Methods section for more details). The bandwidth of the MIR laser pulse is approximately $100\,\mathrm{cm}^{-1}$, resulting in high signal-to-noise measurements thanks to the high power per frequency [134]. This is essential as the low membranes reflectivity close to the LO phonon leads to a very weak signal [135].

In our measurements we use the edge of the SiC window to launch and reflect SPhPs, but equivalent experiments can also be performed by etching a slit in the membrane [39]. SPhPs are in principle also launched outside of the window on the frame, however the presence of the high refractive index Si substrate redshifts the odd mode and dramatically reduces the SPhPs excitation efficiency [39]. It is well known that the measured polariton fringes periodicity is in general different from the wavelength of the polariton itself [131, 136, 137]. The sSNOM signal originates from interference between propagating polaritons and directly back-scattered light (interference between different polaritons can be neglected due to their small intensity [131]), which can be written as:

$$I(x) \approx |E_{bs}|^2 + 2\sum_l |E_{bs}||E_l(x)|\cos((\phi_{bs} - \phi_l)(x)) \tag{5.5}$$

where x is the scan direction. Here E_{bs} is the field directly back-scattered from the tip, related only to the properties of the material below the tip which we consider to be position independent. $E_l(x)$ is the field of the polaritons launched by the tip, by an edge or any other scatterer in the sample that can provide the missing momentum for polariton excitation. The phase difference between the field back-scattered from the tip and the phase
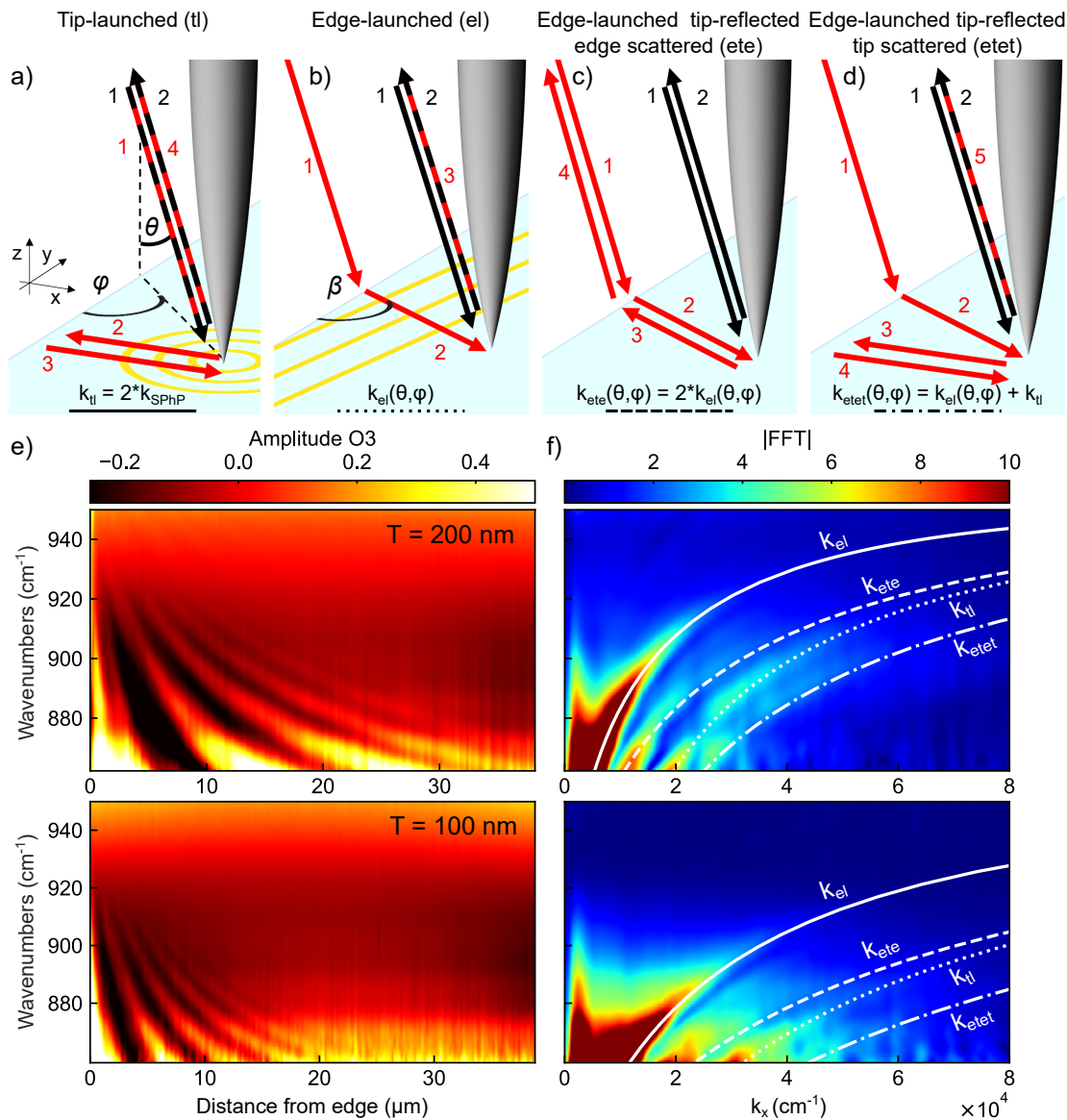
Figure 5.3: Multiple SPhP pathways (red arrows) contribute to the sSNOM signal by interfering with the tip backscattered light (black arrows). a) SPhPs radially launched from the tip are reflected by the edge $k_{tl} = 2k_{SPhP}$. b) SPhPs are launched from the edge and scattered by the tip and $k_{el}(\theta, \varphi)$ depends on the angles θ and φ. c) Edge-launched SPhPs are reflected as spherical waves from the tip and back-scattered from the edge $k_{ete} = 2k_{el}$. d) Edge launched SPhPs reflected by the tip and subsequently by the edge produce a signal at $k_{el} + k_{tl}$. e) Baseline subtracted nano-FTIR amplitude spectra obtained by scanning from a window edge for $T = 200\,\text{nm}$ (top) and $T = 100\,\text{nm}$ (bottom) membranes. f) $|\text{FFT}|$ of the maps in e) along the x-axis. White lines are predicted dispersions corresponding to the processes in a)-d) with $\theta = 60°$ and $\varphi = 65°$.

accumulated by the polariton $\Delta\phi_{bs,l} = (\phi_{bs} - \phi_l)(x)$ determines the positions of maximum and minimum constructive interference and the fringes periodicity Λ. The accumulated phase depends not only on the polariton propagation, but also on the phase acquired in the optical pathways for excitation and scattering of the polaritons [138, 139]. We summarize in Figure 5.3 a-d) the main pathways producing a signal in our sSNOM experiments. Black arrows indicate the optical path of the directly tip scattered light E_{bs}, while red arrows indicate the path of the polaritons E_l (and of their in-out scattering optical path). The light incident angle with respect to the surface normal direction and with the window edge are respectively indicated as θ and φ. In Figure 5.3 a) the scheme for tip-launched polaritons is shown. Here, SPhPs are radially launched by the tip and reflected at the edge, travelling twice the tip-edge distance d, accumulating double the phase delay and producing fringes at $\Lambda_{tl} = \lambda_{SPhP}/2$. This is the most dominant contribution in 2D materials as the tip near-field momentum distribution matches well with the momentum of highly confined polaritons [45]. In Figure 5.3 b) the edge-launched contribution is illustrated: polaritons are launched by the edge and propagate towards the tip, which back-scatters them in the far-field. The total phase difference accumulated for edge-launched polaritons is the sum of ϕ_{edge} accumulated by the free-space light travelling towards the edge and the ϕ_{SPhP} acquired by the SPhP when propagating from the edge to the tip, minus the free-space phase acquired by the light directly hitting the tip $\Delta\phi_{el} = \phi_{edge} + \phi_{SPhP} - \phi_{tip}$. The angle β of the polariton propagation is determined by momentum conservation $k_{0,y} = k_{SPhP,y}$ along the edge direction y [131]. The polariton accumulated phase depends in this case from (θ, φ), producing fringes with periodicity of (see Appendix A for more details) [131, 136]:

$$\Lambda_{el}(\theta, \varphi) = \frac{\lambda_0}{-\sin(\theta)\sin(\varphi) + \sqrt{\sin^2(\theta)(\sin^2(\varphi) - 1) + n^2}} \tag{5.6}$$

where $n = \lambda_0/\lambda_{SPhP}$. While the processes described in Figure 5.3 a), b) are the most common contributions to the sSNOM signal, multiple reflections between tip and edge are also possible [130]. In Figure 5.3 c), d) we illustrate two of these possible multiple-interference pathways. Edge-launched polaritons can be re-launched by the tip towards the edge, causing back-scattering towards the detector, as shown in Figure 5.3 c). The phase accumulated by the polaritons is here doubled compared to the edge-launched case, producing fringes with periodicity $\Lambda_{ete} = \Lambda_{el}/2$. Finally, the edge-launched polaritons which are re-launched by the tip can be reflected again by the edge and scattered by the tip towards the far-field as shown in Figure 5.3 d). In this case the phase accumulation is the sum of the phase accumulated in tip-launched polaritons and edge-launched polaritons, leading to a fringe spacing of $\Lambda_{etet} = (\Lambda_{tl} + \Lambda_{el})/\Lambda_{el}\Lambda_{tl}$.

To reconstruct the SPhPs dispersion and confirm the existence of the processes described in Figures 5.3 a-d), we record spectra along a line perpendicular to one of the edges of the membrane. We align the membranes in order to have an angle φ between the k-vector of the incident light and the edge of $\varphi \approx 65°$. In Figure 5.3 e) we show the baseline subtracted spectra obtained in this way as a function of the edge-tip distance. In the top panel we report the result for $T = 200$ nm, while in the bottom panel the one
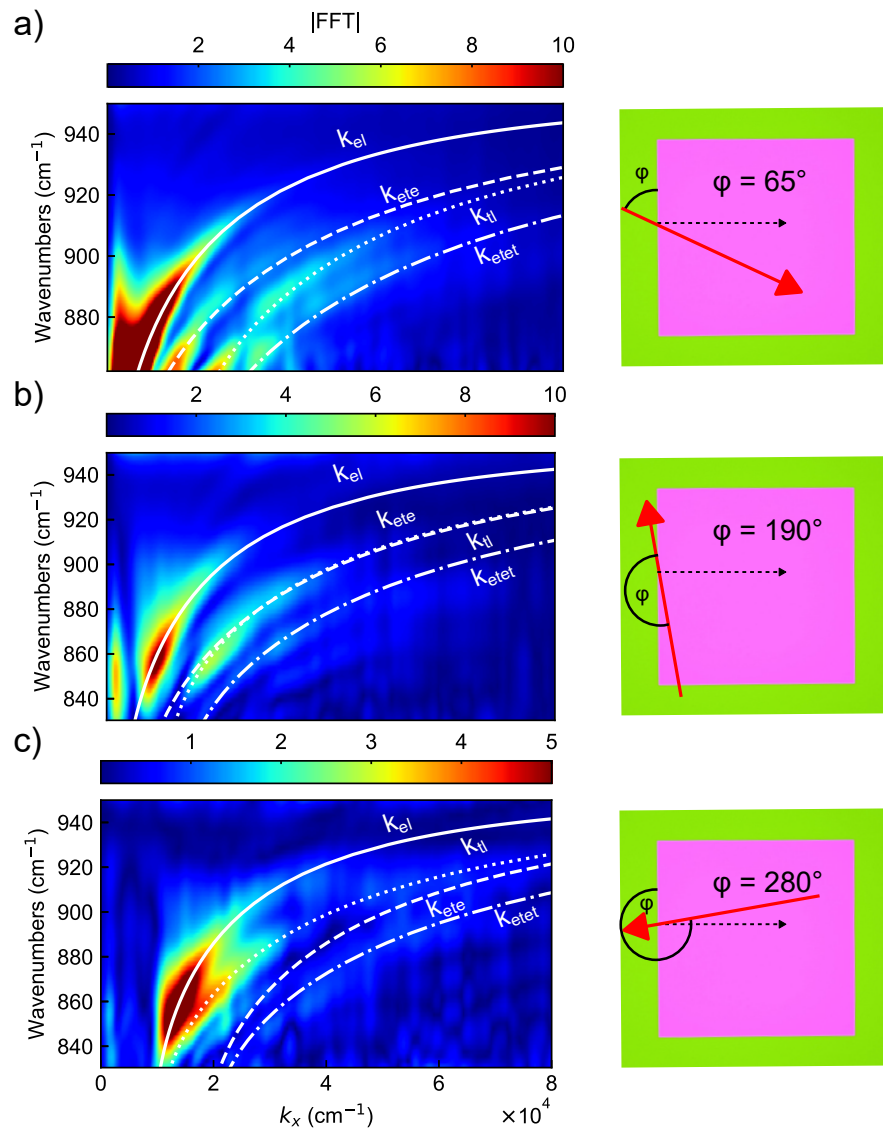
Figure 5.4: Experimental dispersion relation for different angles φ at fixed θ for $T = 200\,\text{nm}$. Dashed arrows indicate the scanning direction. Three significant situations are shown for the angle between the k-vector of the incident light and the scanning direction. In a) $\varphi = 65°$, b) $\varphi = 190°$ and in c) $\varphi = 280°$. The corresponding predicted dispersion branches are shown as white curves.

for $T = 100\,\text{nm}$. As anticipated in Figure 5.2 b) we see fringes with a higher spacing for $T = 200\,\text{nm}$ than for $T = 100\,\text{nm}$ due to the larger λ_{SPhP} (smaller in-plane momentum) in the thicker membrane. As can be seen from Figure 5.2 c), we expect the propagation length to be similarly reduced as does the polariton wavelength (the lines for $T = 100\,\text{nm}$ and $T = 200\,\text{nm}$ are almost overlapping). In order to retrieve the in-plane momentum $k_x(\omega)$ dispersion we fast fourier transform (FFT) each row in the maps of Figure 5.3 e) along the x axis. We follow the procedure outlined in previous works [129, 130] to obtain the maps of the FFT absolute value shown in Figure 5.3 f). Briefly, before performing the FFT, we mirrored the linescans along the first column, performed baseline subtraction for each row, applied a window function to have a smooth decrease at the edges and 0-padded the maps to increase resolution in k space [39].

In Figure 5.3 f) several branches appear in the dispersion maps, showing the complexity of the interference phenomena underlying the sSNOM signal in this system. From $k = 2\pi/\lambda$, we can reconstruct the expected dispersion related to the processes illustrated in Figures 5.3 a-d). Predicted dispersion relations are plotted as white curves in Figure 5.3 f) for $\theta = 60°$ and $\varphi = 65°$, showing good agreement with the experimental data (solid line for edge-launched, dashed for edge-launched-edge-scattered, dotted for tip-launched and dot-dashed for edge-launched-tip-scattered). To confirm the accuracy of the interference model, we performed additional measurements at different values of φ as shown in Figure 5.4. The angle φ between the illumination direction and the edge can be easily changed by rotating the sample, while θ is kept fixed. Changing θ would require a modification of the alignment to the parabolic mirror focusing the light on the tip, which is not easily achieved. In the right panels of Figure 5.4 the rotation of the membrane is sketched (for clarity in the sketch we fix the membrane and rotate the illumination direction). The dashed line indicates the scanning direction during data acquisition. We report the measurements for three significant membrane orientations, in Figure 5.4 a) the plane wave is incident (almost) perpendicular to the edge, while scanning is performed in the same direction of the k-vector. In Figure 5.4 b) the plane wave is almost parallel to the edge (note that $\varphi = 180°$ and $\varphi = 0°$ produce the same periodicity in the oscillations). In Figure 5.4 c) the plane wave is perpendicular to the edge, and we scan in the opposite direction of the k-vector. While the tip-launched contribution stays always the same, the dispersion of the other branches changes as predicted with the angle φ. It should also be noted that small shifts close to $\varphi = 90°$ (i.e. between $\varphi = 65°$ and $\varphi = 90°$) produce negligible changes in the predicted dispersion since $d\sin x/dx \approx 0$ for x close to $\pi/2$.

5.3 Retrieval of the SPhP dispersion

For further analysis we isolate the edge-launched contribution by multiplying the maps of Figure 5.3 f) by a window function centered around the solid white lines. The resulted windowed map is showed in Figure 5.5 a) for $T = 200\,\text{nm}$. The edge-launched SPhPs can be modeled as a plane wave decaying exponentially along its path due to material losses $I(x) = |E_{bs}|^2 + Ae^{-x\Gamma/2}\cos(k_{el}x)$. Neglecting the signal coming from the FFT of the first
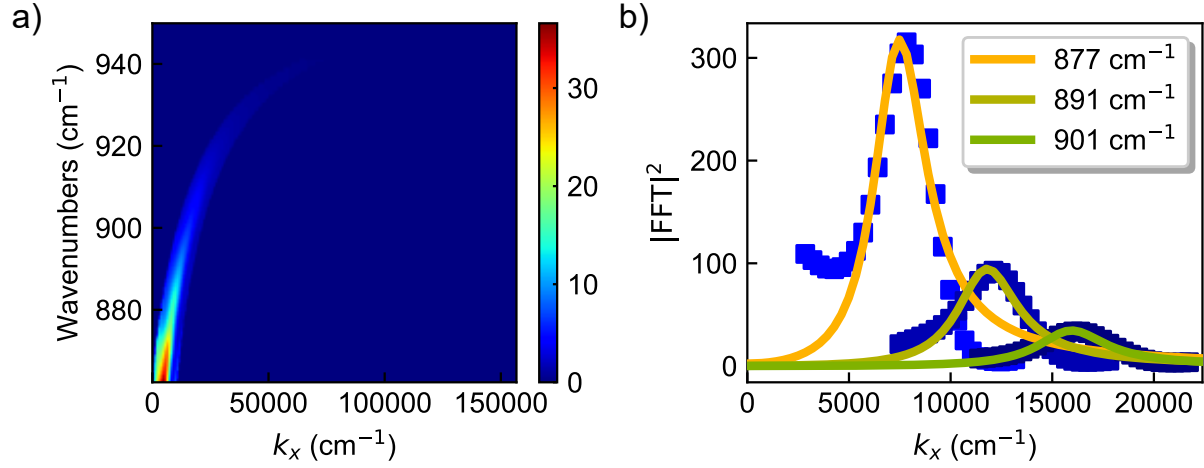
a)

b)

Figure 5.5: a) $|FT|$ map for $T = 200\,\text{nm}$ after product with the window function to isolate the edge-launched contribution. b) Example of the fitting of the isolated edge-launched branch at three selected frequencies.

term (producing only a DC contribution at $k = 0$), the squared module of the FFT of this function has the following form [131]:

$$|\,\text{FFT}(I(x))|^2(k) = \frac{A^2}{2\pi} \frac{(\Gamma/2)^2 + k^2}{(\Gamma/2)^4 + (k^2 - k_{exp}^2)^2 + 2(\Gamma/2)^2(k^2 + k_{exp}^2)} \tag{5.7}$$

We fit the square amplitude of the windowed maps row by row with eq. 5.7 as shown for selected frequencies in Figure 5.5 b). The extracted peak positions k_{exp} can be compared with the theoretical SPhP dispersion by inverting the relation $k_{el} = f(\theta, \varphi, k_{SPhP})$. From eq. 5.6, the experimental wavevector measured for the edge-launched polaritons is:

$$k_{el}^{exp} = k_0 \left(-\sin(\theta)\sin(\varphi) + \sqrt{\sin^2(\theta)(\sin^2(\varphi) - 1) + \left(\frac{k_{SPhP}}{k_0}\right)^2} \right) \tag{5.8}$$

Inverting this relation we get:

$$k_{SPhP} = k_0 \sqrt{\sin^2(\theta)(\sin^2(\varphi) - 1) + \left(\frac{k_{el}^{exp}}{k_0} + \sin(\theta)\sin(\varphi)\right)^2} \tag{5.9}$$

From the k_{el}^{exp} extracted through the fitting procedure shown in Figure 5.5 b), the dispersion k_{SPhP} can be recovered using eq. 5.9.

The data extracted in this way are plotted as green squares in Figure 5.6 a), in the top panel for $T = 200\,\text{nm}$ and in the bottom one for $T = 100\,\text{nm}$. The experimental data are shown together with the analytically calculated dispersion from eqs. 5.3 and 5.4 and with the calculated imaginary part of the Fresnel reflection coefficient obtained
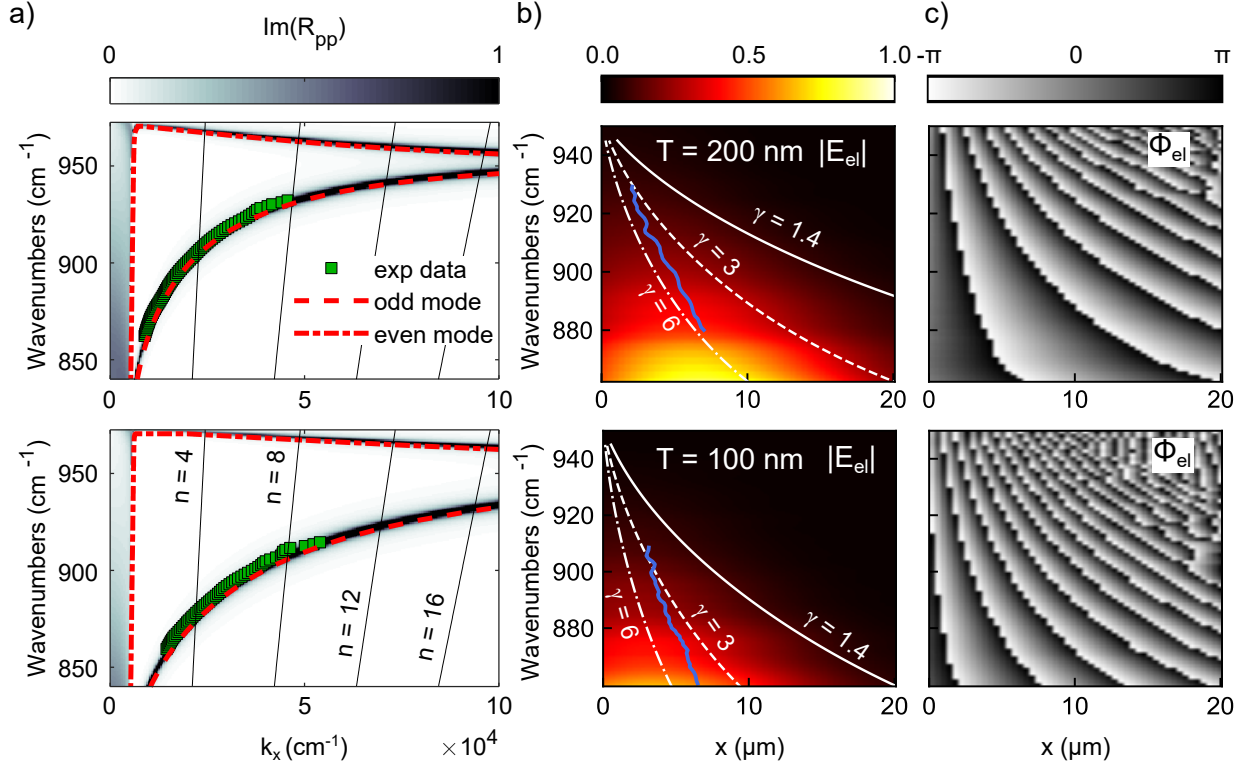
Figure 5.6: Retrieval of the SPhPs dispersion from the isolated edge-launched branch. Transfer matrix calculation of the imaginary part of the complex Fresnel reflection coefficient $\text{Im}(R_{pp})$ for membranes of $T = 200\,\text{nm}$ (top) and $T = 100\,\text{nm}$ (bottom). Red dashed lines are analytical solutions for the even and odd modes from equations 5.3 and 5.4. Green squares are extracted from the experimental data by fitting the isolated edge-launched SPhPs and inverting the relation $k_{el} = f(\theta, \varphi, k_{SPhP})$. Thin black lines indicate the confinement factor $n = k_x/k_0$. Amplitude b) and phase c) obtained by iFFT of the isolated edge-launched polariton branch. White lines in b) correspond to the theoretical value for the odd mode propagation length for different values of the damping parameter γ, while blue lines are the experimentally extracted values of the propagation length.
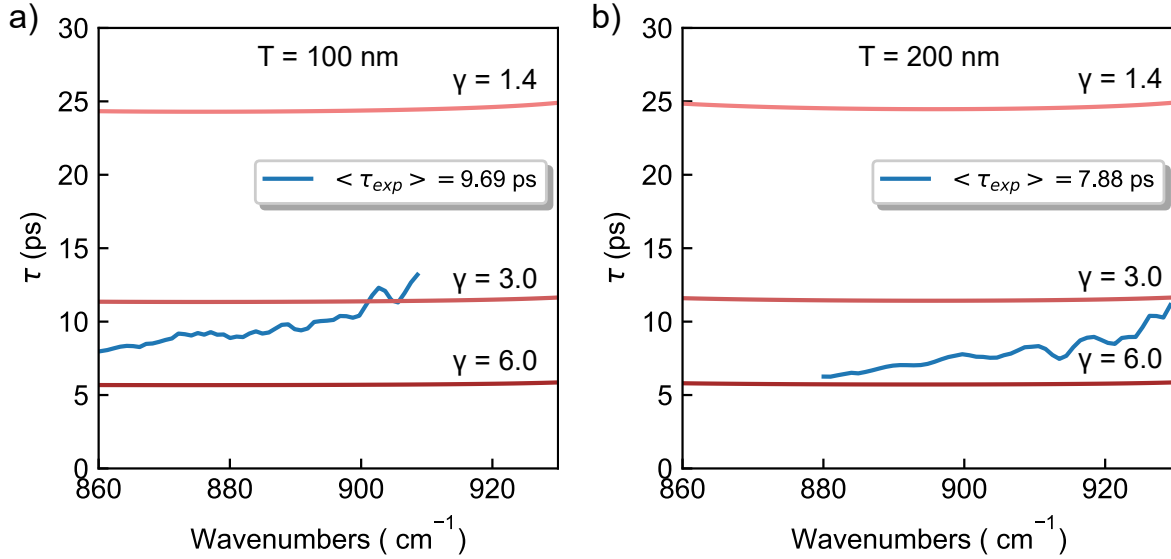
Figure 5.7: Experimental (blue lines) and theoretical values of the odd-mode SPhPs lifetime for membranes of $100\,\mathrm{nm}$ a) and $200\,\mathrm{nm}$ b) thickness. Theoretical curves are reported for three different values of the damping parameter γ appearing in the equation used to calculate the SiC dielectric function.

with the transfer-matrix method [51]. The extracted experimental data closely match the theoretically predicted values for the SPhPs dispersion in a thin film, demonstrating the reconstruction of the SPhPs dispersion through sSNOM. Black lines in Figure 5.6 a) indicate points with constant $n = \lambda_0/\lambda_{SphP}$, quantifying the free-space wavelength shrinking. In Figure 5.6 b), c) we report the amplitude and phase of the inverse FFT (iFFT) of the isolated edge-launched branch. In this case we multiply the maps of Figure 5.3 f) by a Hanning window centered around k_{el} to obtain a smooth iFFT [39]. White lines in Figure 5.6 b) are the theoretical propagation length $L = 1/2\,\mathrm{Im}(k_{odd})$ for the odd mode, where k_{odd} is calculated from equation (5.4). We report the theoretical L for different values of the damping parameter γ determining the imaginary part of the SiC dielectric function and the SPhP damping. Experimentally, we extract the propagation length L by fitting each row (each frequency) of Figure 5.6 b) with an exponential function [39]. We plot the extracted values as blue lines in Figure 5.6 b) for frequencies where the exponential fit gives reliable results. We find that the value of γ in these films has to be in between $\gamma = 3$ and $\gamma = 6$ to reproduce the experimental data. Values as low as $\gamma = 1.4$ have been reported for high quality bulk SiC, suggesting that improved crystal growth might lead to longer propagating SPhPs in free-standing SiC films. From the propagation length L and the group velocity $v_g = d\omega/dk$, the SPhPs lifetime τ can be extracted as $\tau = L/v_g$, as shown in Figure 5.7.

The average values of τ over the investigated frequency range are $\tau \approx 8\,\mathrm{ps}$ for the $200\,\mathrm{nm}$ film and $\tau \approx 9.5\,\mathrm{ps}$ for the $100\,\mathrm{nm}$ film. These values are comparable to what has

been reported for phonon polaritons in naturally abundant hBN [140] and $\alpha - \text{MoO}_3$ [45].
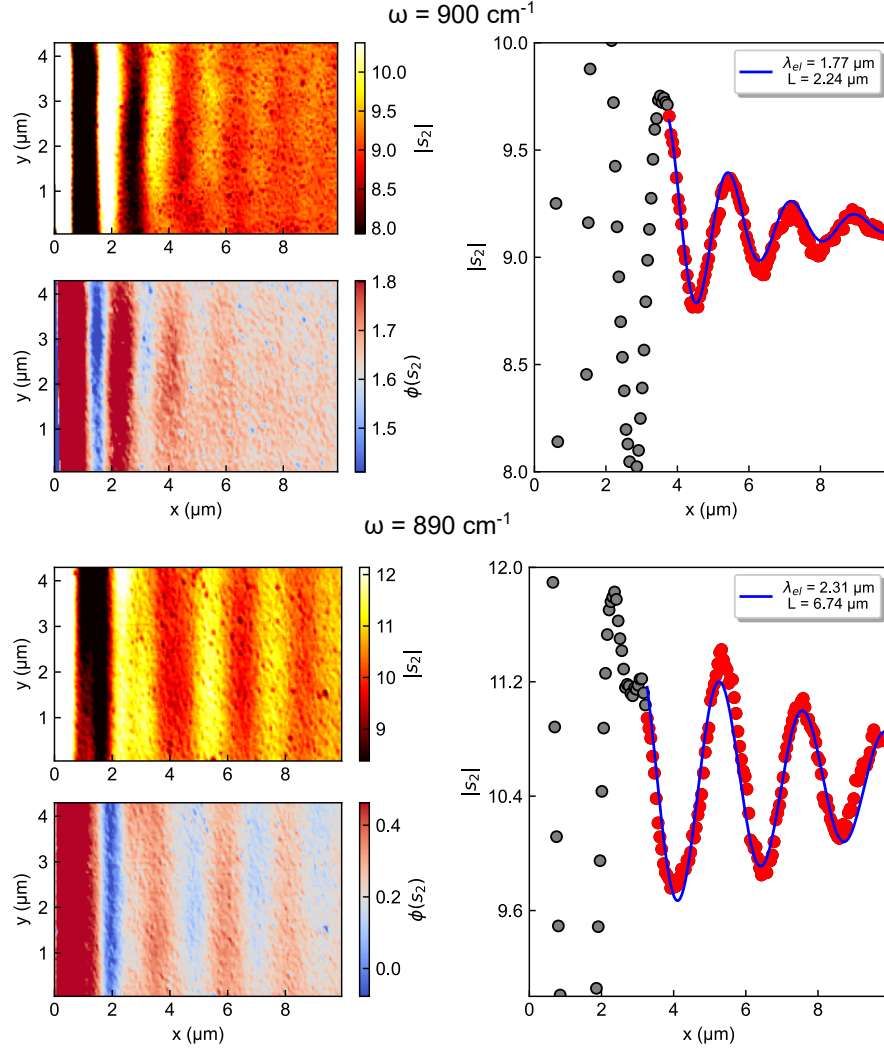

Figure 5.8: Nano-imaging of SPhPs launched on a 100 nm from a chromium strip at two representative wavelengths. Amplitude maps are averaged row-by-row and fitted with eq. 5.10 to extract the SPhPs wavelength and propagation length.

We employed nano-spectroscopy to recover the dispersion on a large frequency range, however nano-imaging with the PsHet technique described in section 3.2.3 usually can achieve higher signal-to-noise by averaging over many rows in an image. For our experimental setup this trade-off is not straightforward, as to obtain narrowband emission we need to filter the laser output by employing a monochromator, which dramatically reduces the available power. In this configuration no SPhP launching from the window edge was detected. In order to perform nano-imaging we pattern a 5 µm wide, 20 nm thick chromium strip on a 100 nm membrane with standard e-beam lithography, which is more efficient in

launching SPhPs. In Figure 5.8 we report the amplitude and phase results for two representative wavelengths ($890\,\mathrm{cm}^{-1}$ and $900\,\mathrm{cm}^{-1}$). In these experiments we only observe edge-launched SPhPs due to the strong launching efficiency of the chromium strip. To extract the SPhP properties we average row-by-row the amplitude maps. The resulting profile can be fit with an oscillating decaying exponential function:

$$y(x) = A_0 + A_1 \left(e^{-x/L} \cos\left(\lambda_{SPhP}x + \phi\right) \right) \tag{5.10}$$

We exclude from the fit the first interference fringe, where the tip strongly interacts with the chromium strip. From the fitting and considering the membrane orientation, the SPhP wavelength and lifetime can be extracted analogously to what was done for the nano-FTIR data. The values extracted from the nano-imaging experiments are consistent with what we obtained through nano spectroscopy [39].

5.4 Conclusions

In summary, in this chapter we have analyzed the SPhP dispersion in free-standing membranes of SiC with thicknesses of $100\,\mathrm{nm}$ and $200\,\mathrm{nm}$ through sSNOM near-field spectroscopy. We have performed a detailed study on the various interference pathways leading to the emergence of complex features in the sSNOM signal. In particular, we analyzed the effect of multiple SPhPs reflections between the tip and window edge. By fitting the experimental data we extracted the frequency-dependant SPhP momenta for both thicknesses, which agree well with theoretical calculations. The findings are corroborated by nano-imaging at selected frequencies. We introduced commercially available SiC free-standing membranes as a platform for phonon polaritonics, where the polariton wavelength can be controlled by the film thickness. We expect that novel experimental and theoretical works in the fields of enhanced near-field energy transfer and enhanced in-plane conductivity of free-standing SiC films could also benefit from our study and direct measurement of the SPhP dispersion.

Chapter 6

Near-field imaging of SPhP vortex in free-standing SiC thin films

In this chapter we discuss the near-field imaging of optical vortex in SiC carbide thin films, of which the dispersion was investigated in the previous chapter. SPhP vortex are created by spin to orbital momentum conversion driven by metallic spiral patterns fabricated on top of the SiC films. As the concept of optical vortex is closely related to the orbital angular momentum of light, we briefly introduce it here.

6.1   Orbital angular momentum of light

As a beam of light carries a linear momentum $\mathbf{P}$, one can naturally define an associated angular momentum as $\mathbf{L} = \mathbf{r} \times \mathbf{P}$. The total angular momentum can be defied in the paraxial approximation as the integral of the cross product between the position vector $\mathbf{r}$ and the linear momentum $\mathbf{P} = \mathbf{E} \times \mathbf{B}$ [141]:

$$\mathbf{j} = \varepsilon_0 \int \mathbf{r} \times (\mathbf{E} \times \mathbf{B}) \cdot \mathbf{dr} \tag{6.1}$$

For weakly focused beams in the paraxial approximation, the total angular momentum is given by the sum of the spin angular momentum $\mathbf{s}$ (SAM) and the orbital angular momentum $\boldsymbol{\ell}$ (OAM):

$$\mathbf{j} = \mathbf{s} + \boldsymbol{\ell} \tag{6.2}$$

The SAM is associated with a rotation of the electric and magnetic fields, and is carried by circular polarization with possible values $s = \pm 1$ depending on the handedness. The OAM is instead related to an optical beam having a helical wavefront that has a phase twist along the azimuthal direction in the plane perpendicular to the propagation direction. The phase profile of an OAM beam in such plane can be described by the simple expression $e^{i\ell\theta}$ where θ is the azimuthal coordinate and ℓ is the azimuthal mode index. The amplitude of the field has instead a doughnut shape, where the diameter increases with ℓ. The number

ℓ quantifying the number of 0 to 2π phase jumps in the transverse plane is also referred as the *topological charge* of the optical vortex. Beams carrying OAM can be described by Laguerre-Gaussian (LG) modes, which are characterized by two indexes $LG_{\ell,p}$ and their profiles for selected values of ℓ, p are shown in Figure 6.1. The index ℓ of the LG modes has the role of describing the topological charge of the optical vortex, while the index p is the radial index determining the number of oscillations. OAM beams can be formed in many ways, ranging from simple spiral phase plates [142] to precisely engineered metasurfaces [143].
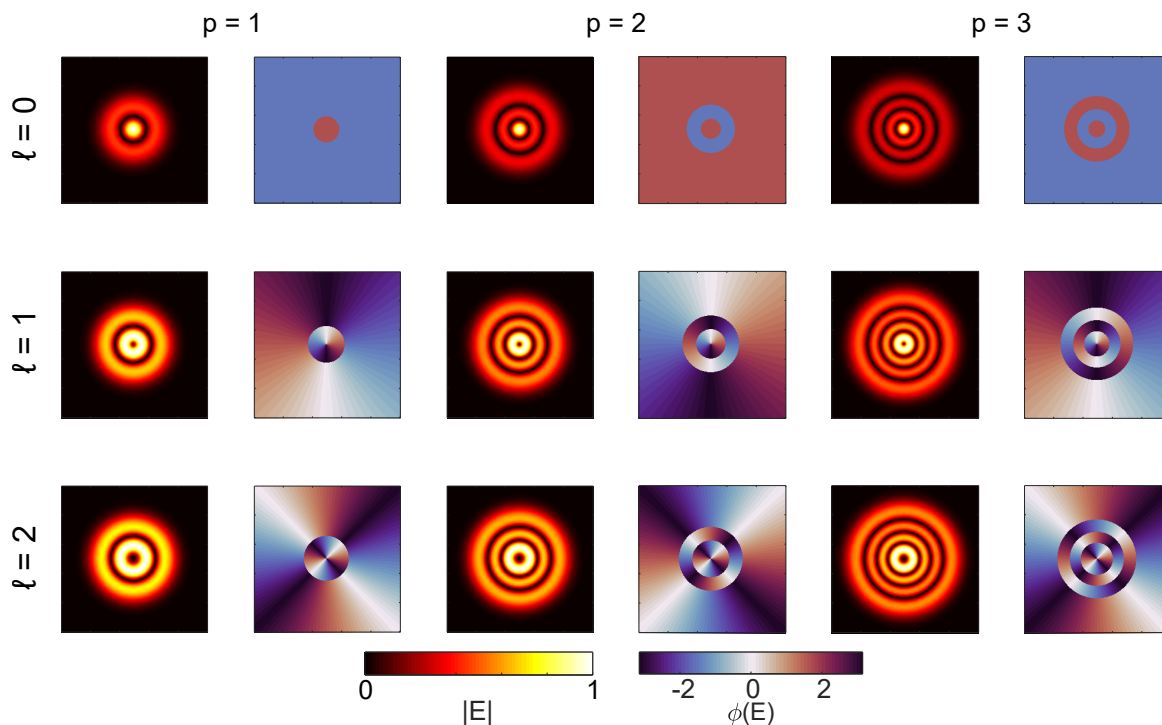

Figure 6.1: Amplitude and Phase of Laguerre-Gaussian modes for selected values of the indexes ℓ, p

An interesting properties of OAM beams is that they are mutually orthogonal (as LG beams are orthogonal to each other) and the associated topological charge ℓ is unbounded. As a consequence, OAM beams are a good candidate for information multiplexing [144], where different data can be encoded in distinguished topological orders which can be separated with minimal cross-talk due to orthogonality [141, 144].

6.2   Two-dimensional optical vortex

Traditional methods for the generation and detection of OAM light states rely on bulky free-space optics [145]. To shrink the footprint of these devices recently great attention has been given to the possibility of on-chip manipulation of optical vortex. SPPs have been the

main candidate to achieve such miniaturization, both for the generation [143] and detection of OAM states [146, 147]. On a more fundamental level, it has been theoretically predicted that deeply subdiffractional optical vortex fields could induce forbidden optical transition in quantum systems [148, 149]. A number of experimental works have demonstrated the generation of SPP vortex by near-field mapping through both aSNOM [150, 151, 152] and sSNOM [153, 154]. An advantage of sSNOM is that by employing the PsHet technique described in section 3.2.3 the phase profile of the SPP vortex is obtained, which allows a direct access to the topological charge. When only the amplitude of the field is available, the tolopogical charge has to be inferred by the diameter of the doughnut intensity pattern. Recently, ultrafast imaging of SPP vortex below the diffraction limit has been demonstrated through two-photon photoemission electron microscopy [155, 156].
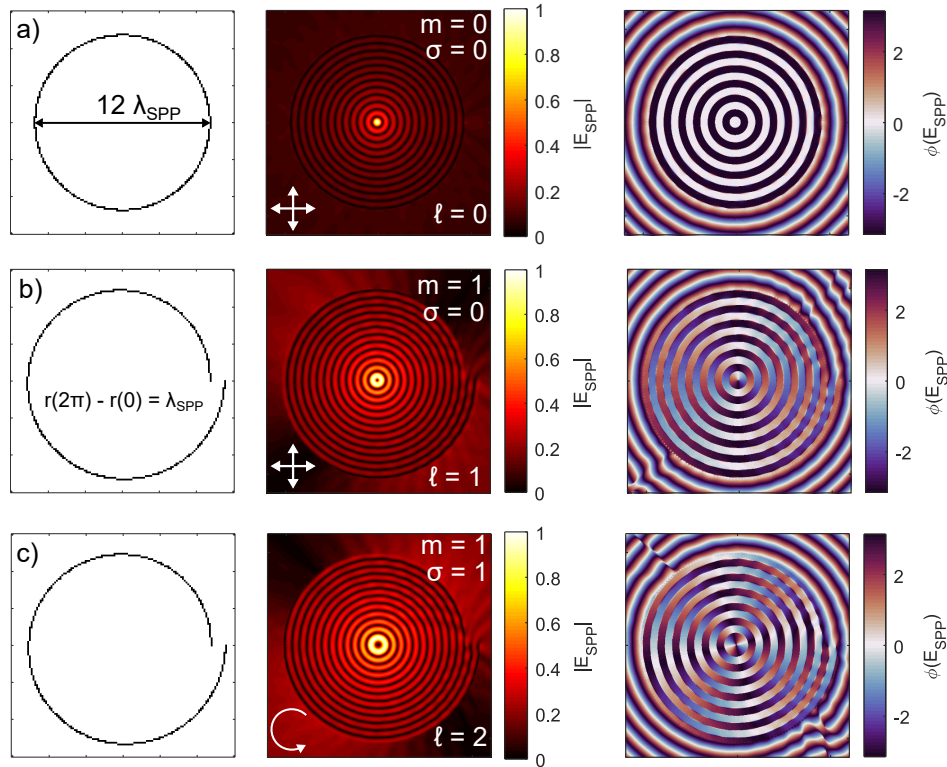

Figure 6.2: Amplitude and phase of the E_z SPP field at $\lambda = 800$ nm obtained through the Huygens principle with $N = 200$ dipoles. The position of the dipoles is shown by the black curves. a) Circular groove excited by radial polarization ($\sigma = 0$) yielding a SPP focus with $\ell = 0$. b) Circular groove excited by LCP ($\sigma = 1$) producing an optical vortex with $\ell = 1$. c) Archimedian spiral groove with $m = 1$ excited by LCP ($\sigma = 1$) producing an optical vortex with $\ell = 2$. Images size $12 \times 12 \ \mu m^2$

The generation of SPP vortex is based on interference of SPP launched by a circular or spiral pattern that can take the form of a groove or ridge in a metal film. In the most common case to ensure that SPPs are launched with the same intensity along the

pattern, incident fields with radial symmetry are employed. This property is for example shared by radially polarized, circularly polarized and OAM beams. In the case of a circular groove/ridge, if the radius $r = n\lambda_{SPP}$ is an integer multiple of the SPP wavelength, a focal spot in the center can be created by excitation with radially polarized light. The intense focal field in the center is obtained as all the SPPs interfere constructively at the center with the same phase. The SPP generation process can be simulated through the Huygens principle by positioning a number of dipoles in a circular pattern, as shown in Figure 6.2 a). The amplitude and phase simulate the E_z component of the SPP field produced by a circular groove with $n = 6$ for $\lambda = 800\,\mathrm{nm}$ on a gold surface with $\varepsilon = -25.0 + 1.2i$. The interference pattern is obtained by placing $N = 200$ dipoles equally spaced in the azimuthal direction. Each dipole located at $\mathbf{r_i}$ emits a field given by:

$$E_i = \frac{e^{i(\mathbf{k_{SPP}} \cdot (\mathbf{r} - \mathbf{r_i}) + \varphi)}}{\sqrt{(r - r_i)}} \tag{6.3}$$

where φ_i is an additional phase term. The total field is obtained by summing each contribution:

$$E = \sum_{i=1}^{N} E_i \tag{6.4}$$

For radial polarization all the dipoles emit in phase so that $\varphi_i = 0$ for all i. To produce an optical vortex from an input radial polarization an additional phase delay can be obtained by moving from a circular to a spiral groove. A 2π phase delay is obtained with an Archimedian spiral in which the radius increment over 2π is given by λ_{SPP}. The equation for such spiral is:

$$r(\theta) = \lambda_{SPP} \left(\frac{m\theta}{2\pi} + n \right) \tag{6.5}$$

with θ varying between 0 and 2π. The simulation with the dipoles arranged in this geometry is shown in Figure 6.2 b) for radial polarization. In this case a SPP vortex is generated, with the amplitude having the typical doughnut shape while the phase is characterized by a singularity in the center and a phase increment from 0 to 2π in the azimuthal direction. The topological charge of the vortex is therefore $\ell = 1$. The effect of left circularly polarized (LCP) light on such a structure is shown in Figure 6.2 c). To simulate the effect of LCP excitation each dipole emits with a phase equal to its angular coordinate $\varphi_i = \theta_i$. In this case the geometrical phase delay determined by the structure is summed with the phase delay determined by the LCP light, producing a SPP vortex with topological order $\ell = 2$. The total angular momentum of the SPP vortex can be expressed as:

$$\ell = m + \sigma \tag{6.6}$$

where m indicates the geometrical order of the groove/slit used to launch SPP, and σ the topological order of the exciting beam. For LCP and right circularly polarized (RCP)

light $\sigma = \pm 1$ respectively, and higher values are obtained by high order OAM beams. The convention is that counter-clockwise vortexes have a $+$ charge, while clockwise vortexes have a $-$ sign. To give an example, excitation of the structure in Figure 6.2 c) with RCP light would yield a SPP focus as in Figure 6.2 a) as $m = 1$ and $\sigma = -1$. In the following we restrict to the case of circularly polarized excitation so that $\sigma = \pm 1$.
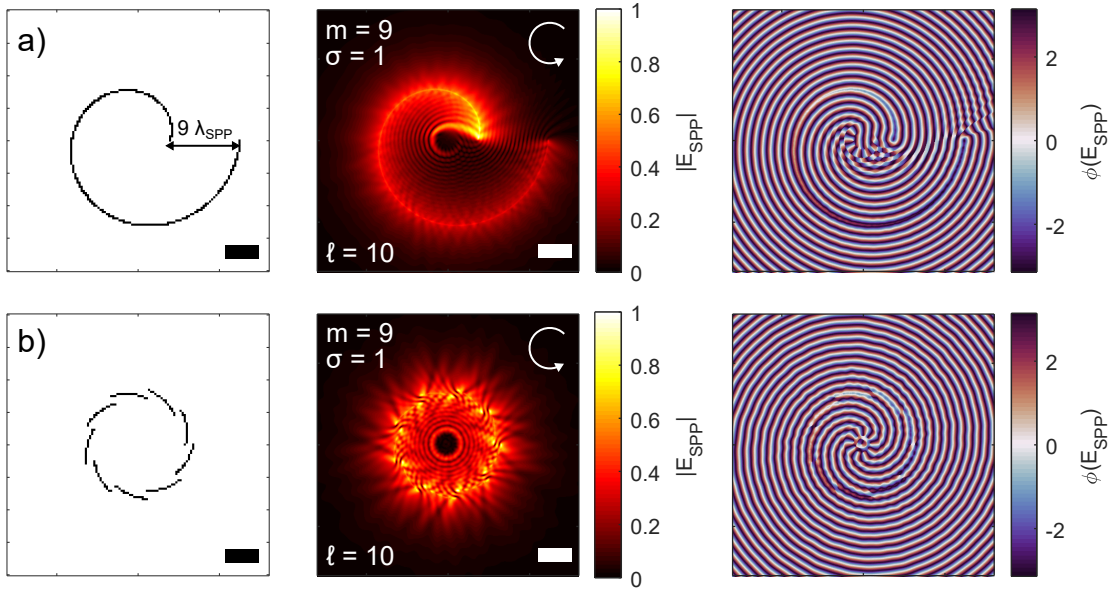

Figure 6.3: a) SPP interference pattern for a spiral $m = 9$ at $\lambda = 530\,\text{nm}$. The vortex pattern is distorted by SPP damping. b) The correct SPP vortex can be obtained by employing the corresponding vortex generator. Scale bar: 2 μm

According to eq. 6.6 to obtain vortex with higher topological charge, m can be increased. This corresponds to increasing the distance between the initial and final points of the spiral by multiples of λ_{SPP}. However this approach can introduce strong distortions at high m due to losses as the distance traveled by the SPPs is substantially different. The SPP interference pattern for a spiral of order $m = 9$ and $n = 4$ is shown in Figure 6.3 a). The resulting vortex is expected to have a topological charge $\ell = 10$ since we use LCP excitation. To highlight the effect of losses the field is evaluated in this case at $\lambda = 530\,\text{nm}$ where $\varepsilon = -4.7 + 1.9i$. The position of the dipoles is shown as black curves. In Figure 6.3 a) the vortex pattern is clearly distorted due to azimuthal losses. To solve this problem, so called vortex generators have been proposed, which are described by the following equation [151]:

$$r(\theta) = \lambda_{SPP}\left(\frac{\text{mod}(m\theta, 2\pi)}{2\pi} + n\right) \tag{6.7}$$

where $\text{mod}(m\theta, 2\pi)$ indicates the remainder of the division of $m\theta$ by 2π. In the vortex generator, instead of having a single discontinuity in the groove with $\Delta = 9\lambda_{SPP}$, 9 discontinuities with $\Delta = \lambda_{SPP}$ are realized. The resulting SPP pattern is shown in Figure

6.3 b) for $m = 9$ and $n = 6$. Since the SPP traveling distance is similar for all azimuthal coordinates, the correct vortex pattern is obtained.
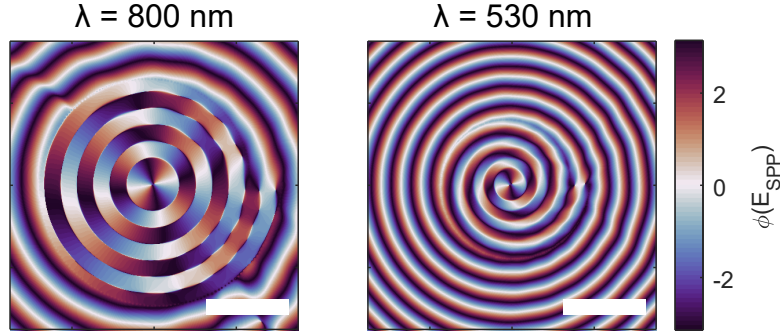

Figure 6.4: Phase profile of an SPP vortex with $\ell = 2$. On top of the shrinking of the SPP wavelength at $530\,\text{nm}$, the phase profile has a different behaviour due to increased confinement and losses of the SPP. Scale bar: $2\,\mu\text{m}$

By comparing the SPP vortex in Figures 6.2 and 6.3 an interesting difference can be seen in the phase profile. This difference can be highlighted by simulating the same vortex with $\ell = 2$ at $\lambda = 800\,\text{nm}$ and $\lambda = 530\,\text{nm}$ as shown in Figure 6.4. While the vortex at $\lambda = 530\,\text{nm}$ is characterized by a spiral phase pattern, the one at $\lambda = 800\,\text{nm}$ closely resembles the one of a LG beam of order $\ell = 2$ [157]. The difference in the phase profiles in Figure 6.4 is related to the losses of the SPP and their confinement with respect to the light line. While the vortex at $\lambda = 800\,\text{nm}$ is characterized by low confinement and low losses, at $\lambda = 530\,\text{nm}$ the SPP dispersion is appreciably on the right of the light line. Then, while for $\lambda = 800\,\text{nm}$ the vortex profile is similar to the one of a free-space propagating beam described by one of the LG modes as shown in Figure 6.1, this is not the case for $\lambda = 530\,\text{nm}$. This has a consequence for the quantitative evaluation of the mode purity of an optical vortex, which is checked by integrating the field profile $U(r, \theta)$ against the reference LG functions [158, 159]:

$$A_{\ell,\ell',p} = \frac{|\iint LG_{\ell,p} \cdot U^* \, dr \, d\theta|^2}{|\iint LG_{\ell,p} \cdot LG^*_{\ell',p} \, dr \, d\theta|^2} \tag{6.8}$$

In practice often the integral overlap is not done directly with the LG beams, but with their interference with a plane wave, which is how free-space OAM beams are usually detected [143]. Overall, this observation indicates that to quantify the OAM purity of an optical vortex originating from highly confined SPP, LG modes cannot be used as a reference, but an alternative set of functions have to be used.

6.3   Surface phonon polariton vortex

The principles introduced in the previous sections also apply to the generation of vortex with mid-IR SPhPs. While SPP vortex have been extensively studied, SPhP vortex are

still to be fully explored. Recently, hyperbolic phonon-polaritons (HPhP) vortex have been mapped through s-SNOM in hBN films [160, 161]. However, in both these works the HPhP field was measured employing conventional reflection-mode sSNOM, which is not suited to map complex optical fields. Due to the mechanism introduced in chapter 5, the measured edge-launched fringes periodicity is not the same along all directions due to the different angle φ between the exciting wavefront and the edge [39]. This inevitably distorts the resulting HPhP field. This issue can be solved by employing transmission sSNOM, where light is coupled from a parabolic mirror positioned below the sample, and light scattered by the tip is sent to the parabolic mirror employed for reflection measurements [162, 163]. As the light is focused from below at normal incidence, the distortion of the fringes periodicity due to the orientation between the launching edge and the exciting wavefront is eliminated. This scheme has been employed to correctly map the field distribution resulting from SPP interference producing two-dimensional vortex and skyrmions [153, 154, 164, 165]. Moreover, as the polarization is perpendicular to the tip shaft, tip-launched SPhP and coupling between tip and resonant structures are minimized in this configuration [162, 166].
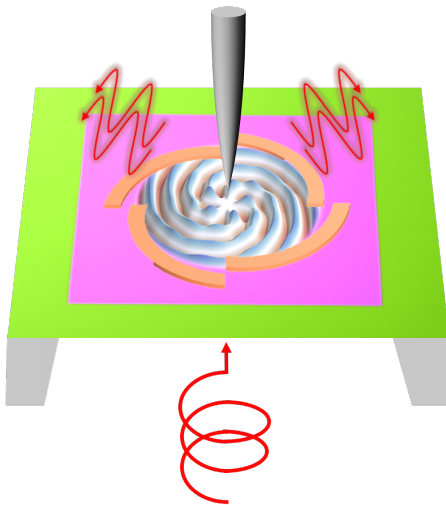

Figure 6.5: Sketch of the near-field transmission measurementd to map SPhP vortex. Chromium ridges are fabricated on top of a suspended SiC membrane to generate SPhP vortex. The structure is excited from a circularly polarized beam incident from below.

Here we map SPhP vortex in suspended $100 \, \mathrm{nm}$ SiC thin-films supporting highly confined SPhPs described in chapter 5. The small thickness of the SiC membranes allows us to measure in transmission, eliminating the artifacts discussed above. Phase and amplitude are obtained using the PsHet method, and the signal is demodulated at the second order $n = 2$. The vortex are created by launching SPhPs from Chromium (Cr) ridges fabricated with conventional electron beam lithography on top of the SiC membrane as sketched in Figure 6.5. The shape of the Cr ridges is chosen according to eq. 6.7 describing the shape of the vortex generator. The wavelength of the SPhPs is calculated according to eq. 5.4. The laser source is the same employed in chapter 5, where the beam bandwidth is

reduced with a monochromator as it was done for the experiments shown in Figure 5.8. A quarter-waveplate is used to produce RCP and LCP excitation.
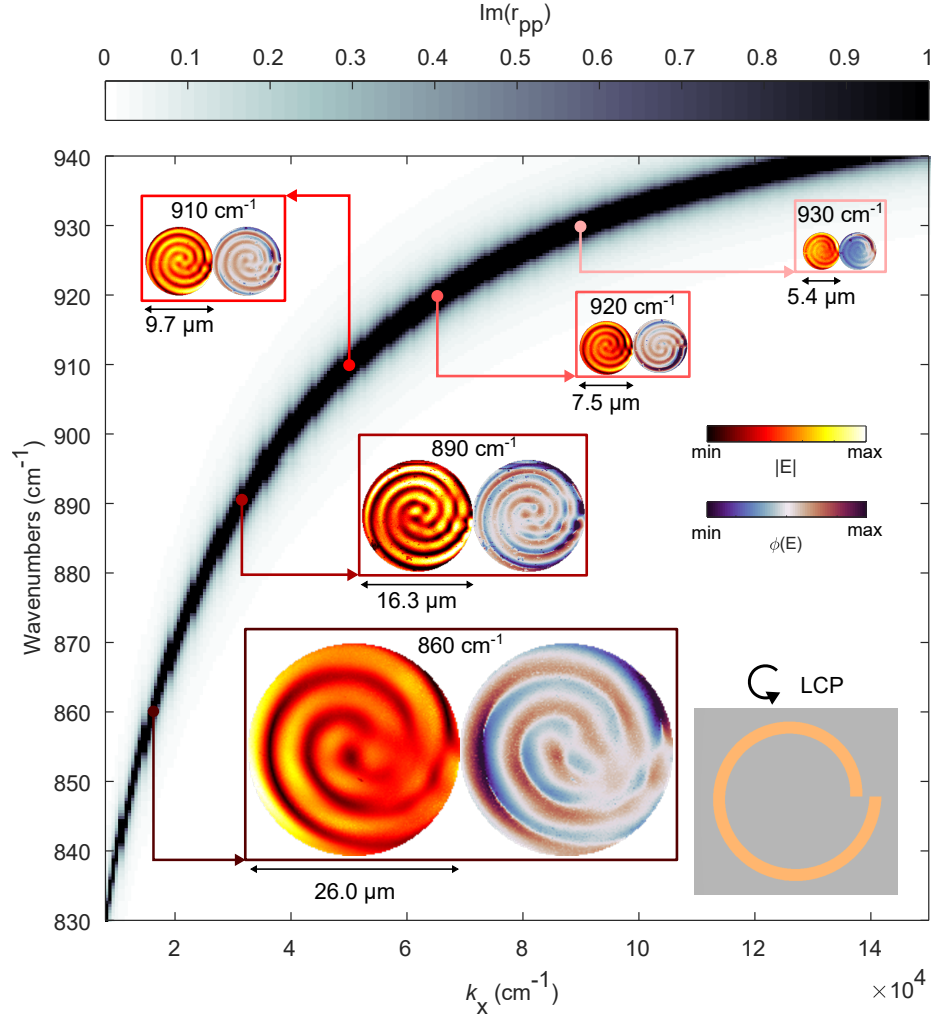

Figure 6.6: Near-field amplitude and phase maps obtained at different frequencies in the SiC RS band for vortex with $\ell = 2$. The SPhP dispersion calculated through the transfer-matrix method is shown in the background. A sketch of the Cr ridge and polarization handedness is shown in the bottom-right corner. Due to the strong SPhP dispersion, a small change in the excitation wavelength (from $11.6\,\mu m$ to $10.7\,\mu m$) can shrink the vortex size 5 times.

A difference between SPP and SPhP is that for the latter the dispersion is much stronger, and the polariton wavelength strongly changes in a narrow wavelength range. This means that by slightly tuning the excitation wavelength, vortex of very different sizes can be obtained. This effect is shown in Figure 6.6 for vortexes with $\ell = 2$ obtained by excitation of SPhP on the SiC membrane. The launching ridge is a single Cr spiral with $m = 1$ and the sample is excited with LCP light, as shown in the inset in the bottom right

corner. The experimentally obtained amplitude and phase maps are reported for a set of wavelengths spanning the RS band. The maps show spiral patterns with 2 arms, confirming the vortex topological order $\ell = 2$. In the background the SPhP dispersion of the thin-film odd mode (see chapter 5 for mode details) calculated through the transfer-matrix method is reported. The maps are scaled to their real spacial size to easily visualize how much the vortex footprint shrinks when moving from $\omega = 860\,\mathrm{cm}^{-1}$ to $\omega = 930\,\mathrm{cm}^{-1}$. An $\approx 8\%$ reduction in the excitation wavelength results in an $\approx 80\%$ reduction of the vortex size. The smallest vortex measured has a confinement of $\lambda_{SPhP}/\lambda_0 \approx 15.5$, comparable to what has been achieved in hBN films [161].
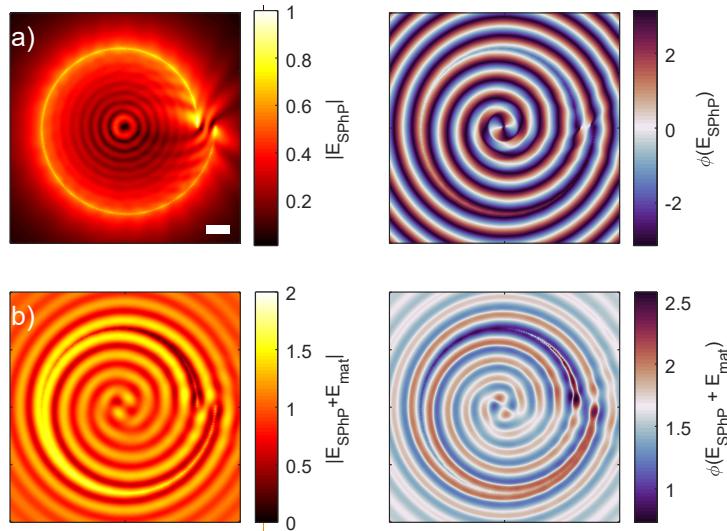

Figure 6.7: The field profiles measured by sSNOM are affected by the bare-material signal coming from the SiC film. a) Simulation of a SPhP vortex with $\ell = 2$ at $900\,\mathrm{cm}^{-1}$. b) Adding a background field representing the bare material response modifies the simulated optical vortex profile. Scale bar: 1 μm.

By comparing the experimental near-field maps in Figure 6.6 to the theoretical calculation in Figure 6.2 c), one can see that there are clear differences. In the experimental data both amplitude and phase show a spiral behavior. While we have seen that a spiraling phase is associated with strong SPhP confinement as shown in Figure 6.6, we expect nevertheless a doughnut distribution of the field amplitude. The discrepancy between experimental data and theoretical predictions can be understood by considering the contribution coming from the bare material response [100], which is position independent but must be considered when comparing with the theoretical predictions. The sSNOM signal can be written as:

$$
\begin{aligned}
A_{exp}(r,\theta) &= |E_{SPhP}(r,\theta) + E_{mat}| \\
\phi_{exp}(r,\theta) &= \phi(E_{SPhP}(r,\theta) + E_{mat})
\end{aligned}
\tag{6.9}
$$

where $A_{exp}(r, \theta)$ and $\phi_{exp}(r, \theta)$ are the amplitude and phase signals obtained experimentally. Since both the amplitude and phase computations are not linear operations, the presence of the background field is not simply summed in the experimental maps. The effect of a constant background field is shown in Figure 6.7 for a $\ell = 2$ vortex. In Figure 6.7 a) the pure SPhP profile calculated through the Huygens principle is shown at $\omega = 900 \, \text{cm}^{-1}$. The dielectric function used for SiC is the same as in chapter 5 (following eq. 1.5), except we use here a higher dissipation term of $\gamma = 6.6 \, \text{cm}^{-1}$, which better reproduces the experimental results. The absolute value of the SPhP field is normalized to 1, and the additional background field added has the value $E_{mat} = 1e^{i\pi/2}$. This field acts in such a way that both the amplitude and phase have a spiral pattern as shown in Figure 6.7 b), reproducing well the experimental data shown in Figure 6.6.
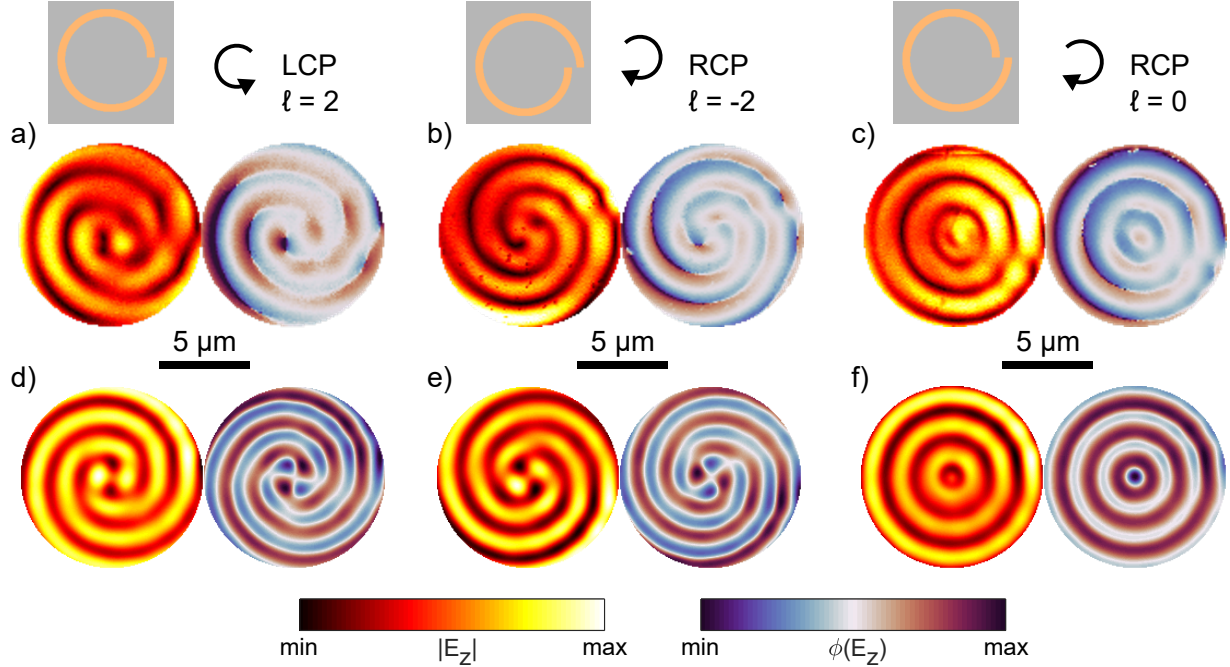

Figure 6.8: Near field mapping of SPhP vortex at $900 \, \text{cm}^{-1}$ and corresponding simulations for a, d) $\ell = 2$, b, e) $\ell = -2$ and c, f) $\ell = 0$. The launching ridge structure and polarization handedness are sketched at the top for each vortex.

The topological order of the vortex can be controlled by the geometrical shape of the Cr ridge and the polarization handedness according to eq. 6.6. In Figure 6.8 we show experiments and simulations at $\omega = 900 \, \text{cm}^{-1}$ at which $\lambda_{SPhP} = 1.58 \, \mu\text{m}$. The value of the topological charge can be inverted by flipping the handedness of both the spiral pattern and the polarization handedness as shown in Figure 6.8 a, b) where we map vortex with $\ell = 2$ and $\ell = -2$ respectively. Corresponding simulations are shown in Figure 6.8 d, e) By having opposite handedness of the Cr ridge $m = 1$ and polarization $\sigma = -1$ a SPhP focus can be realized, as shown in the experimental and simulated maps of Figure 6.8 c, f).
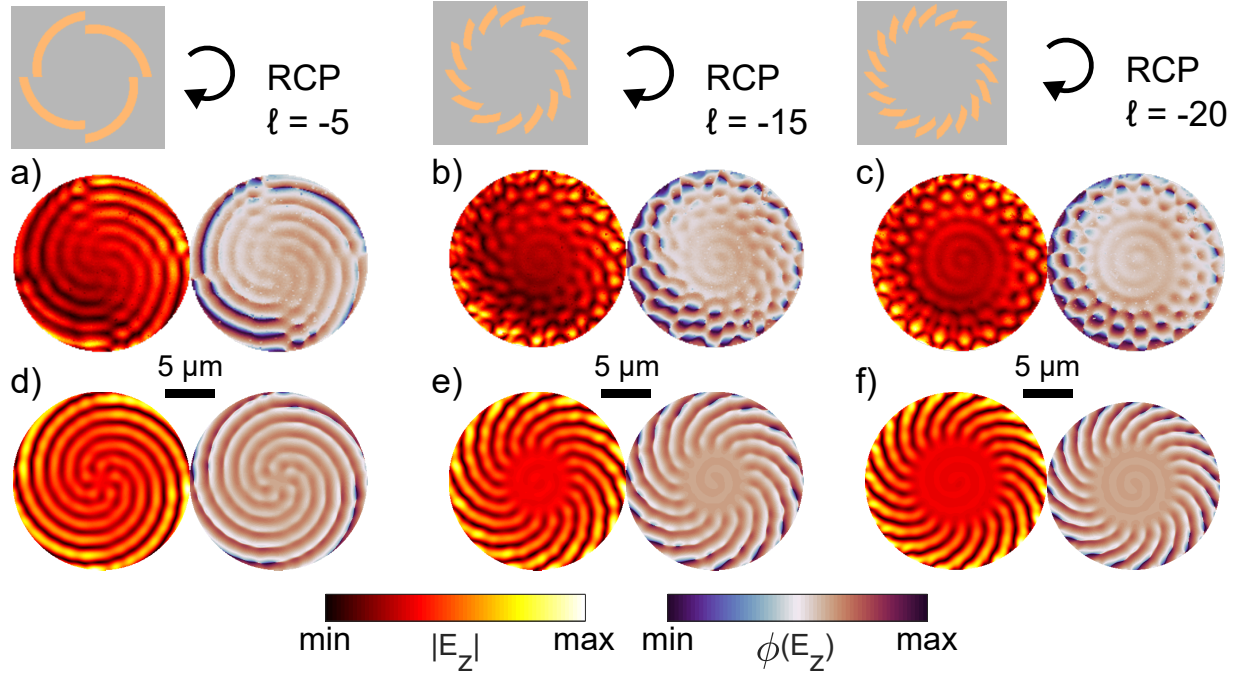
Figure 6.9: Near field mapping of SPhP vortex at $900\,\mathrm{cm}^{-1}$ and corresponding simulations for a, d) $\ell = -5$, b, e) $\ell = -15$ and c, f) $\ell = -20$. The launching ridge structure and polarization handedness are sketched at the top for each vortex.

Thanks to the artifact-free measurements and low losses of the SPhP in the suspended SiC membranes, we are able to map SPhP vortex with high topological orders. In Figure 6.9 a-c) we report maps of vortex with $\ell = -5$, $\ell = -15$ and $\ell = -20$. The corresponding simulations are shown in Figure 6.9 d-f). The background material field is chosen to better fit the simulations to the experimental data. To the best of our knowledge, $\ell = -20$ is the highest topological order ever measured in the near-field for 2-dimensional optical vortexes [150, 151, 154, 161]. As the maximum order of the topological order is related to the number of information channels that can be used for multiplexing, this result is an important step for realization of on-chip generation and detection of OAM states.

As the signal coming from the bare material contribution is position-independent, FFT filtering can be used to remove its contribution. The absolute value of the complex FFT map for the $\ell = -2$ vortex reported in Figure 6.8 b) is shown in Figure 6.10 a). The intense spot at the center comes from the position-independent material response. The pure vortex field can be obtained by filtering the FFT map and retaining only a ring around the predicted SPhP wavevector as shown in Figure 6.10 b). In this way not only the material response is eliminated, but also any defect due to dirt on the sample is removed by filtering high-k vector components. The SPhP field can be recovered by inverse FFT of the complex filtered map in Figure 6.10 b), as shown in Figure 6.10 c). Excellent agreement is obtained with the simulated $\ell = -2$ vortex field in Figure 6.10 d) obtained with no additional background field. The same procedure can be applied to the high order
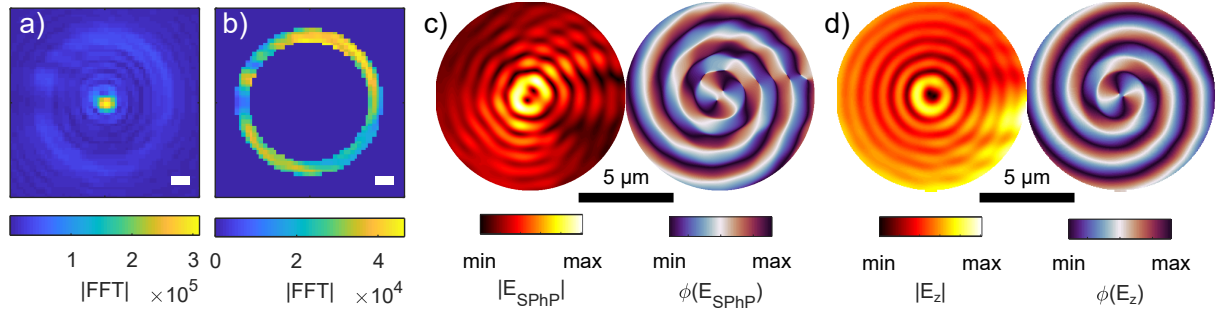
Figure 6.10: a,b) Removal of the position-independent material response through filtering of the FFT maps, where only a ring around the theoretical SPhP wavevector is retained. The absolute value of the FFT is shown. The FFT maps are obtained from the data reported in Figure 6.8 b) at $\omega = 900\,\mathrm{cm}^{-1}$. Scale bar $2k_x/k_0$. c) Amplitude and phase SPhP vortex maps recovered from inverse FFT of b). The retrieved field shows excellent agreement with the corresponding simulation reported in d).

vortex shown in Figure 6.9. We consider the $\ell = -15$ and $\ell = -20$ vortex and show the filtered experimental maps in Figure 6.11 a), c). The corresponding simulated amplitude and phase maps are shown in Figure 6.11 b), d). While the experimental phase profiles show great agreement with the theoretical maps, the experimental amplitude shows higher intensity at the center compared to what predicted from simulations. Further analysis should be carried to understand this discrepancy, possibly due to a non-complete removal of the bare material contribution.

6.4   Conclusions

In summary, we presented in this chapter the amplitude and phase near-field mapping of SPhP vortexes in suspended SiC thin films. The transmission sSNOM setup allows reduction of artifacts arising from tilted illumination which were present in previous works on near-field mapping of optical vortex in hBN films [161]. We analyzed the influence of the bare material response on the vortex mapping, aloowing us to accurately reproduce the experimental results through simulations based on the simple Huygens principle. We also show that the pure SPhP vortex response can be recovered by FFT filtering of the experimental data. We report, to the best of our knowledge, the highest topological order $\ell = -20$ ever recorded by near-field mapping of two-dimensional optical vortex.
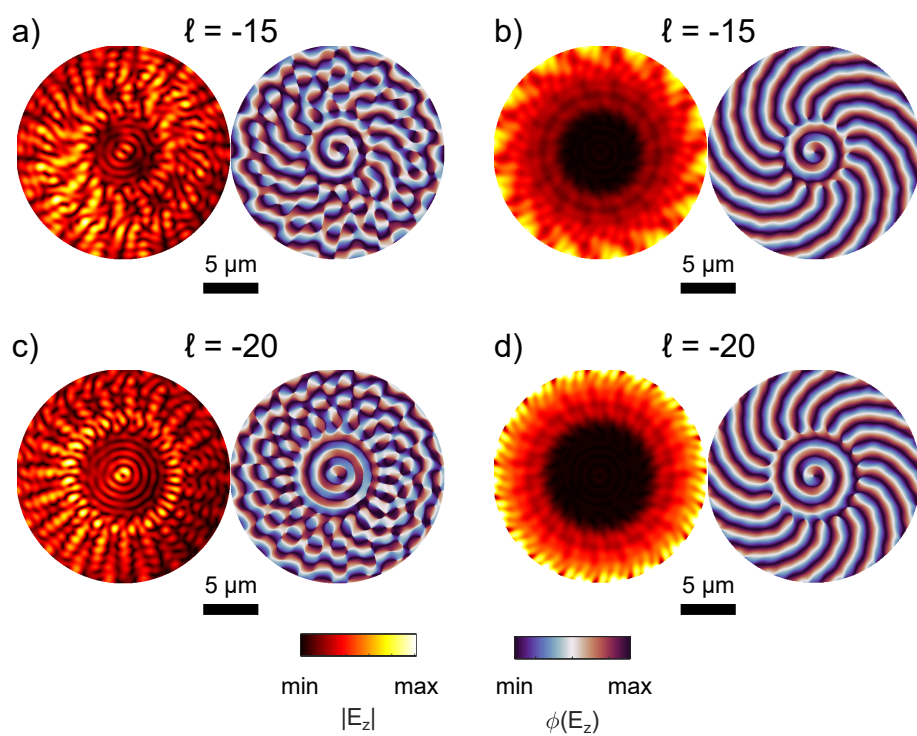
Figure 6.11: SPhP vortex field retrieved from FFT filtering at $\omega = 900\,\mathrm{cm}^{-1}$ for $\ell = -15$ a) and $\ell = -20$ c). Corresponding simulations shown in panels b), d).

Chapter 7

Conclusions and Outlooks

This work investigates various silicon carbide (SiC) nanostructures exhibiting subwavelength field confinement through the excitation of surface phonon polaritons (SPhP). SiC resonators support long-lived resonances owing to low phonon-polariton intrinsic losses.

Chapter 4 introduces a metasurface made of cylindrical pillars supporting various high quality factor resonances, which is probed both through far-field and near-field spectroscopy. For the near-field measurements a scattering-scanning near-field microscope (sSNOM) is employed throughout this thesis. In sSNOM a laser source is focused at the apex of an AFM tip and the backscattered light is collected, resulting in subwavelength spatial resolution. We provide an in-depth investigation of how the presence of the metallic AFM tip modifies the optical response of the metasurface. The excitation of a dark-mode through the near-field interaction with the tip is observed in the experimental result. This new mode could be in the future further investigated by coupling the metasurface to different mid-IR resonators or emitters for sensing [167], engineered thermal emission [78, 168] or higher harmonic generation [80, 85].

All SiC structures up to now have been fabricated through a combination of electron beam lithography and reactive-ion etching. More freedom in the design of the optical response could be achieved by employing three-dimensional laser printed polymer structures [169] as a soft mask with an etching rate comparable to the one of SiC. In this way height modulation of the SiC resonators could be achieved.

Chapter 5 investigates through sSNOM highly confined SPhPs in suspended SiC membranes with lifetimes comparable to what has been reported in various two-dimensional materials [45, 140]. As SiC membranes are commercially available with millimeter lateral sizes, these present a viable alternative to vdW films for large-scale confined SPhP applications. As the SiC Reststrahlen band partially overlaps with the one of the in-plane anisotropic $\alpha - MoO_3$, coupling of the SPhPs of the two materials might lead to the generation of novel hybridized modes [170]. For future works, inverse resonators could be fabricated by etching the SiC suspended films. Moreover, SiC membranes could be employed in a number of thermal applications, as it has been shown that SPhPs modify the thermal conductivity of polar dielectrics [120, 121, 122]. As a further step, pattering of the films surface could be implemented to achieve routing of thermal diffusion [124].

In the last chapter, the films studied in chapter 5 are employed to generate highly confined SPhP vortex. The topological order of the designed vortex is confirmed by mapping the corresponding near-field distribution through sSNOM. Investigation of the effect of the highly dispersive SPhP wavelength on the vortex topological order will be a future step to unlock the full potential of SPhP-based vortex [161]. A quantitative evaluation of the quality of the produced vortex would also be a future step to better evaluate the performance of the SiC membranes for optical vortex generation [159]. On-chip detection of mid-infrared OAM beams could be implemented through the demonstrated highly confined SPhP [141]. More complex SPhP optical states such as skyrmions could be similarly realized and mapped in the SiC membranes [164].

Appendix A

Supplementary Information

Point spread function and focal field equations

The plots shown in Figure 1.1 are calculated in the so called paraxial approximation. In the this approximation the field is assumed to have components only orthogonal to the propagation direction z. This assumption is valid for free-space propagating and weakly focused beams. In this case the transverse components of the wavevector are assumed to be small so that the following expansion can be used [1]:

$$k_z = k\sqrt{1 - \frac{k_x^2 + k_y^2}{k^2}} \approx k - \frac{k_x^2 + k_y^2}{2k} \tag{A.1}$$

In this approximation the point-spread function in the image plane for a dipole oriented along the x-axis is [1]:

$$|\mathbf{E}(x, y, z = 0)|^2 \propto \frac{\mathrm{NA}^4}{\lambda^6 M^2} \left[2\frac{J_1(2\pi\tilde{\rho})}{2\pi\tilde{\rho}} \right]^2 \tag{A.2}$$

where $\rho^2 = x^2 + y^2$ and $\tilde{\rho} = NA\rho/M\lambda$. M is here the magnification of the optical apparatus. J_1 is the Bessel function of the first kind of order 1. In Figure 1.1 the PSF is evaluated for $M = 1$.

In the paraxial approximation the field of a weakly focused Gaussian beam has the following expression [1]:

$$E(\rho, z) = \mathbf{E_0} \frac{\omega_0}{\omega(z)} e^{\frac{-\rho^2}{\omega^2(z)}} e^{i[kz - \eta(z) + k\rho^2/2R(z)]} \tag{A.3}$$

where:

$$\begin{aligned} \omega(z) &= \omega_0 (1 + z^2/z_0^2)^{1/2} \\ R(z) &= z(1 + z_0^2/z^2) \\ \eta(z) &= \arctan(z/z_0) \end{aligned} \tag{A.4}$$

and $z_0 = k\omega_0^2/2$. The focusing angle θ is related to the other quantities as $\theta = 2/k\omega_0$. In Figure 1.1 the fields are evaluated at $z = 10\,\text{nm}$ for $\lambda = 500\,\text{nm}$.

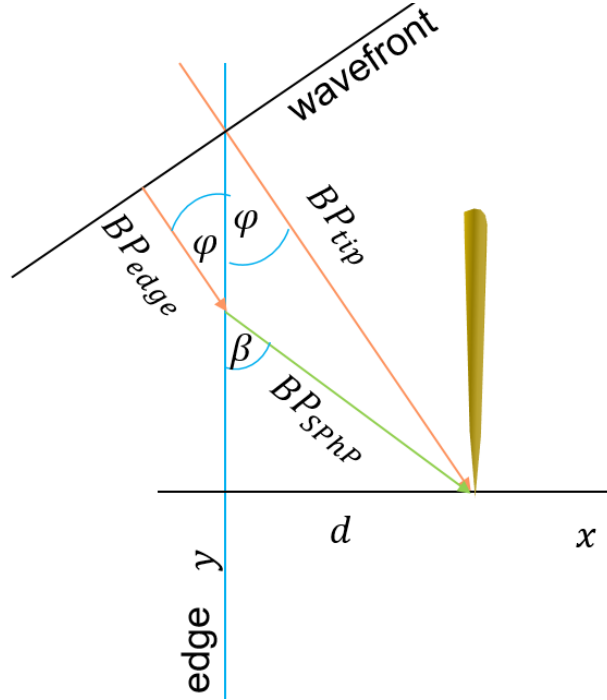# Derivation of fringes spacing in sSNOM polariton interferometry

Figure A.1: 2D sketch for the derivation of the phase accumulated along the different optical paths travelled during polariton excitation, propagation and scattering.

The periodicity of the sSNOM measured fringes depends on the phase accumulate between the directly back-scattered light from the tip and the polariton pathway [39, 131]. The fringes periodicity is related to the accumulated phase by $\Lambda = 2\pi\Delta\phi/d$, where d is the edge-tip distance. The derivation of the position-dependent accumulated phase is easier in 2D, and the generalization in 3D is straightforward. In Figure A.1 a sketch of the 2D geometry of the problem is reported. Here φ is the angle between the incident light k-vector and the edge launching the polaritons. β is the polariton propagation angle with respect to the edge and is determined by conservation of momentum along the edge direction y:

$$\beta_{2D} = \arccos\left(\frac{\cos\varphi}{n}\right) \tag{A.5}$$

Where $n = \lambda_0/\lambda_{SPhP}$. To evaluate the total phase accumulation, we have to describe the phase delay in the three relevant optical pathways: from the plane wave wavefront to

the tip BP_{tip}, from the wavefront to the edge BP_{edge} and from the edge to the tip BP_{SPhP}. From simple geometrical considerations (and remembering that in BP_{SPhP} the wavevector is not the free-space one but the polariton wavevector) the phase accumulated along these three paths is:

$$\begin{cases} |BP_{edge}|_{2D} & = k_0 d \left(\frac{1}{\tan \varphi} - \frac{1}{\tan \beta} \right) \cos \varphi \\ |BP_{tip}|_{2D} & = k_0 \frac{d}{\sin \varphi} \\ |BP_{SPhP}|_{2D} & = k_0 n \frac{d}{\sin \beta} \end{cases} \tag{A.6}$$

The only difference in the 3D case is that $|BP_{edge}|$ and $|BP_{tip}|$ have to be projected in the $x - y$ plane and that the momentum conservation along y is also modified accordingly:

$$\beta_{3D} = \arccos \left(\frac{\cos \varphi \sin \theta}{n} \right) \tag{A.7}$$

$$\begin{cases} |BP_{edge}|_{3D} & = k_0 d \left(\frac{1}{\tan \varphi} - \frac{1}{\tan \beta} \right) \cos \varphi \sin \theta \\ |BP_{tip}|_{3D} & = k_0 \frac{d}{\sin \varphi} \sin \theta \\ |BP_{SPhP}|_{3D} & = k_0 n \frac{d}{\sin \beta} \end{cases} \tag{A.8}$$

For the edge launched polaritons the phase accumulated by the polariton optical path with respect to the light directly backscattered by the tip is:

$$\Delta\varphi_{el} = |BP_{edge}| + |BP_{SPhP}| - |BP_{tip}| =$$
$$= k_0 d \left(- \sin \varphi \sin \theta - \sqrt{n^2 - \sin^2 \theta + \sin^2 \theta \sin^2 \varphi} \right) \tag{A.9}$$

The corresponding fringes spacing $\Lambda = 2\pi \Delta\phi / d$ is therefore:

$$\Lambda_{el} = \frac{\lambda_0}{- \sin \varphi \sin \theta - \sqrt{n^2 + \sin^2 \theta (\sin^2 \varphi - 1)}} \tag{A.10}$$

For the edge-launched tip-reflected edge-scattered polaritons the accumulated phase is $\Delta\phi_{ete} = 2|BP_{edge}| + 2|BP_{SPhP}| - 2|BP_{tip}| = 2\Delta\phi_{el}$, and therefore the fringes spacing $\Lambda_{ete} = \Lambda_{el}/2$. For the edge-launched tip-reflected tip-scattered contribution the accumulated phase is $\Delta\phi_{etet} = |BP_{edge}| + |BP_{SPhP}| - |BP_{tip}| + 2dnk_0$, where the last term corresponds to the phase accumulated by the polariton when going from the tip to the edge and back to the tip (this is the bare tip-launched contribution). The fringes spacing is then $\Lambda_{etet} = \lambda_0 \left(1/\Lambda_{el} + 1/\Lambda_{tl} \right)$. The predicted dispersion curves for all these processes are simply obtained by $k = 2\pi/\Lambda$.

Appendix B

Publisher permission

CCC

RightsLink

Home   Help ⌄   Email Support   Sign in   Create Account

Near-Field Spectroscopy of Cylindrical Phonon-Polariton
Antennas

ACS Publications
Most Trusted. Most Cited. Most Read.

Author: Andrea Mancini, Christopher R. Gubbin, Rodrigo Berté, et al

Publication: ACS Nano

Publisher: American Chemical Society

Date: Jul 1, 2020

Copyright © 2020, American Chemical Society

CCC
RightsLink

Home   Help   Email Support   Sign in   Create Account

Near-Field Retrieval of the Surface Phonon Polariton Dispersion in Free-Standing Silicon Carbide Thin Films

Author: Andrea Mancini, Lin Nan, Fedja J. Wendisch, et al

Publication: ACS Photonics

Publisher: American Chemical Society

Date: Nov 1, 2022

Copyright © 2022, American Chemical Society

PERMISSION/LICENSE IS GRANTED FOR YOUR ORDER AT NO CHARGE

This type of permission/license, instead of the standard Terms and Conditions, is sent to you because no fee is being charged for your order. Please note the following:

- Permission is granted for your request in both print and electronic formats, and translations.
- If figures and/or tables were requested, they may be adapted or used in part.
- Please print this page for your records and send a copy of it to your publisher/graduate school.
- Appropriate credit for the requested material should be given as follows: "Reprinted (adapted) with permission from {COMPLETE REFERENCE CITATION}. Copyright {YEAR} American Chemical Society." Insert appropriate information in place of the capitalized words.
- One-time permission is granted only for the use specified in your RightsLink request. No additional uses are granted (such as derivative works or other editions). For any uses, please submit a new request.

If credit is given to another source for the material you requested from RightsLink, permission must be obtained from that source.

BACK   CLOSE WINDOW

Bibliography

[1] L. Novotny and B. Hecht, *Principles of nano-optics*. Cambridge university press, 2012.

[2] J. I. Goldstein, D. E. Newbury, J. R. Michael, N. W. Ritchie, J. H. J. Scott, and D. C. Joy, *Scanning electron microscopy and X-ray microanalysis*. Springer, 2017.

[3] I. Utke, P. Hoffmann, and J. Melngailis, "Gas-assisted focused electron beam and ion beam processing and fabrication," *Journal of Vacuum Science & Technology B: Microelectronics and Nanometer Structures Processing, Measurement, and Phenomena*, vol. 26, no. 4, pp. 1197–1276, 2008.

[4] G. Hlawacek, V. Veligura, R. van Gastel, and B. Poelsema, "Helium ion microscopy," *Journal of Vacuum Science & Technology B, Nanotechnology and Microelectronics: Materials, Processing, Measurement, and Phenomena*, vol. 32, no. 2, p. 020801, 2014.

[5] B. H. Bransden and C. J. Joachain, *Physics of atoms and molecules*. Pearson Education India, 2003.

[6] N. W. Ashcroft and N. D. Mermin, *Solid state physics*. Cengage Learning, 2022.

[7] S. W. Hell, S. J. Sahl, M. Bates, X. Zhuang, R. Heintzmann, M. J. Booth, J. Bewersdorf, G. Shtengel, H. Hess, P. Tinnefeld, *et al.*, "The 2015 super-resolution microscopy roadmap," *Journal of Physics D: Applied Physics*, vol. 48, no. 44, p. 443001, 2015.

[8] R. J. Hermann and M. J. Gordon, "Nanoscale optical microscopy and spectroscopy using near-field probes," *Annual Review of Chemical and Biomolecular Engineering*, vol. 9, pp. 365–387, 2018.

[9] X. Chen, D. Hu, R. Mescall, G. You, D. Basov, Q. Dai, and M. Liu, "Modern scattering-type scanning near-field optical microscopy for advanced material research," *Advanced Materials*, vol. 31, no. 24, p. 1804774, 2019.

[10] R. Zia, J. A. Schuller, A. Chandran, and M. L. Brongersma, "Plasmonics: the next chip-scale technology," *Materials today*, vol. 9, no. 7-8, pp. 20–27, 2006.

[11] C. Sun, M. T. Wade, Y. Lee, J. S. Orcutt, L. Alloatti, M. S. Georgas, A. S. Waterman, J. M. Shainline, R. R. Avizienis, S. Lin, *et al.*, "Single-chip microprocessor that communicates directly using light," *Nature*, vol. 528, no. 7583, pp. 534–538, 2015.

[12] P. Biagioni, J.-S. Huang, and B. Hecht, "Nanoantennas for visible and infrared radiation," *Reports on Progress in Physics*, vol. 75, no. 2, p. 024402, 2012.

[13] J. Haas and B. Mizaikoff, "Advances in mid-infrared spectroscopy for chemical analysis," *Annual Review of Analytical Chemistry*, vol. 9, no. 1, pp. 45–68, 2016. PMID: 27070183.

[14] E. Le Ru and P. Etchegoin, *Principles of Surface-Enhanced Raman Spectroscopy: and related plasmonic effects.* Elsevier, 2008.

[15] S. A. Maier, *Plasmonics: fundamentals and applications.* Springer, 2007.

[16] P. R. West, S. Ishii, G. V. Naik, N. K. Emani, V. M. Shalaev, and A. Boltasseva, "Searching for better plasmonic materials," *Laser & photonics reviews*, vol. 4, no. 6, pp. 795–808, 2010.

[17] G. V. Naik, J. Kim, and A. Boltasseva, "Oxides and nitrides as alternative plasmonic materials in the optical range," *Optical materials express*, vol. 1, no. 6, pp. 1090–1099, 2011.

[18] G. V. Naik, V. M. Shalaev, and A. Boltasseva, "Alternative plasmonic materials: beyond gold and silver," *Advanced Materials*, vol. 25, no. 24, pp. 3264–3294, 2013.

[19] W.-P. Guo, R. Mishra, C.-W. Cheng, B.-H. Wu, L.-J. Chen, M.-T. Lin, and S. Gwo, "Titanium nitride epitaxial films as a plasmonic material platform: alternative to gold," *ACS Photonics*, vol. 6, no. 8, pp. 1848–1854, 2019.

[20] A. N. Grigorenko, M. Polini, and K. Novoselov, "Graphene plasmonics," *Nature photonics*, vol. 6, no. 11, pp. 749–758, 2012.

[21] T. Taliercio and P. Biagioni, "Semiconductor infrared plasmonics," *Nanophotonics*, vol. 8, no. 6, pp. 949–990, 2019.

[22] J. D. Caldwell, L. Lindsay, V. Giannini, I. Vurgaftman, T. L. Reinecke, S. A. Maier, and O. J. Glembocki, "Low-loss, infrared and terahertz nanophotonics using surface phonon polaritons," *Nanophotonics*, vol. 4, no. 1, pp. 44–68, 2015.

[23] M. Dressel and G. Grüner, *Electrodynamics of solids: optical properties of electrons in matter.* American Association of Physics Teachers, 2002.

[24] F. J. Garcia de Abajo, "Graphene plasmonics: challenges and opportunities," *Acs Photonics*, vol. 1, no. 3, pp. 135–152, 2014.

[25] T. Wang, Z. Gui, A. Janotti, C. Ni, and P. Karandikar, "Strong effect of electron-phonon interaction on the lattice thermal conductivity in 3c-sic," *Physical Review Materials*, vol. 1, no. 3, p. 034601, 2017.

[26] U. Monteverde, J. Pal, M. Migliorato, M. Missous, U. Bangert, R. Zan, R. Kashtiban, and D. Powell, "Under pressure: control of strain, phonons and bandgap opening in rippled graphene," *Carbon*, vol. 91, pp. 266–274, 2015.

[27] M. Fox, *Optical properties of solids*. American Association of Physics Teachers, 2002.

[28] C. Eddy Jr and D. Gaskill, "Silicon carbide as a platform for power electronics," *Science*, vol. 324, no. 5933, pp. 1398–1400, 2009.

[29] S. Castelletto, A. Peruzzo, C. Bonato, B. C. Johnson, M. Radulaski, H. Ou, F. Kaiser, and J. Wrachtrup, "Silicon carbide photonics bridging quantum technology," *ACS Photonics*, vol. 9, no. 5, pp. 1434–1457, 2022.

[30] A. V. Zayats and D. Richards, *Nano-optics and near-field optical microscopy*. Artech House, 2009.

[31] K. N. Fish, "Total internal reflection fluorescence (tirf) microscopy," *Current protocols in cytometry*, vol. 50, no. 1, pp. 12–18, 2009.

[32] W. X. Tang, H. C. Zhang, H. F. Ma, W. X. Jiang, and T. J. Cui, "Concept, theory, design, and applications of spoof surface plasmon polaritons at microwave frequencies," *Advanced Optical Materials*, vol. 7, no. 1, p. 1800421, 2019.

[33] D. Aurelio and M. Liscidini, "Electromagnetic field enhancement in bloch surface waves," *Physical Review B*, vol. 96, no. 4, p. 045308, 2017.

[34] J. B. Khurgin, "How to deal with the loss in plasmonics and metamaterials," *Nature nanotechnology*, vol. 10, no. 1, pp. 2–6, 2015.

[35] L. Novotny, "Effective wavelength scaling for optical antennas," *Physical review letters*, vol. 98, no. 26, p. 266802, 2007.

[36] K. L. Kelly, E. Coronado, L. L. Zhao, and G. C. Schatz, "The optical properties of metal nanoparticles: the influence of size, shape, and dielectric environment," *The Journal of Physical Chemistry B*, vol. 107, no. 3, pp. 668–677, 2003.

[37] J. B. Khurgin, "Relative merits of phononics vs. plasmonics: the energy balance approach," *Nanophotonics*, vol. 7, no. 1, pp. 305–316, 2018.

[38] M. A. Ordal, R. J. Bell, R. W. Alexander, L. L. Long, and M. R. Querry, "Optical properties of fourteen metals in the infrared and far infrared: Al, co, cu, au, fe, pb, mo, ni, pd, pt, ag, ti, v, and w.," *Applied optics*, vol. 24, no. 24, pp. 4493–4499, 1985.

[39] A. Mancini, L. Nan, F. J. Wendisch, R. Berté, H. Ren, E. Cortés, and S. A. Maier, "Near-field retrieval of the surface phonon polariton dispersion in free-standing silicon carbide thin films," *ACS Photonics*, 2022.

[40] M. S. Tame, K. McEnery, Ş. Özdemir, J. Lee, S. A. Maier, and M. Kim, "Quantum plasmonics," *Nature Physics*, vol. 9, no. 6, pp. 329–340, 2013.

[41] G. Hu, Q. Ou, G. Si, Y. Wu, J. Wu, Z. Dai, A. Krasnok, Y. Mazor, Q. Zhang, Q. Bao, *et al.*, "Topological polaritons and photonic magic angles in twisted α-moo3 bilayers," *Nature*, vol. 582, no. 7811, pp. 209–213, 2020.

[42] J. Sun, N. M. Litchinitser, and J. Zhou, "Indefinite by nature: from ultraviolet to terahertz," *Acs Photonics*, vol. 1, no. 4, pp. 293–303, 2014.

[43] C. Wang, S. Huang, Q. Xing, Y. Xie, C. Song, F. Wang, and H. Yan, "Van der waals thin films of wte2 for natural hyperbolic plasmonic surfaces," *Nature communications*, vol. 11, no. 1, pp. 1–9, 2020.

[44] S. Dai, Z. Fei, Q. Ma, A. Rodin, M. Wagner, A. McLeod, M. Liu, W. Gannett, W. Regan, K. Watanabe, *et al.*, "Tunable phonon polaritons in atomically thin van der waals crystals of boron nitride," *Science*, vol. 343, no. 6175, pp. 1125–1129, 2014.

[45] W. Ma, P. Alonso-González, S. Li, A. Y. Nikitin, J. Yuan, J. Martín-Sánchez, J. Taboada-Gutiérrez, I. Amenabar, P. Li, S. Vélez, *et al.*, "In-plane anisotropic and ultra-low-loss polaritons in a natural van der waals crystal," *Nature*, vol. 562, no. 7728, pp. 557–562, 2018.

[46] G. Álvarez-Pérez, T. G. Folland, I. Errea, J. Taboada-Gutiérrez, J. Duan, J. Martín-Sánchez, A. I. Tresguerres-Mata, J. R. Matson, A. Bylinkin, M. He, *et al.*, "Infrared permittivity of the biaxial van der waals semiconductor α-moo3 from near-and far-field correlative studies," *Advanced Materials*, vol. 32, no. 29, p. 1908176, 2020.

[47] J. Taboada-Gutiérrez, G. Álvarez-Pérez, J. Duan, W. Ma, K. Crowley, I. Prieto, A. Bylinkin, H. Volkova, K. Kimura, T. Kimura, *et al.*, "Broad spectral tuning of ultra-low-loss polaritons in a van der waals crystal by intercalation," *Nature materials*, vol. 19, no. 9, pp. 964–968, 2020.

[48] N. C. Passler, X. Ni, G. Hu, J. R. Matson, G. Carini, M. Wolf, M. Schubert, A. Alù, J. D. Caldwell, T. G. Folland, *et al.*, "Hyperbolic shear polaritons in low-symmetry crystals," *Nature*, vol. 602, no. 7898, pp. 595–600, 2022.

[49] G. Hu, W. Ma, D. Hu, J. Wu, C. Zheng, K. Liu, X. Zhang, X. Ni, J. Chen, X. Zhang, *et al.*, "Real-space nanoimaging of hyperbolic shear polaritons in a monoclinic crystal," *Nature Nanotechnology*, pp. 1–7, 2022.

[50] M. Born and E. Wolf, *Principles of optics: electromagnetic theory of propagation, interference and diffraction of light.* Elsevier, 2013.

[51] N. C. Passler and A. Paarmann, "Generalized 4× 4 matrix formalism for light propagation in anisotropic stratified media: study of surface phonon polaritons in polar dielectric heterostructures," *JOSA B*, vol. 34, no. 10, pp. 2128–2139, 2017.

[52] G. Álvarez-Pérez, K. V. Voronin, V. S. Volkov, P. Alonso-González, and A. Y. Nikitin, "Analytical approximations for the dispersion of electromagnetic modes in slabs of biaxial crystals," *Physical Review B*, vol. 100, no. 23, p. 235408, 2019.

[53] Q. Zhang, Q. Ou, G. Si, G. Hu, S. Dong, Y. Chen, J. Ni, C. Zhao, M. S. Fuhrer, Y. Yang, *et al.*, "Unidirectionally excited phonon polaritons in high-symmetry orthorhombic crystals," *Science advances*, vol. 8, no. 30, p. eabn9774, 2022.

[54] S. G. Menabde, J. Jahng, S. Boroviks, J. Ahn, J. T. Heiden, D. K. Hwang, E. S. Lee, N. A. Mortensen, and M. S. Jang, "Low-loss anisotropic image polaritons in van der waals crystal α-moo3," *Advanced Optical Materials*, p. 2201492, 2022.

[55] S. D. Gedney, "Introduction to the finite-difference time-domain (fdtd) method for electromagnetics," *Synthesis Lectures on Computational Electromagnetics*, vol. 6, no. 1, pp. 1–250, 2011.

[56] J.-M. Jin, *The finite element method in electromagnetics*. John Wiley & Sons, 2015.

[57] T. Grosges, A. Vial, and D. Barchiesi, "Models of near-field spectroscopic studies: comparison between finite-element and finite-difference methods," *Optics Express*, vol. 13, no. 21, pp. 8483–8497, 2005.

[58] C. Parini, S. Gregson, J. McCormick, D. J. Van Rensburg, and T. Eibert, *Theory and Practice of Modern Antenna Range Measurements, Volume 1*. Institution of Engineering and Technology, 2020.

[59] G. Binnig, C. F. Quate, and C. Gerber, "Atomic force microscope," *Physical review letters*, vol. 56, no. 9, p. 930, 1986.

[60] H. A. Bethe, "Theory of diffraction by small holes," *Physical review*, vol. 66, no. 7-8, p. 163, 1944.

[61] B. Knoll and F. Keilmann, "Mid-infrared scanning near-field optical microscope resolves 30 nm," *Journal of microscopy*, vol. 194, no. 2-3, pp. 512–515, 1999.

[62] T. Schädle and B. Mizaikoff, "Mid-infrared waveguides: a perspective," *Applied Spectroscopy*, vol. 70, no. 10, pp. 1625–1638, 2016.

[63] R. Hillenbrand, T. Taubner, and F. Keilmann, "Phonon-enhanced light–matter interaction at the nanometre scale," *Nature*, vol. 418, no. 6894, pp. 159–162, 2002.

[64] A. Cvitkovic, N. Ocelic, and R. Hillenbrand, "Analytical model for quantitative prediction of material contrasts in scattering-type near-field optical microscopy," *Optics express*, vol. 15, no. 14, pp. 8550–8565, 2007.

[65] J. Aizpurua, T. Taubner, F. J. G. de Abajo, M. Brehm, and R. Hillenbrand, "Substrate-enhanced infrared near-field spectroscopy," *Optics Express*, vol. 16, no. 3, pp. 1529–1545, 2008.

[66] N. Ocelic, A. Huber, and R. Hillenbrand, "Pseudoheterodyne detection for background-free near-field spectroscopy," *Applied Physics Letters*, vol. 89, no. 10, p. 101124, 2006.

[67] F. Mooshammer, M. A. Huber, F. Sandner, M. Plankl, M. Zizlsperger, and R. Huber, "Quantifying nanoscale electromagnetic fields in near-field microscopy by fourier demodulation analysis," *Acs Photonics*, vol. 7, no. 2, pp. 344–351, 2020.

[68] F. Huth, A. Govyadinov, S. Amarie, W. Nuansing, F. Keilmann, and R. Hillenbrand, "Nano-ftir absorption spectroscopy of molecular fingerprints at 20 nm spatial resolution," *Nano letters*, vol. 12, no. 8, pp. 3973–3978, 2012.

[69] I. Amenabar, S. Poly, W. Nuansing, E. H. Hubrich, A. A. Govyadinov, F. Huth, R. Krutokhvostov, L. Zhang, M. Knez, J. Heberle, *et al.*, "Structural analysis and mapping of individual protein complexes by infrared nanospectroscopy," *Nature communications*, vol. 4, no. 1, pp. 1–9, 2013.

[70] A. A. Govyadinov, I. Amenabar, F. Huth, P. S. Carney, and R. Hillenbrand, "Quantitative measurement of local infrared absorption and dielectric function with tip-enhanced near-field microscopy," *The journal of physical chemistry letters*, vol. 4, no. 9, pp. 1526–1531, 2013.

[71] F. Huth, M. Schnell, J. Wittborn, N. Ocelic, and R. Hillenbrand, "Infrared-spectroscopic nanoimaging with a thermal source," *Nature materials*, vol. 10, no. 5, pp. 352–356, 2011.

[72] A. Mancini, C. R. Gubbin, R. Berté, F. Martini, A. Politi, E. Cortés, Y. Li, S. De Liberato, and S. A. Maier, "Near-field spectroscopy of cylindrical phonon-polariton antennas," *ACS Nano*, vol. 14, no. 7, pp. 8508–8517, 2020.

[73] J. D. Caldwell, O. J. Glembocki, Y. Francescato, N. Sharac, V. Giannini, F. J. Bezares, J. P. Long, J. C. Owrutsky, I. Vurgaftman, J. G. Tischler, V. D. Wheeler, N. D. Bassim, L. M. Shirey, R. Kasica, and S. A. Maier, "Low-loss, extreme subdiffraction photon confinement *via* silicon carbide localized surface phonon polariton resonators," *Nano Lett.*, vol. 13, no. 8, pp. 3690–3697, 2013.

[74] C. R. Gubbin, S. A. Maier, and S. De Liberato, "Theoretical investigation of phonon polaritons in sic micropillar resonators," *Phys. Rev. B*, vol. 95, no. 3, p. 035313, 2017.

[75] C. R. Gubbin, R. Berte, M. A. Meeker, A. J. Giles, C. T. Ellis, J. G. Tischler, V. D. Wheeler, S. A. Maier, J. D. Caldwell, and S. De Liberato, "Hybrid longitudinal-transverse phonon polaritons," *Nat. Commun.*, vol. 10, p. 1682, 2019.

[76] Y. Chen, Y. Francescato, J. D. Caldwell, V. Giannini, T. W. Maß, O. J. Glembocki, F. J. Bezares, T. Taubner, R. Kasica, M. Hong, and S. A. Maier, "Spectral tuning of localized surface phonon polariton resonators for low-loss mid-ir applications," *ACS Photonics*, vol. 1, no. 8, pp. 718–724, 2014.

[77] C. R. Gubbin, F. Martini, A. Politi, S. A. Maier, and S. De Liberato, "Strong and coherent coupling between localized and propagating phonon polaritons," *Phys. Rev. Lett.*, vol. 116, no. 24, p. 246402, 2016.

[78] G. Lu, C. R. Gubbin, J. R. Nolen, T. Folland, M. J. Tadjer, S. De Liberato, and J. D. Caldwell, "Engineering the spectral and spatial dispersion of thermal emission via polariton–phonon strong coupling," *Nano Letters*, vol. 21, no. 4, pp. 1831–1838, 2021.

[79] C. R. Gubbin and S. De Liberato, "Theory of nonlinear polaritonics: χ (2) scattering on a β-sic surface," *ACS Photonics*, vol. 4, no. 6, pp. 1381–1388, 2017.

[80] I. Razdolski, N. C. Passler, C. R. Gubbin, C. J. Winta, R. Cernansky, F. Martini, A. Politi, S. A. Maier, M. Wolf, A. Paarmann, and S. De Liberato, "Second harmonic generation from strongly coupled localized and propagating phonon-polariton modes," *Phys. Rev. B*, vol. 98, no. 12, p. 125425, 2018.

[81] C. R. Gubbin and S. De Liberato, "Theory of four-wave-mixing in phonon polaritons," *ACS Photonics*, vol. 5, no. 2, pp. 284–288, 2018.

[82] S.-i. Nakashima and H. Harima, "Raman investigation of sic polytypes," *Phys. Status Solidi A*, vol. 162, no. 1, pp. 39–64, 1997.

[83] P. Nordlander and E. Prodan, "Plasmon hybridization in nanoparticles near metallic surfaces," *Nano Lett.*, vol. 4, no. 11, pp. 2209–2213, 2004.

[84] V. G. Kravets, A. V. Kabashin, W. L. Barnes, and A. N. Grigorenko, "Plasmonic surface lattice resonances: A review of properties and applications," *Chem. Rev.*, vol. 118, no. 12, pp. 5912–5951, 2018.

[85] I. Razdolski, Y. Chen, A. J. Giles, S. Gewinner, W. Schöllkopf, M. Hong, M. Wolf, V. Giannini, J. D. Caldwell, S. A. Maier, and A. Paarmann, "Resonant enhancement of second-harmonic generation in the mid-infrared using localized surface phonon polaritons in subdiffractional nanostructures," *Nano Lett.*, vol. 16, no. 11, pp. 6954–6959, 2016. PMID: 27766887.

[86] H. Gudjonson, M. A. Kats, K. Liu, Z. Nie, E. Kumacheva, and F. Capasso, "Accounting for inhomogeneous broadening in nano-optics by electromagnetic modeling based on monte carlo methods," *Proc. Natl. Acad. Sci.*, vol. 111, no. 6, pp. E639–E644, 2014.

[87] H. Altug, S.-H. Oh, S. A. Maier, and J. Homola, "Advances and applications of nanophotonic biosensors," *Nature Nanotechnology*, vol. 17, no. 1, pp. 5–16, 2022.

[88] A. V. Shchegrov, K. Joulain, R. Carminati, and J.-J. Greffet, "Near-field spectral effects due to electromagnetic surface excitations," *Phys. Rev. Lett.*, vol. 85, no. 7, p. 1548, 2000.

[89] A. García-Etxarri, I. Romero, F. J. G. de Abajo, R. Hillenbrand, and J. Aizpurua, "Influence of the tip in near-field imaging of nanoparticle plasmonic modes: Weak and strong coupling regimes," *Phys. Rev. B*, vol. 79, no. 12, p. 125439, 2009.

[90] E. A. Muller, B. Pollard, H. A. Bechtel, R. Adato, D. Etezadi, H. Altug, and M. B. Raschke, "Nanoimaging and control of molecular vibrations through electromagnetically induced scattering reaching the strong coupling regime," *ACS Photonics*, vol. 5, no. 9, pp. 3594–3600, 2018.

[91] T. Folland, L. Nordin, D. Wasserman, and J. Caldwell, "Probing polaritons in the mid-to far-infrared," *J. Appl. Phys.*, vol. 125, no. 19, p. 191102, 2019.

[92] C. Ciracì, Y. Urzhumov, and D. R. Smith, "Far-field analysis of axially symmetric three-dimensional directional cloaks," *Optics express*, vol. 21, no. 8, pp. 9397–9406, 2013.

[93] I. Amenabar, S. Poly, M. Goikoetxea, W. Nuansing, P. Lasch, and R. Hillenbrand, "Hyperspectral infrared nanoimaging of organic samples based on fourier transform infrared nanospectroscopy," *Nature communications*, vol. 8, no. 1, pp. 1–10, 2017.

[94] J. D. Caldwell, A. V. Kretinin, Y. Chen, V. Giannini, M. M. Fogler, Y. Francescato, C. T. Ellis, J. G. Tischler, C. R. Woods, A. J. Giles, *et al.*, "Sub-diffractional volume-confined polaritons in the natural hyperbolic material hexagonal boron nitride," *Nat. Commun.*, vol. 5, no. 1, pp. 1–9, 2014.

[95] V. M. Breslin, D. C. Ratchford, A. J. Giles, A. D. Dunkelberger, and J. C. Owrutsky, "Hyperbolic phonon polariton resonances in calcite nanopillars," *Opt. Express*, vol. 29, no. 8, pp. 11760–11772, 2021.

[96] W. Ma, G. Hu, D. Hu, R. Chen, T. Sun, X. Zhang, Q. Dai, Y. Zeng, A. Alù, C.-W. Qiu, *et al.*, "Ghost hyperbolic surface polaritons in bulk anisotropic crystals," *Nature*, vol. 596, no. 7872, pp. 362–366, 2021.

[97] F. H. Feres, R. A. Mayer, L. Wehmeier, F. C. Maia, E. Viana, A. Malachias, H. A. Bechtel, J. M. Klopf, L. M. Eng, S. C. Kehr, *et al.*, "Sub-diffractional cavity modes of terahertz hyperbolic phonon polaritons in tin oxide," *Nat. Commun.*, vol. 12, no. 1, pp. 1–9, 2021.

[98] M. He, T. G. Folland, J. Duan, P. Alonso-González, S. De Liberato, A. Paarmann, and J. D. Caldwell, "Anisotropy and modal hybridization in infrared nanophotonics using low-symmetry materials," *ACS Photonics*, vol. 9, no. 4, pp. 1078–1095, 2022.

[99] D. Basov, M. Fogler, and F. García de Abajo, "Polaritons in van der waals materials," *Science*, vol. 354, no. 6309, p. aag1992, 2016.

[100] A. Ambrosio, M. Tamagnone, K. Chaudhary, L. A. Jauregui, P. Kim, W. L. Wilson, and F. Capasso, "Selective excitation and imaging of ultraslow phonon polaritons in thin hexagonal boron nitride crystals," *Light Sci. Appl.*, vol. 7, no. 1, pp. 1–9, 2018.

[101] K. Chaudhary, M. Tamagnone, M. Rezaee, D. K. Bediako, A. Ambrosio, P. Kim, and F. Capasso, "Engineering phonon polaritons in van der waals heterostructures to enhance in-plane optical anisotropy," *Sci. Adv.*, vol. 5, no. 4, p. eaau7171, 2019.

[102] Z. Zheng, N. Xu, S. L. Oscurato, M. Tamagnone, F. Sun, Y. Jiang, Y. Ke, J. Chen, W. Huang, W. L. Wilson, *et al.*, "A mid-infrared biaxial hyperbolic van der waals crystal," *Sci. Adv.*, vol. 5, no. 5, p. eaav8690, 2019.

[103] Q. Zhang, Q. Ou, G. Hu, J. Liu, Z. Dai, M. S. Fuhrer, Q. Bao, and C.-W. Qiu, "Hybridized hyperbolic surface phonon polaritons at α-moo3 and polar dielectric interfaces," *Nano Lett.*, vol. 21, no. 7, pp. 3112–3119, 2021.

[104] J. Yang, J. Tang, M. B. Ghasemian, M. Mayyas, Q. V. Yu, L. H. Li, and K. Kalantar-Zadeh, "High-q phonon-polaritons in spatially confined freestanding α-moo3," *ACS Photonics*, vol. 9, no. 3, pp. 905–913, 2022.

[105] M. Chen, X. Lin, T. H. Dinh, Z. Zheng, J. Shen, Q. Ma, H. Chen, P. Jarillo-Herrero, and S. Dai, "Configurable phonon polaritons in twisted α-moo3," *Nat. Mater.*, vol. 19, no. 12, pp. 1307–1311, 2020.

[106] Z. Zheng, F. Sun, W. Huang, J. Jiang, R. Zhan, Y. Ke, H. Chen, and S. Deng, "Phonon polaritons in twisted double-layers of hyperbolic van der waals crystals," *Nano Lett.*, vol. 20, no. 7, pp. 5301–5308, 2020.

[107] Q. Zhang, G. Hu, W. Ma, P. Li, A. Krasnok, R. Hillenbrand, A. Alù, and C.-W. Qiu, "Interface nano-optics with van der waals polaritons," *Nature*, vol. 597, no. 7875, pp. 187–195, 2021.

[108] A. T. Hoang, K. Qu, X. Chen, and J.-H. Ahn, "Large-area synthesis of transition metal dichalcogenides via cvd and solution-based approaches and their device applications," *Nanoscale*, vol. 13, no. 2, pp. 615–633, 2021.

[109] J. Dionne, L. Sweatlock, H. Atwater, and A. Polman, "Planar metal plasmon waveguides: frequency-dependent dispersion, propagation, localization, and loss beyond the free electron model," *Phys. Rev. B*, vol. 72, no. 7, p. 075405, 2005.

[110] Y. Liu, D. F. Pile, Z. Liu, D. Wu, C. Sun, and X. Zhang, "Negative group velocity of surface plasmons on thin metallic films," *Proc. SPIE*, vol. 6323, pp. 224–232, 2006.

[111] M. Francoeur, M. P. Mengüç, and R. Vaillon, "Spectral tuning of near-field radiative heat flux between two thin silicon carbide films," *J. Phys. D: Appl. Phys.*, vol. 43, no. 7, p. 075501, 2010.

[112] M. Francoeur, M. P. Mengüç, and R. Vaillon, "Local density of electromagnetic states within a nanometric gap formed between two thin films supporting surface phonon polaritons," *J. Appl. Phys.*, vol. 107, no. 3, p. 034313, 2010.

[113] S. Dai, J. Quan, G. Hu, C.-W. Qiu, T. H. Tao, X. Li, and A. Alù, "Hyperbolic phonon polaritons in suspended hexagonal boron nitride," *Nano Lett.*, vol. 19, no. 2, pp. 1009–1014, 2018.

[114] J. Shen, Z. Zheng, T. Dinh, C. Wang, M. Chen, P. Chen, Q. Ma, P. Jarillo-Herrero, L. Kang, and S. Dai, "Hyperbolic phonon polaritons with positive and negative phase velocities in suspended α-moo3," *Appl. Phys. Lett.*, vol. 120, no. 11, p. 113101, 2022.

[115] H. Hu, R. Yu, H. Teng, D. Hu, N. Chen, Y. Qu, X. Yang, X. Chen, A. McLeod, P. Alonso-González, *et al.*, "Active control of micrometer plasmon propagation in suspended graphene," *Nat. Commun.*, vol. 13, no. 1, pp. 1–9, 2022.

[116] A. Huber, N. Ocelic, D. Kazantsev, and R. Hillenbrand, "Near-field imaging of mid-infrared surface phonon polariton propagation," *Appl. Phys. Lett.*, vol. 87, no. 8, p. 081103, 2005.

[117] P. Rufangura, T. G. Folland, A. Agrawal, J. D. Caldwell, and F. Iacopi, "Towards low-loss on-chip nanophotonics with coupled graphene and silicon carbide: A review," *JPhys Materials*, vol. 3, no. 3, p. 032005, 2020.

[118] A. L. Falk, B. B. Buckley, G. Calusine, W. F. Koehl, V. V. Dobrovitski, A. Politi, C. A. Zorman, P. X.-L. Feng, and D. D. Awschalom, "Polytype control of spin qubits in silicon carbide," *Nat. Commun.*, vol. 4, no. 1, pp. 1–7, 2013.

[119] I. Chatzopoulos, F. Martini, R. Cernansky, and A. Politi, "High-q/v photonic crystal cavities and qed analysis in 3c-sic," *ACS Photonics*, vol. 6, no. 8, pp. 1826–1831, 2019.

[120] D.-Z. A. Chen, A. Narayanaswamy, and G. Chen, "Surface phonon-polariton mediated thermal conductivity enhancement of amorphous thin films," *Phys. Rev. B*, vol. 72, no. 15, p. 155435, 2005.

[121] L. Tranchant, S. Hamamura, J. Ordonez-Miranda, T. Yabuki, A. Vega-Flick, F. Cervantes-Alvarez, J. J. Alvarado-Gil, S. Volz, and K. Miyazaki, "Two-dimensional phonon polariton heat transport," *Nano Lett.*, vol. 19, no. 10, pp. 6924–6930, 2019.

[122] Y. Wu, J. Ordonez-Miranda, S. Gluchko, R. Anufriev, D. D. S. Meneses, L. Del Campo, S. Volz, and M. Nomura, "Enhanced thermal conduction by surface phonon-polaritons," *Sci. Adv.*, vol. 6, no. 40, p. eabb4461, 2020.

[123] H. Xiong, Y. Lu, Q. Wu, Z. Li, J. Qi, X. Xu, R. Ma, and J. Xu, "Topological valley transport of terahertz phonon–polaritons in a linbo3 chip," *ACS Photonics*, vol. 8, no. 9, pp. 2737–2745, 2021.

[124] S. Guddala, F. Komissarenko, S. Kiriushechkina, A. Vakulenko, M. Li, V. Menon, A. Alù, and A. Khanikaev, "Topological phonon-polariton funneling in midinfrared metasurfaces," *Science*, vol. 374, no. 6564, pp. 225–227, 2021.

[125] L. Tang, J. DeSutter, and M. Francoeur, "Near-field radiative heat transfer between dissimilar materials mediated by coupled surface phonon-and plasmon-polaritons," *Acs Photonics*, vol. 7, no. 5, pp. 1304–1311, 2020.

[126] S. Shen, A. Narayanaswamy, and G. Chen, "Surface phonon polaritons mediated energy transfer between nanoscale gaps," *Nano Lett.*, vol. 9, no. 8, pp. 2909–2913, 2009.

[127] K. Kim, B. Song, V. Fernández-Hurtado, W. Lee, W. Jeong, L. Cui, D. Thompson, J. Feist, M. Reid, F. J. García-Vidal, *et al.*, "Radiative heat transfer in the extreme near field," *Nature*, vol. 528, no. 7582, pp. 387–391, 2015.

[128] R. St-Gelais, L. Zhu, S. Fan, and M. Lipson, "Near-field radiative heat transfer between parallel structures in the deep subwavelength regime," *Nat. Nanotechnol.*, vol. 11, no. 6, pp. 515–519, 2016.

[129] A. Bylinkin, M. Schnell, F. Calavalle, P. Li, J. Taboada-Gutièrrez, S. Liu, J. H. Edgar, F. Casanova, L. E. Hueso, P. Alonso-Gonzalez, *et al.*, "Real-space observation of vibrational strong coupling between propagating phonon polaritons and organic molecules," *Nat. Photonics*, vol. 15, no. 3, pp. 197–202, 2021.

[130] E. Yoxall, M. Schnell, A. Y. Nikitin, O. Txoperena, A. Woessner, M. B. Lundeberg, F. Casanova, L. E. Hueso, F. H. Koppens, and R. Hillenbrand, "Direct observation of ultraslow hyperbolic polariton propagation with negative phase velocity," *Nat. Photonics*, vol. 9, no. 10, pp. 674–678, 2015.

[131] K. J. Kaltenecker, E. Krauss, L. Casses, M. Geisler, B. Hecht, N. A. Mortensen, P. U. Jepsen, and N. Stenger, "Mono-crystalline gold platelets: a high-quality platform for surface plasmon polaritons," *Nanophotonics*, vol. 9, no. 2, pp. 509–522, 2020.

[132] N. C. Passler, I. Razdolski, D. S. Katzer, D. F. Storm, J. D. Caldwell, M. Wolf, and A. Paarmann, "Second harmonic generation from phononic epsilon-near-zero berreman modes in ultrathin polar crystal films," *Acs Photonics*, vol. 6, no. 6, pp. 1365–1371, 2019.

[133] S. Campione, I. Brener, and F. Marquier, "Theory of epsilon-near-zero modes in ultrathin films," *Phys. Rev. B*, vol. 91, no. 12, p. 121408, 2015.

[134] F. Mörz, R. Semenyshyn, T. Steinle, F. Neubrech, U. Zschieschang, H. Klauk, A. Steinmann, and H. Giessen, "Nearly diffraction limited ftir mapping using an ultrastable broadband femtosecond laser tunable from 1.33 to 8 μm," *Opt. Express*, vol. 25, no. 26, pp. 32355–32363, 2017.

[135] B. Hauer, A. P. Engelhardt, and T. Taubner, "Quasi-analytical model for scattering infrared near-field microscopy on layered systems," *Opt. Express*, vol. 20, no. 12, pp. 13173–13188, 2012.

[136] F. Walla, M. M. Wiecha, N. Mecklenbeck, S. Beldi, F. Keilmann, M. D. Thomson, and H. G. Roskos, "Anisotropic excitation of surface plasmon polaritons on a metal film by a scattering-type scanning near-field microscope with a non-rotationally-symmetric probe tip," *Nanophotonics*, vol. 7, no. 1, pp. 269–276, 2018.

[137] J. Barnett, D. Wendland, M. Lewin, K. Wirth, A. Heßler, and T. Taubner, "Investigation of low-confinement surface phonon polariton launching on sic and srtio3 using scanning near-field optical microscopy," *Appl. Phys. Lett.*, vol. 120, no. 21, p. 211107, 2022.

[138] F. Hu, Y. Luan, M. Scott, J. Yan, D. Mandrus, X. Xu, and Z. Fei, "Imaging exciton–polariton transport in mose2 waveguides," *Nat. Phot.*, vol. 11, no. 6, pp. 356–360, 2017.

[139] B. Liao, X. Guo, D. Hu, F. Zhai, H. Hu, K. Chen, C. Luo, M. Liu, X. Yang, and Q. Dai, "A multibeam interference model for analyzing complex near-field images of polaritons in 2d van der waals microstructures," *Adv. Funct. Mater.*, vol. 29, no. 42, p. 1904662, 2019.

[140] A. J. Giles, S. Dai, I. Vurgaftman, T. Hoffman, S. Liu, L. Lindsay, C. T. Ellis, N. Assefa, I. Chatzakis, T. L. Reinecke, *et al.*, "Ultralow-loss polaritons in isotopically pure boron nitride," *Nat. Mater.*, vol. 17, no. 2, pp. 134–139, 2018.

[141] C. Li, S. A. Maier, and H. Ren, "Optical vortices in nanophotonics," *arXiv preprint arXiv:2103.14163*, 2021.

[142] M. Beijersbergen, R. Coerwinkel, M. Kristensen, and J. Woerdman, "Helical-wavefront laser beams produced with a spiral phaseplate," *Optics communications*, vol. 112, no. 5-6, pp. 321–327, 1994.

[143] N. Yu, P. Genevet, M. A. Kats, F. Aieta, J.-P. Tetienne, F. Capasso, and Z. Gaburro, "Light propagation with phase discontinuities: generalized laws of reflection and refraction," *science*, vol. 334, no. 6054, pp. 333–337, 2011.

[144] F. Tamburini, E. Mari, A. Sponselli, B. Thidé, A. Bianchini, and F. Romanato, "Encoding many channels on the same frequency through radio vorticity: first experimental test," *New journal of physics*, vol. 14, no. 3, p. 033001, 2012.

[145] B. Knyazev, Y. Y. Choporova, M. Mitkov, V. Pavelyev, and B. Volodkin, "Generation of terahertz surface plasmon polaritons using nondiffractive bessel beams with orbital angular momentum," *Physical review letters*, vol. 115, no. 16, p. 163901, 2015.

[146] P. Genevet, J. Lin, M. A. Kats, and F. Capasso, "Holographic detection of the orbital angular momentum of light with plasmonic photodiodes," *Nature communications*, vol. 3, no. 1, pp. 1–5, 2012.

[147] H. Ren, X. Li, Q. Zhang, and M. Gu, "On-chip noninterference angular momentum multiplexing of broadband light," *Science*, vol. 352, no. 6287, pp. 805–809, 2016.

[148] F. Machado, N. Rivera, H. Buljan, M. Soljačić, and I. Kaminer, "Shaping polaritons to reshape selection rules," *ACS Photonics*, vol. 5, no. 8, pp. 3064–3072, 2018.

[149] A. M. Konzelmann, S. O. Krüger, and H. Giessen, "Interaction of orbital angular momentum light with rydberg excitons: Modifying dipole selection rules," *Physical Review B*, vol. 100, no. 11, p. 115308, 2019.

[150] Y. Gorodetski, A. Niv, V. Kleiner, and E. Hasman, "Observation of the spin-based plasmonic effect in nanoscale structures," *Physical review letters*, vol. 101, no. 4, p. 043903, 2008.

[151] H. Kim, J. Park, S.-W. Cho, S.-Y. Lee, M. Kang, and B. Lee, "Synthesis and dynamic switching of surface plasmon vortices with plasmonic vortex lens," *Nano letters*, vol. 10, no. 2, pp. 529–536, 2010.

[152] Y. Zhang, X. Zeng, L. Ma, R. Zhang, Z. Zhan, C. Chen, X. Ren, C. He, C. Liu, and C. Cheng, "Manipulation for superposition of orbital angular momentum states in surface plasmon polaritons," *Advanced Optical Materials*, vol. 7, no. 18, p. 1900372, 2019.

[153] A. David, B. Gjonaj, Y. Blau, S. Dolev, and G. Bartal, "Nanoscale shaping and focusing of visible light in planar metal–oxide–silicon waveguides," *Optica*, vol. 2, no. 12, pp. 1045–1048, 2015.

[154] A. David, B. Gjonaj, and G. Bartal, "Two-dimensional optical nanovortices at visible light," *Physical Review B*, vol. 93, no. 12, p. 121302, 2016.

[155] G. Spektor, D. Kilbane, A. Mahro, B. Frank, S. Ristok, L. Gal, P. Kahl, D. Podbiel, S. Mathias, H. Giessen, *et al.*, "Revealing the subfemtosecond dynamics of orbital angular momentum in nanoplasmonic vortices," *Science*, vol. 355, no. 6330, pp. 1187–1191, 2017.

[156] G. Spektor, E. Prinz, M. Hartelt, A.-K. Mahro, M. Aeschlimann, and M. Orenstein, "Orbital angular momentum multiplication in plasmonic vortex cavities," *Science Advances*, vol. 7, no. 33, p. eabg5571, 2021.

[157] A. Faßbender, J. Babockỳ, P. Dvořák, V. Křápek, and S. Linden, "Invited article: direct phase mapping of broadband laguerre-gaussian metasurfaces," *APL Photonics*, vol. 3, no. 11, p. 110803, 2018.

[158] A. Vijayakumar, C. Rosales-Guzmán, M. Rai, J. Rosen, O. Minin, I. Minin, and A. Forbes, "Generation of structured light by multilevel orbital angular momentum holograms," *Optics express*, vol. 27, no. 5, pp. 6459–6470, 2019.

[159] S. Fu, Y. Zhai, J. Zhang, X. Liu, R. Song, H. Zhou, and C. Gao, "Universal orbital angular momentum spectrum analyzer for beams," *PhotoniX*, vol. 1, no. 1, pp. 1–12, 2020.

[160] L. Xiong, Y. Li, D. Halbertal, M. Sammon, Z. Sun, S. Liu, J. H. Edgar, T. Low, M. M. Fogler, C. R. Dean, *et al.*, "Polaritonic vortices with a half-integer charge," *Nano letters*, vol. 21, no. 21, pp. 9256–9261, 2021.

[161] M. Wang, G. Hu, S. Chand, M. Cotrufo, Y. Abate, K. Watanabe, T. Taniguchi, G. Grosso, C.-W. Qiu, and A. Alù, "Spin-orbit-locked hyperbolic polariton vortices carrying reconfigurable topological charges," *eLight*, vol. 2, no. 1, pp. 1–11, 2022.

[162] M. Schnell, A. Garcia-Etxarri, A. J. Huber, K. B. Crozier, A. Borisov, J. Aizpurua, and R. Hillenbrand, "Amplitude-and phase-resolved near-field mapping of infrared antenna modes by transmission-mode scattering-type near-field microscopy," *The Journal of Physical Chemistry C*, vol. 114, no. 16, pp. 7341–7345, 2010.

[163] M. Schnell, P. Alonso-Gonzalez, L. Arzubiaga, F. Casanova, L. E. Hueso, A. Chuvilin, and R. Hillenbrand, "Nanofocusing of mid-infrared energy with tapered transmission lines," *Nature photonics*, vol. 5, no. 5, pp. 283–287, 2011.

[164] S. Tsesses, E. Ostrovsky, K. Cohen, B. Gjonaj, N. Lindner, and G. Bartal, "Optical skyrmion lattice in evanescent electromagnetic fields," *Science*, vol. 361, no. 6406, pp. 993–996, 2018.

[165] S. Tsesses, K. Cohen, E. Ostrovsky, B. Gjonaj, and G. Bartal, "Spin–orbit interaction of light in plasmonic lattices," *Nano letters*, vol. 19, no. 6, pp. 4010–4016, 2019.

[166] P. Alonso-Gonzalez, M. Schnell, P. Sarriugarte, H. Sobhani, C. Wu, N. Arju, A. Khanikaev, F. Golmar, P. Albella, L. Arzubiaga, *et al.*, "Real-space mapping of fano interference in plasmonic metamolecules," *Nano letters*, vol. 11, no. 9, pp. 3922–3926, 2011.

[167] R. Berte, C. R. Gubbin, V. D. Wheeler, A. J. Giles, V. Giannini, S. A. Maier, S. De Liberato, and J. D. Caldwell, "Sub-nanometer thin oxide film sensing with localized surface phonon polaritons," *ACS photonics*, vol. 5, no. 7, pp. 2807–2815, 2018.

[168] T. Wang, P. Li, D. N. Chigrin, A. J. Giles, F. J. Bezares, O. J. Glembocki, J. D. Caldwell, and T. Taubner, "Phonon-polaritonic bowtie nanoantennas: controlling infrared thermal radiation at the nanoscale," *Acs Photonics*, vol. 4, no. 7, pp. 1753–1760, 2017.

[169] J. K. Gansel, M. Thiel, M. S. Rill, M. Decker, K. Bade, V. Saile, G. von Freymann, S. Linden, and M. Wegener, "Gold helix photonic metamaterial as broadband circular polarizer," *science*, vol. 325, no. 5947, pp. 1513–1515, 2009.

[170] J. Duan, G. Álvarez-Pérez, K. V. Voronin, I. Prieto, J. Taboada-Gutiérrez, V. S. Volkov, J. Martín-Sánchez, A. Y. Nikitin, and P. Alonso-González, "Enabling propagation of anisotropic polaritons along forbidden directions via a topological transition," *Science Advances*, vol. 7, no. 14, p. eabf2690, 2021.

Acknowledgements

I would like to thank my supervisor Prof. Stefan A. Maier for always being supportive in my research plans and for caring for the development of all of his students.

Next, I would like to thank all the people that have helped me settle in in Munich and were there from the beginning, Dr. Yi Li, Dr. Ludwig Huettenhofer and Benjamin Tilmann.

These years would have not been as enjoyable if not for the group of PhD students that started in the same period as me: Matias Herran, Simone Ezendam and Lin Nan. Smiliarly, I would like to thank Dr. Rodrigo Berte, Dr. Julian Gargiulo, Dr. Fedja Wendish and Dr. Luca Sortino for the intense scientific discussions and the time spent together outside of working hours.

As I started my PhD split between the near-field world of sSNOM and the far-field world of iSCAT, the help of Christoph Gruber and Franz Groebmeyer in this latter part has been fundamental in being able to continue in this direction.

I would like to thank Dr. Fritz Keilmann for organizing every year the very enjoyable Alptip "conference" in which I was able to connect with other sSNOM practitioners. Dealing with sSNOM can be frustrating, and I would like to thank Thorsten Goelz for many discussions and time spent on the setup.

Overall, I would like to thank the whole Hybrid Nano group for the enjoyable working environment. In particular I want thank Prof. Leonardo Menezes for all the work he does for the group and the light-hearted atmosphere he carries with himself.

Finally I would like to thank all my friends in Rome and my parents who kept supporting me during these years.